Research on Health Assessment Technique of Mountain Tunnel Lining Based on the Microtremor Method

常時微動計測に基づく山岳トンネル覆工コンクリートの健全度評価技術の研究

August 2014

2014 年 8 月

Graduate School of Engineering, Nagasaki University

長崎大学大学院工学研究科

Yang GAO

高　陽

Acknowledgements

It would not have been possible to finish this doctoral thesis without the support of the kind people around me, to only some of whom it is possible to give particular mention here.

First and foremost, I would like to thank my adviser, Prof. **Yujing Jiang**, a respectable, responsible and resourceful scholar, who has been supportive since I began studying in Nagasaki University. He taught me not only the skill of writing a research paper, but also the method of solving problems which is invaluable in my future study. I gratefully acknowledge my committee members, Prof. **Akihide Saimoto** and Prof. **Kiyoshi Omine**, for their valuable comments and suggestions to refine this thesis.

I am very thankful to my former supervisors, Prof. **Shucai Li** and Prof. **Qingsong Zhang** in Shandong University, for their fundamental assistance and guidance in getting my postgraduate study started on the right foot and cultivating me with solid science foundation. Also, I am extremely grateful to the Assistant Prof. **Bo Li**, who gave the good advice, support and friendship on both academic and personal matters.

I would like to thank my friends in Nagasaki, **Dr. Lei Yang, Dr. Kangming Chen, Dr. Sha Lou, Mr. Richeng Liu, Mr. Yan Du, Miss Xiaoshan Wang, Mr. Xiao Shi, Mr Xuezhen Wu** and all others who helped make my stay in Japan a very pleasant one.

Finally, and most importantly, I would like to thank my wife **Miaomiao Zhao.** During the whole time of study, she always supported and encouraged me and gave birth to our beautiful daughter **Qiqi**. Words are not sufficient to express the overwhelming love for her. Also, I would like to thank my parents, for their love, patience and support over my entire lifetime.

Yang Gao

June 2014

Abstract

Japan is a country surrounded by sea and 70% of its land is covered by mountains. A large number of tunnels have been constructed during the last several decades. To date, a great number of tunnels have been in service for more than 50 years. The persistent ageing of tunnels causes many problems on the lining of tunnel, such as corrosion, spalling, fracturing, generation of internal voids and seepage. Deteriorations and damages of lining concrete decrease the integrity of tunnel lining and subsequently affect the workability, serviceability and safety reliability of tunnels. From the pioneering attempt on civil engineering structures in 1930s by Carder, the ambient test has attracted more and more attentions for assessing the health state of civil structures in operational conditions due to its easy testing & data understanding, low cost and multiple-input. Hereby, this dissertation mainly investigates the relationship between the tunnel lining healthy state and its vibration behaviors.

First of all, the EDEM with the function of simulating rock cracking was developed by implanting the tensile-shear failure criterion into the DEM code of UDEC, and it was utilized to investigate the natural frequency variation of the cracking reinforcement beam. The validity and accuracy of the EDEM were verified by comparing the numerical results with the experimental results.

Secondly, the vibration characters of tunnel lining shells built with poling-board method was analyzed based on the analytical solutions. Both the Love-Timoshenko shell theory and Donnell-Mushtari shell theory are adopted and extended to the elastic boundary conditions to analyze the vibration characters of tunnel lining, and the rock-concrete contacts were treated as elastic boundaries represented by the distributed springs. The void between concrete linings and rock masses was treated as the additional load and its influence on the natural frequency was estimated by the modal expansion approach. The validity and the accuracy of the proposed theory were verified by the numerical results of the Distinct Element Method (DEM) code of

UDEC. Thirdly, the in-situ microtremor measurements were carried out on three spans of Satomi tunnel (the seriously damaged span S1, the moderately damaged span S2 and the healthy span S3). The microtremors were analyzed at the frequency domain (i.e., power spectral density (PSD)). The modal parameters including nature frequencies and damping ratios were extracted from the measured data. The relation between microtremor characteristics and the health conditions of tunnel was discussed. As an initial step, the in-situ measurements give clear evidence that the microtremor vibration characteristics have strong relation with the health conditions of lining concrete.

Moreover, a horse shoe shaped tunnel lining, of which the lining shape and the physico-mechanical properties of the surrounding rock mass and lining concrete are in accordance with the tested tunnel, was modeled by the code of UDEC to verify the in-situ measurements and to give a better understanding about the microtremor vibration behaviors. The relationship between the stiffness of rock-concrete interface and the peak frequency was analyzed. The influences of the voids and their geometrical parameters, rock type and concrete type on frequency response of tunnel lining were studied. The relationship between the peak frequency and the stress state of the tunnel lining were also discussed based on the numerical results.

A void delineation method based on the vibration intensity of microtremors was also discussed. In this method, the vibration modal parameters (natural frequencies, mode shapes and dampings) are unnecessary to obtain by the modal identification procedure. The mean values of PSD were adopted to represent the vibration intensity of microtremors. The vibration intensity ratios of the microtremors in different directions were analyzed. In the numerical simulations, not Gaussian while noise but the microtremors measured at the healthy span were chosen as far-field vibration sources. Influences of the properties of rock-concrete interfaces, the voids and their geometrical parameters, and the mechanical properties of rock and concrete on the vibration intensity ratio of tunnel linings were also studied.

CONTENTS

CHAPTER 1

Introduction

1.1 Research background

In many countries of the world, a great number of tunnels have been commissioned for several decades, and the persistent ageing of tunnels causes many problems on the lining of tunnel, such as corrosion, buckling, fracturing, the creation of internal voids and the seepage induced by flaws (Malmgren et al., 2005). As an important primary support of the underground excavations, the concrete lining serves a number of functions, such as supporting the adjacent rock blocks, prevent ground erosion and degradation. Deteriorations and damages of lining concrete decrease the integrity of tunnel lining and subsequently affect the workability, serviceability and safety reliability of tunnels (Aktan et al., 2000; Bhalla et al., 2005).

At present, a number of damage inspection methods in both destructive and non-destructive manners have been proposed and used in practices. Representative ones include visual inspection, core sampling, ground penetrating radar (GPR), ultrasonic method, and magnetic method, etc. (Daniels, 2004; Jiles, 1990; Poranski et al., 1996). The visual inspection, including video and visual light surveying, crack measurements, is the primary method during the periodic inspections. The periodic inspections will serve to discover whether damaged areas or weak points exist, and to judge whether or not detailed inspections about the state conditions and the damage information are necessary to carry out (Asakura and Kojima, 2003). Coring provides specific information inside of tunnel lining within limited inspection areas, but is slow and expensive. Non-destructive methods could help improve investigation periods in relatively large areas. However, highly-experienced operators are essential in these inspections, and considerable time and cost are required to estimate the overall structural integrity in the most previous techniques (Park and Choi, 2008).

The damage of lining results in a localized reduction of the strength and stiffness of lining concrete. It has been found that the vibration modal parameters such as the natural frequency of concrete structures are significantly sensitive to their damage status (Konno and Ohmachi, 1998). Salawu (1997) presents an excellent review on the use of modal frequency changes for damage diagnostics. The changes in structural properties cause a variation of vibration frequencies. It also should be noted that

frequency shifts have significant practical limitations for applications in some special structures considered, although ongoing and future work may help resolve these difficulties. More precise sensors or larger levels of damage are necessary to identify the somewhat low sensitivity of frequency shifts due to damage. However, many studies have shown that resonant frequencies have much less statistical variation from random error sources than other modal parameters (Farrar, et al. 1997; Doebling, et al. 1997). Using frequency shifts to detect damage appears to be more practical in applications where such shifts can be measured very precisely in a controlled environment, such as for quality control in manufacturing (Migliori, et al., 1993). So far, various methodologies have been proposed and verified in simple systems, such as beams (Kim et al., 2003; Lam et al., 2005), plates (Yam et al., 2002; Loutridis et al., 2005) and building models (Yuen and Lam, 2006; Lam and Ng, 2008). It provides a possible approach for effectively detecting the damages of the tunnel lining.

1.1.1 Theoretical background about vibrations of thin shells with the elastic support

A mountain tunnel lining can be treated as a cylindrical shell structure of which the thickness is much smaller than other dimensions. The vibration of thin elastic shells has been studied by many researchers and numerous different shell theories have been derived in the literature (Leissa, 1973; Soedel, 1981; Cremer, Heckl and Ungar 1988). The differences among these theories are the various assumptions about the form of terms in small magnitude (e.g., tiny displacement) and the order of terms which are retained in the analysis, and numerous thin cylindrical shells with ideal boundary conditions classed, e.g., as clamped, free and simply supported with axial constraint and simply supported without axial constraint were analyzed in these literature.

A variety of methods have been applied to the study of thin shell vibration. Approximate analyses based on various shell theories have been performed using the Rayleigh-Ritz method (Leissa, 1973). Exact solution of the Flugge shell theory equations of motion has been performed by various authors (Forsberg, 1964; Warburton, 1965, 1970; Vronay and Smith, 1970), and accurate solutions can be achieved with this approach. The exact solution of wave propagation in infinite

cylinders, which is a simple, non-iterative and effective method, has also been widely used for the thin shell vibrations with different boundary conditions (Aremenakas et al., 1969; Harari, 1978; Fuller, 1981). Wang and Lai (2000) used this approach to study the vibration of the infinite length circular cylindrical shells based on Love's shell theory and gave an approximate method for the natural frequency calculations. Zhang et al. (2001) calculated the natural frequency of thin cylindrical shells and compared the results of both the wave propagation method and numerical finite element method. Zhang et al. (2001a, b; 2004;) have also extended this approach to coupled vibration of fluid-filled shells, submerged shells and cross-ply laminated composite shells. Xu et al. (1998; 1999a, b) studied the power flow propagating in fluid-filled shells with this approach.

1.1.2 Modal parameter identification based on the vibration measurements

There are two methods available in measuring the vibration response of a structure: the forced vibration test and the ambient vibration test. In early times, the forced vibration tests were preferred due to the accuracy of the corresponding identification techniques. However, this method is not applicable or not practical for the damage detection of large-scale three-dimensional structures, in which huge reaction mass shakers are necessary (Peeters et al., 2001). With the development and application of high sensitivity accelerometer, the low-cost ambient test has become the main experimental method for the structural damage identification. The ambient vibration measurement is a kind of output-only data dynamic testing and a modal analysis procedure is carried out based on output-only data.

Ambient vibrations provide information about the modal parameters of a structure that we can extract using modal analysis methods. There are many different techniques to identify the natural modes of a structure, which can be divided into parametric and non-parametric methods (Michel, 2007). In the parametric method, the parameters of the considered model are updated to fit the recorded data in frequency or in time domain (Peeters, 2000). While in the non-parametric method, no special parameters are necessary and only signal processing tools are used so that it is user-friendly easy

to implement. The simplest method to estimate the modal parameters from the ambient vibrations of a structure is the peak-picking method. It is also called the 'half-power method'. The eigenfrequencies can be identified form the frequency peaks of average power spectrum plot for each sensors placed at different measuring points of the structure, and the operational deflection shapes instead of mode shapes can be acquired. This method is best suited for structures with light damping and well separated modes where modal coefficients are essentially real valued. Due to its remarkable simplicity, the peak-picking method can derive quick analysis results. The Singular Value Decomposition (SVD) method is an improvement of the peak-picking method (Brincker, 2001). It consists of decomposing the power spectral density matrices with the auto and cross spectra between the outputs into single-degrees-of-freedom systems by singular value decomposition. This method has been discussed by many researchers with different names (2-4): Principal Component Analysis (PCA), Complex Mode Indication Function (CMIF), and Frequency Domain Decomposition (FDD). The method is able to detect mode-multiplicity (i.e. different modes at the same frequency), but is still rather subjective (Peeters, 2005). The peck-picking and the SVD-based method are both so-called nonparametric methods: the eigenfrequencies are determined by just looking at signal-based features without fitting or estimating a parametric model.

On the other hand, methods in which a parametric model is determined from the data allow the use of objective criteria to assess the modelling quality (e.g. the use of stabilization diagrams or other convergence criteria). In contrast to non-parametric identification, this method leads to finitely parameterized representations, such as difference/differential equation and modal models (Fassois, 2001). These methods can be further classified according to the type of 'structure' imposed on the model evolution of model parameters, including unstructured parameter evolution methods (e.g., ARMA and RML method) (Niedzwiecki, 2000; Cooper and Worden, 2000; Zhan and Jardine, 2005), stochastic parameter evolution methods (Kitagawa, 1983; Gersch, and Kitagawa, 1985) and deterministic parameter evolution methods (e.g., TAR and

TARMA methods) (Conforto, 1999; Mrad, et al., 1988; Fouskitakis and Fassois, 2001).

Microtremor, as one type of ambient vibration originating from the natural or artificial oscillations without specific sources, recently, has attract more and more attentions in the study of the microtremor dynamic properties of concrete structures. The first widely implemented microtremor method, proposed by Nakamura in 1989 (Nakamura, 1989), is the Horizontal to Vertical Spectral Ratio (H/V) method used to derive the dynamic characteristics of soil and rock ground. The applicability of Nakamura's method was verified and developed through the field investigation (Lermo and Chavez, 1994; Konno and Ohmachi, 1998; Bonnefoy et al., 2006). A number of studies have been conducted to investigate the applicability and reliability of the microtremor method in the health assessments of structures since 1990s. However, during the last two decades, microtremor recordings have become to be preferred due to their low cost and convenient operations (Tuladha et al., 2004; Chatelain et al., 2000; Ikeda et al., 2010). They are used to determine the structure dynamic behaviors (Brownjohn, 2003; Ventura et al., 2004), to evaluate the damage after earthquakes (Clinton, 2004; Dunand, 2006) and to assess the retrofitting results (Todorovska, et al., 2006; Celebi, 1998).

1.1.3 Numerical simulations about the dynamic characteristics of concrete structures

Compared to the field experiments, the numerical simulation usually provides an effective and relatively low-cost way to study the dynamic characteristics of structures. At present, the Finite Element Method (FEM) is commonly adopted to predict structure vibrations (e.g., Zaghloul and White, 1993; Uddin et al., 1994; Kuo et al., 1995; Dondi, 1996). The presence of discontinuities in numerical models, such as the interfaces between tunnel linings and surrounding rock masses, however, would undermine the calculation accuracy in some degree, especially when large deformations occur. The bodies of semi-infinite extent such as the half-space ground can be also dynamically analyzed by the boundary element method (BEM) (Lombaert,

et al., 2000; Grundmann, 1999; Rasmussen et al., 2001; Hirose, 2000). A better solution to the FEM problem of wave reflection at artificial boundaries is offered by the FEM/BEM combination method (Pan, et al., 1994; Pan and Atluri, 1995; Francois, et al., 2007). However, BEM computer programs are difficult to construct and the existing ones are not easily available (Niki, et al., 2011).

With the capability of simulating large deformations and non-linear dynamic calculation of discontinuities, the Distinct Element Method (DEM) has received extensive applications in recent years (Jiang et al. 2009; Zhang et al.1997). Zhao et al. (2006; 2008) conducted seismic wave propagation across single or multiple rock fractures by using the code of UDEC. Those simulation results, including the reflection and transmission coefficients and the influence of joint stiffness on wave propagation, showed good agreements with theoretical calculations.

So far, the traffic-induced vibration of tunnels and its propagation in the ground have been studied with both analytical and numerical methods, which focus on the ground-borne vibrations transmitting to the adjacent structures. The influence of the vibration source (the moving train) and the propagation path (the composition of the ground) of wave are mainly discussed. In order to simplify the modeling process, the ground is assumed to be continuously bonded to the outer surface of the tunnel, and the tunnel-ground interface is usually neglected. Displacement and strain is usually treated as compatible at the interface boundaries (Metrikine et al. 2000). Few attentions have focused on the vibration characteristics of tunnel itself, especially with the low amplitude ambient vibrations evoked by vehicle in road tunnel (Jiang et al. 2012). In those old mountain tunnels built with poling-board method, sound contact boundary conditions are hardly achieved and flexibility supports usually exist between the rock and the tunnel lining.

1.1.4 Void delineation in structures based on vibration intensity of microtremors

With the age-cold method of voids inspection, the lining voids can be identified by tapping the lining surface with the hammer and listening to the hollow drum sound. As impact-generated vibrations reflect between the lining and void surfaces, lining

concrete where the voids exist resonates weakly and produces airborne sound through seismic-acoustic wave conversion. Highly-experienced operators are essential in this kind of inspection due to the lack of specific criteria of judgment. On the other hand, it provides a possible approach for the void detection if the measured seismic waves could be digitized and quantified. Previous work by Sansalone and Carino (1986) showed that the impact-echo method could be used for detecting the voids or cracks in plate-like structures based on the wave reflection of internal defects. In addition, field studies on concrete structures were performed to verify the results obtained from numerical and laboratory studies (e.g., Cheng and Sansalone, 1993; Davis, 2003; Yu, et al., 2006).

Microtremor could be considered as a temporally and spatially stochastic process that contains propagating waves. Not only near-field vibration sources (e.g., traffic) but also far-field vibration sources (e.g., crustal motion) could induce microtremors. The wave propagation originating from the far-field vibration sources is also significantly affected by the internal structure of materials, which can be used to detect flaws existing in materials and to assess the integrity of structures. Numerous studies for the dynamic response of cavities or tunnels in the ground to plane elastic wave have been carried out since 1960s. Glazanov and Shenderov (1971) studied the plane wave scattering by a cylindrical cavity in an isotropic elastic medium. Fotieva (1980) studied the two parallel circular tunnels subjected to the compressional and the shear waves. Sancar and Pao (1981) gave the solution for the scattering of plane harmonic wave by two cylindrical cavities in an elastic solid. The tow-dimensional scattering and diffraction of SH wave by a circular hold has been studied by many researchers (Lee and Trifunac, 1979; Kundu and Bostrom, 1992, Ma1 et al. 1992). However, incident P (SV) waves, due to the complexity of the problem, most research is still in the methodology stage (Varadan, 1978). Few numerical results have been provided that can be used to guide engineering practice. The methods for solving these problems can be classified into the following two categories: analytical methods (such as laplace transform method, conformal mapping method, the wave function expansion method, the conformal mapping method, the wave function expansion

method and Fourier–Bessel series method, the curved beam theory) and numerical methods (such as boundary element method, finite element method, strip element method (Providakis, 1993; Shi, et. al, 1996; Stamos, 1995; Davis, et. al, 2001; Eisenberger and Efraim 2001; Okumura et al., 1992).

1.2 Object and thesis structure

With the research background given above, the overall object of this thesis is to investigate the relationship between the tunnel lining healthy state and its microtremor behaviors. The outline of this thesis is shown in Fig. 1.1.

Chapter 1 gives an introduction of the research background, objectives and the structure of this thesis. Chapter 2 summarizes three types of the most widely used non-destructive health assessment techniques of tunnel linings, including optical technique, electromagnetic technique and mechanical oscillation technique. Main applications, advantages and disadvantages of these technologies are compared and analyzed. Due to the limitation of the traditional inspection techniques, the vibration-based damage identification method attracts more and more attentions to analyze the health state of the tunnel lining. In Chapter 3, the expanded DEM (EDEM) with the function of simulating rock cracking was developed by implanting the tensile-shear failure criterion into the DEM code of UDEC, and it was utilized to investigate the natural frequency variation of the cracking reinforcement beam. The validity and accuracy of the EDEM were verified by comparing the numerical results with the experimental results. In Chapter 4, both the Love-Timoshenko shell theory and Donnell-Mushtari shell theory were adopted and extended to the elastic boundary conditions to analyze the vibration characters of tunnel lining, and the rock-concrete contacts were treated as elastic boundaries represented by the distributed springs. The void between concrete linings and rock masses was treated as the additional load and its influence on the natural frequency was estimated by the modal expansion approach. The validity and the accuracy of the proposed method were verified by the numerical results of the DEM code of UDEC. Chapter 5 introduces the in-situ microtremor

measurements on three spans of Satomi tunnel (the seriously damaged span S1, the moderately damaged span S2 and the healthy span S3). The microtremors were analyzed at the frequency domain (i.e., power spectral density (PSD)). The modal parameters including nature frequencies and damping ratios were extracted from the measured data. The relation between microtremor characteristics and the health conditions of tunnel was discussed. As an initial step, the in-situ measurements give clear evidence that the microtremor intensity characteristics have strong relation with the healthy conditions of lining concrete, which has the potential to be used in engineering practices. Comparing with theoretical and experimental studies, the numerical simulation provides a convenient and low-cost approach to study the dynamic problems, especially when theoretical solutions are difficult to obtain. In Chapter 6, a horse shoe shaped tunnel lining, of which the lining shape and the physico-mechanical properties of the surrounding rock mass and lining concrete are in accordance with the tested tunnel, was modeled to verify the in-situ measurements and to give a better understanding about the microtremor vibration behaviors. Rock-concrete contacts were represented by the interface element in UDEC. A stationary Gaussian white noise with power of 60 dBW and a frequency range of 0 to 100 Hz was input on the floor of tunnel in terms of a normal stress to represent the exciting source. The relationship between the normal stiffness of rock-concrete interface and the peak frequency was analyzed. The influences of the voids and their geometrical parameters, rock type and concrete type on frequency response of tunnel lining were studied. The relationship between the peak frequency and the stress state of the tunnel lining were also discussed based on the numerical results. Chapter 7 presents a void delineation method based on the vibration intensity of microtremors. In this method, white noise excitation is not indispensable and the vibration modal parameters (natural frequencies, mode shapes and dampings) are unnecessary to obtain by the modal identification procedure. The mean values of PSD were adopted to represent the vibration intensity of microtremors. The vibration intensity ratios of the microtremors of in-situ measurements and numerical simulations were analyzed. In the numerical simulations, not Gaussian while noise but the microtremors

measured at the healthy span were chosen as far-field vibration sources. Influences of the properties of rock-concrete interfaces, the voids and their geometrical parameters, and the mechanical properties of rock and concrete on the vibration intensity ratio of tunnel linings were also studied. Finally, major conclusions and some discussions of this thesis are provided in Chapter 8.

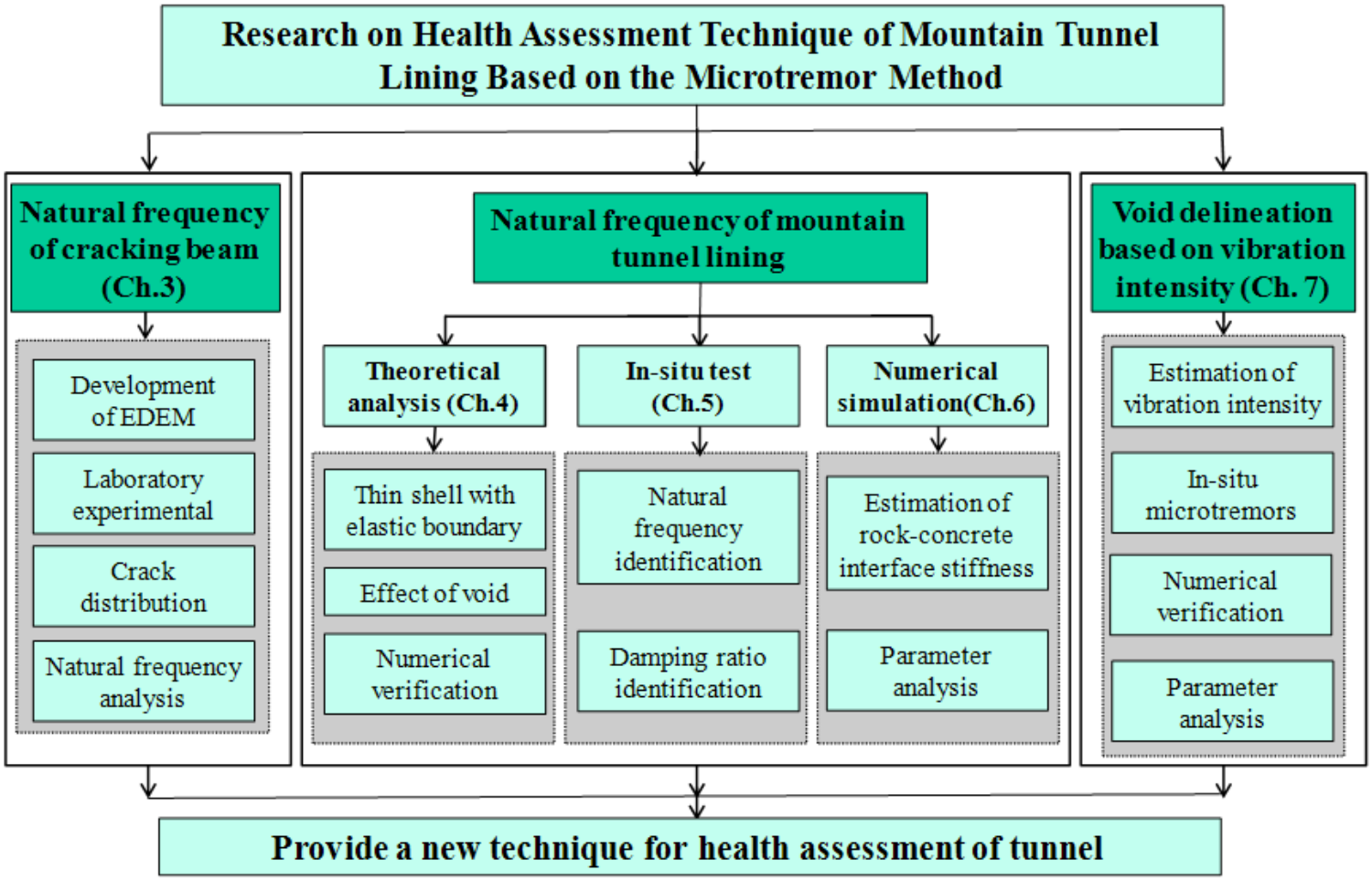

Fig. 1.1 Structure of the doctoral thesis

CHAPTER 2

A review of non-destructive health assessment techniques for tunnel lining

2.1 Introduction

Japan is a country surrounded by sea and 70% of its land is covered by mountains. A large number of tunnels have been constructed in mountainous areas during the last several decades, and those tunnels have become an indispensible part of the national traffic networks. To date, a great number of tunnels have been in service for more than 50 years. Fig. 2.1 shows the number of tunnels, which have been constructed for more than 50 years in Japan, according to Ministry of Land, Infrastructure, Transport and Tourism (2005). In Nagasaki, most of the tunnels were constructed since the year of 1965, with a total number of 123 until March of 2010. During these tunnels, about 17 tunnels have been used for more than 50 years. However, this number will increase 86 after 30 years, as shown in Fig. 2.2.

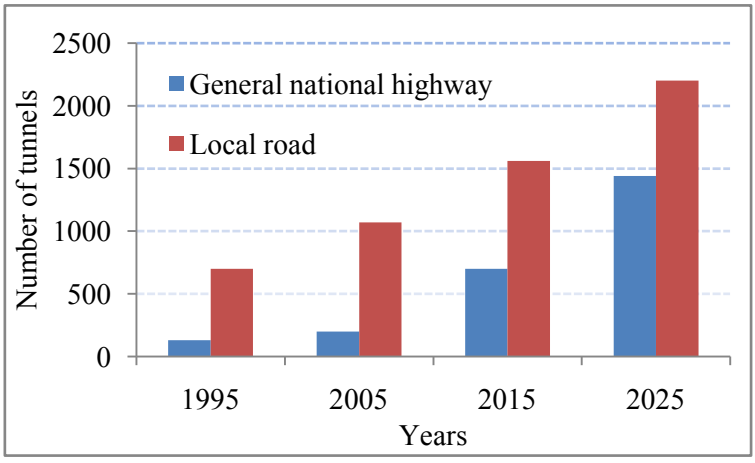

Fig. 2.1 The number of tunnels which have been constructed for more than 50 years.

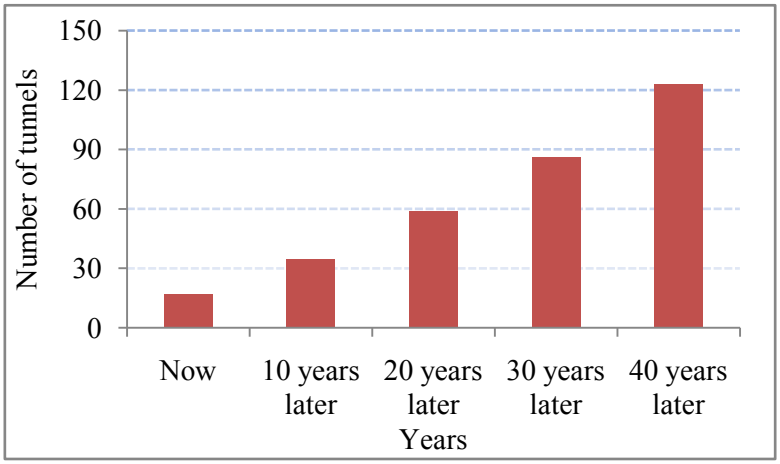

Fig. 2.2 The number of tunnels which have been used for more than 50 years in Nagasaki city

The persistent ageing of tunnels causes many problems on the lining of tunnel, such as corrosion, spalling, fracturing, generation of internal voids and seepage (Malmgren et al. 2005), as shown in Fig. 2.3. Deteriorations and damages of lining concrete decrease the integrity of tunnel lining and subsequently affect the workability, serviceability and safety reliability of tunnels (Aktan et al. 2000, Bhalla et al. 2005).

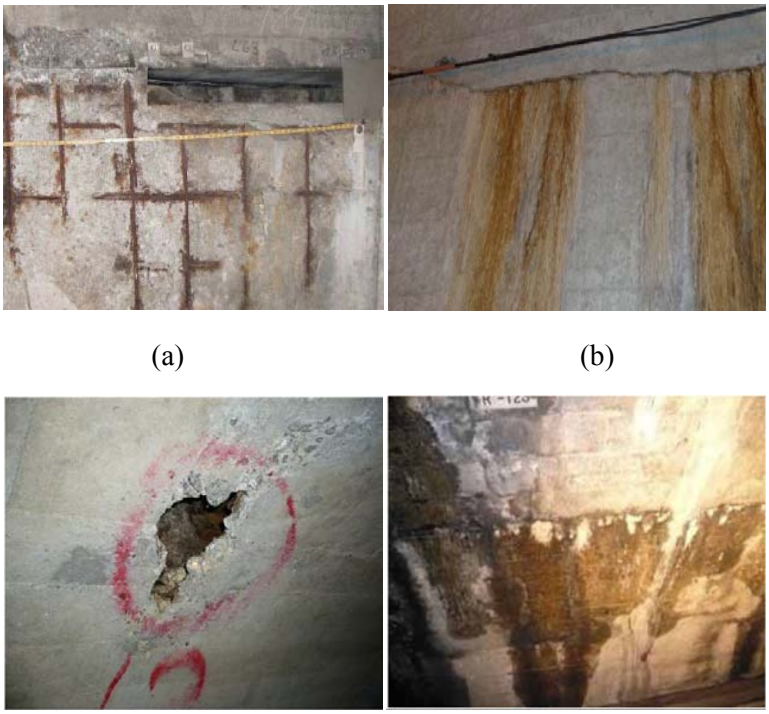

(a) (b)

(c) (d)

Fig. 2.3 Common persistent ageing problems of tunnel lining (Tomie, 2013).

(a) Concrete spalling. (b) Cracks. (c) Void behind the lining. (d) Seepage.

On February 2, 2012, about 1.2 tons' concretes dropped from the ceiling board of Sasako tunnel and buried 3 cars, causing 9 person died and 2 person injured. Fig. 2.4 illustrates the destruction process of the accident. One of the important reasons is the deterioration of the tunnel. Additionally, the accident also impacted logistics and passenger transport, resulting in huge economic losses. Therefore, routine maintenance which does not improve the quality level of the whole structure but it is necessary to guarantee the normal operation by slowing the deterioration process. The goals of the routine maintenance for tunnels are (Sandrone, 2011):

- Maintain the regular functions, in terms of both serviceability and safety, of the structure.
- Preserve the tunnel characteristics to guarantee its future life span and economical value.
- Estimate the tunnel performance in the future.

In order to achieve these goals, appropriate inspection needs to be conducted at appropriate time to ensure the effective function of tunnel. In this chapter, the widely used health assessment techniques of tunnel linings are reviewed and summarized. The advantage and disadvantages of these techniques are compared and analyzed.

Fig. 2.4 Demonstration of the destruction process (JDP news, 2012).

2.2 Non-destructive health assessment techniques for tunnel lining

To date, a number of inspection methods including destructive and nondestructive approaches have been proposed and used in practices to evaluate tunnel integrities (Abraham and Derobert, 2003; Haack, 1995; Richards, 1996). Table 2.1 summarizes the scope of advantages and disadvantages of the most widely used techniques of tunnel linings.

2.2.1 Optical techniques

(1) Visual inspection

The visual inspection is the detection of the visual changes on the tunnel surfaces. The cracks (length and width), concrete spalling (length, depth and width) and corrosion on the steel members (length, depth and width of the corrosion) should be recorded. These inspection works are mainly done via the human naked eye, hence the rapid and exact survey cannot be ensured especially in the extensive coverage areas and the results are influenced by the adverse working environments and the detector experiences. Moreover, the damages identified in this inspection are manually recorded on inspection sheets, entailing the limited use of databases, which are not typically stored in digital formats (Yoon, 2009). In order to overcome these problems, various technologies (such as laser beams, digital cameras, mobile robots), using film and filters that are sensitive to the visible light spectrum or to infrared wavelengths respectively, have been developed and applied (Ukai, 2007; Sasama et al., 1996; Sasama et al., 2006; Yu et al., 2007). Array of synchronised, overlapping off-the-shelf digital cameras used in the visual inspection of tunnel lining and its results are shown in Fig. 2.5 (Stent et al., 2013).

In tunnels, visual inspection has been used experimentally to detect cracks. With the development of the high resolution possible with this method, cracks as thin as 0.5 mm could be identified. Furthermore, concrete spallings, deposits of carbonate and moist patches, can be detected on surface of tunnel lining.

Table 2.1 Non-destructive health assessment techniques for tunnel lining.

Techniques		Main application	Problems with	Advantages
Optical technique	Visual inspection	Cracks; visual and geometrical defects	Speed; demand of powerful lighting; penetration depth;	Low cost; little skill required for the operator; detection of small and dry cracks on the surface of the tunnel lining; immediate data for viewing
	Infrared thermography	Voids, moist patches and cracks.	Influenced by water content and tunnel climate; unknown about depth of voids	high speed; remote detection; real time pictorial display
Electromagnetic technology	Ground Penetrating Radar	Voids, cracks and water; thickness measurement	Evaluation; wave energy attenuates; influenced by the presence of steel.	Deep penetration with high resolution in concrete ;depth information acquisition
Mechanical oscillation technique	Impact-echo	voids, eliminations and geometry of structure; bond quality of interfaces	demand of experience of the operator and the calibration test; not effective for detection of rebar and defects near surface ;	Relatively simple test to perform; commercially available test equipment; Effective for detecting interface state.

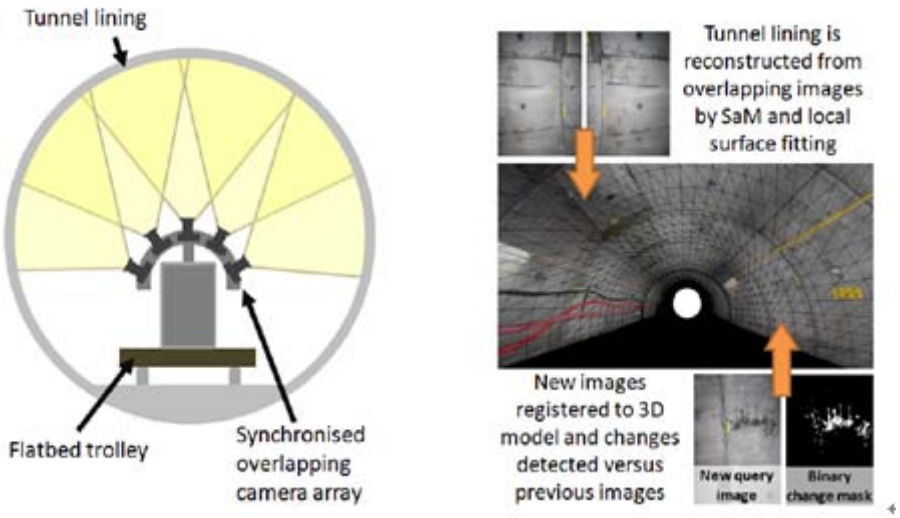

(a) (b)

Fig. 2.5 Overview of the visual inspection system via the camera (Stent et al., 2013). (a) Low-cost camera array for data capture. (b) Pipeline summary.

(2) Infrared thermography

Visual inspection can reveal the surface defects in the photograph pattern, while anomalies within the lining which are invisible to the eye could not be identified. A special visual inspection technique using infrared rays, which has been successfully applied in a number of engineering projects, e.g. the medical industry (Adams et al., 1998), the printing industry (Can, 1998), identification of buried mineshafts (Donnelly and Mccann, 2000), identification of canal seepage (Engelbert, et al., 1997) as well as various other civil engineering applications (Burnay, et al., 1988), is introduced in details in the following.

Most materials absorb infrared radiation, causing an increase in the temperature. All objects with a temperature higher than absolute zero (-273.15 °C or 0 K) radiate infrared energy within a range of wavelengths from 0 to∞ which is far beyond the spectral ranges of light visible of human. For technical infrared recordings, the middle infrared ranges (from about 2 to 6 mm or 8 to14 mm) are usually used (Boscomer, 1989). Infrared thermography is a technique for converting the measured thermal radiation (infrared rays), which is invisible to the human eye, into a visual temperature image. The equation for the

radiation of an object according to the Stefan–Boltzmann equation is (Drysdale, 1997):

$$E = \varepsilon\sigma T^4 \tag{2.1}$$

where E is the radiation (W/m^2), T is the temperature (K), σ is the Stefan–Boltzmann constant (5.67×10^{-8} W/m^2 K^4) and ε is the emissivity.

In tunnel, the thermal flow are usually induced by the gaseous material (e.g., air) or the liquid (e.g., ground water). The defects such as voids, as well as the changes of lining materials usually change the thermal flows and result in a pronounced increase or decrease in temperature. Hence, the possible defects in the tunnel lining can be identified by the infrared thermography distribution on the lining surface. In infrared thermography, differences in temperature from 0.1°C and upwards can be identified. Fig. 2.6 shows a typical infrared image of tunnel wall.

For the convenient use in tunnels, an infrared camera or scanner is generally mounted on a moving vehicle (e.g., a rail way wagon). The scanner basically surveys the entire t-nnel lining over its full area, so that the intensity of the thermal radiation of every element of surface amounting to 15 cm in size is registered and stored digitally. The measurements are recommended to be carried out in winter in which the temperature gradients are maximized and the temperature abnormalities are highlighted. The scanner must be set up in front of the measuring car in order to minimize the influence of waste heat (thermal radiation) on the thermal radiation pattern of the tunnel shell surface. Therefore, this method should be applied when traffic is forbidden. In addition to registering the temperature, a visual picture of the tunnel shell can be recorded by the scanner at the same time.

This technique is able to identify:

- ground water seepage in/behind tunnel lining;
- changes in the geological conditions behind the lining;
- changes of the lining materials;
- defects in the lining, such as voids, cracks.

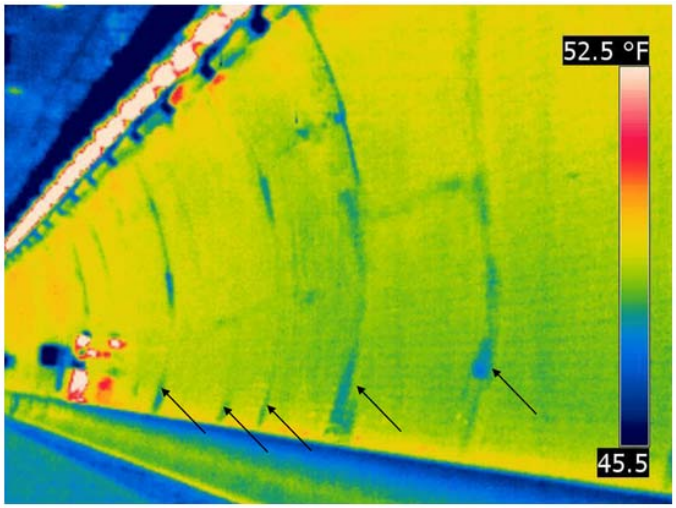

Fig. 2.6 Infrared image of tiled tunnel wall: areas in blue appear to be deboned tiles according to limited sounding tests (SHRP2, 2000).

The following limitations remain to be considered with regard to applying thermography in tunnels:

- The variation of water content over time often causes disturbance in the results.
- The thermal flow though the tunnel lining during the measurement should be constant in order to assess changes with the same experimental conditions.
- The low penetration depth providing information, renders it very difficult to assess the depth of an abnormality based on thermography alone.
- The tunnel lining should not have any coating or installation that prevents the thermal radiation penetration.

2.2.2 Electromagnetic techniques

Ground Penetrating Radar (GPR) is the most widely used electromagnetic investigation method, in which electromagnetic waves penetrate through the concrete or any other medium. The GPR was first manufactured for commercial purpose in the mid-1970s and was demonstrated as a useful geophysical tool (Lerner, 1974). In the 1980s, the digital system was brought in GPR to get a higher system performance and a deeper depth of penetration (Wills, 1992). From then on, the GPR became a standard tool for a variety of geophysical, engineering, and structural investigation applications (Bungey, 2004; Annan, et al., 2002; Jones, et al., 2006).

(1) Introduction

A GPR system consists of a control unit, a transmitting antenna, a receiving antenna and a device for saving and displaying the data, which can be integrated into the control unit. The transmitting antenna and receiving antenna are often assembled together for the convenient operation. The main wave frequencies used in GPR are between 80 and 1000 MHz. The short electromagnetic pulses (1 - 20 ns) is emitted by an antenna into the structure under investigation and the signal is reflected due to the changes in the electromagnetic properties of materials in the propagation direction. The percentage of the wave that is reflected is proportional to the difference of the dielectric constants (see Fig. 2.7). Reflection coefficient (k) for vertical incidence between two perfectly dielectric materials is given by:

$$k = \frac{\sqrt{\kappa_1} - \sqrt{\kappa_2}}{\sqrt{\kappa_1} + \sqrt{\kappa_2}} \tag{2.2}$$

where κ_1 and κ_2 are the dielectric constants of the two media (A-CUBED, 1983).

The conduct electricity of the material (see Table 2.2) has a major influence on the wave amplitude attenuation in the material. Meanwhile, the amount of wave attenuation or weaken is also influenced by the frequency of the waves. Therefore, reflection, conductivity and frequency are the major factors governing the penetration depth of the waves into the structure. An increase in the frequency or the conductivity decreases the penetration depth (Peter and Ulriksen, 1982).

The velocity at which the electromagnetic energy travels in the ground is important in determining the depth of reflectors. The propagation velocity was determined as (A-Cubed, 1983):

$$v = \frac{c}{\sqrt{\kappa}} \tag{2.3}$$

Where $c = 3\times10^8$ m/s is the speed of light in vacuum.

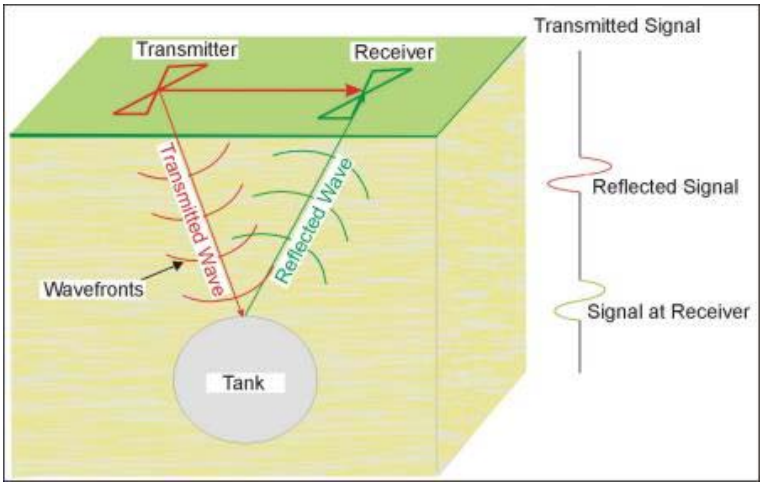

Fig. 2.7 Radar principles (U.S. Department of Transportation, 2014).

Table 2.2 Dielectric constant of common materials.

Material	Dielectric constant	Electric conductivity (ms/m)	Velocity (m/ns)	Attenuation (dB/m)
Air	1	0	0.3	0
Distilled water	80	0.01	0.033	0.002
Fresh water	80	0.5	0.033	0.1
Sea water	80	30000	0.01	1000
Pure ice	3 - 4	0.01	0.16	0.01
Saturated sand	20 - 30	0.1 - 1.0	0.06	0.03 - 0.3
Saturated silt	10	50	0.09	26
Silts(various)	5 - 30	1 - 100	0.07	1 - 100
Saturated clay	10	500	0.09	260
Clays(various)	5 - 40	2 - 1000	0.06	1 - 300
Limestone	4 - 8	0.5 - 2	0.12	0.4 - 1
Shales	5 - 15	1 - 100	0.09	1 - 100
Granite	4 - 6	0.01 - 1	0.13	0.01 - 1

(2) Data acquisition

Effective data acquisition is dependent on a well designed survey and effective implementation. Before the measurement, the main system parameters including single frequency, time window, sampling interval, single stacking and compensating should be adjusted based on the site condition and the information desired.

The time window is the duration over which the system records the returns at each

position. Appreciably larger than the maximum possible depth of interest is generally recommended to acquire the information as much as possible.

The antennas frequency determines the exploration depth that is possible. The larger the frequency is, the deeper the signal penetration becomes. Higher frequency antennas generate shorter waves and thus have finer resolution and can detect smaller objects.

Appropriate linear compensating should be chosen in order to acquire the clear reflection signals and the abrupt changes of the compensating should be avoided. Usually, manual gain is applied to equalize the signal amplitude.

(3) Data processing

During the measurement, the antenna is moved slowly and steady across the surface of the structure as shown in Fig. 2.8. The GPR data are common plotted in a two-dimensional cross section with position plotted on the horizontal axes and time (or depth) on the vertical axes. The depth axis assumes a constant velocity to estimate the penetrate depth. In tunnel lining inspections, the GPR cross-section can be viewed as a depth section along the road direction.

In order to make a better data interpretation and reduce clutter, the raw data must be processed. Initially, we eliminate the bad traces which are beyond the measurement range. Data may be filtered by band-pass filter or/and background removal in the field to remove noise, or the raw data may be recorded and the data processed for noise removal at a later time. The band-pass filter is applied to remove the possible low and high frequency signals, and the background removal is used for high pass filtering. There are also a number of more advanced filtering techniques such as migration that are occasionally employed to solve a specific problem with the data set due to the time consuming in data processing. However, it is important to note that data processing should not distort the data radically or alter their nature and should not introduce spurious features (Diamanti, et al., 2008).

Fig. 2.8 An example of data collection of GPR.

(3) Data interpretations

Reflections against boundary layers between materials with different dielectric constants can occur. Different types of defects, which has different boundary shapes, also results in various reflection characteristic (e.g., continuous line, hyperbola, or multiple discontinuous chaotic reflections), as shown in Fig. 2.9. By comparing the reflection character to known examples, a better interpretation of the reflection data can be constructed to analyze defects.

- The targets such as the steel arch and the void usually appear a hyperbolic curve, as shown in Fig. 2.9a. The transmitted radar wave propagates through the surface of the concrete and transmitted through the concrete diverges at a wide angle, typically 45° on each side of the normal, so that defects are recognized before the antenna is located directly above them. As the antenna moves on the surface of

the concrete, towards a defect, the defect's reflection time becomes shorter. When the antenna is located just on the top of the defect, the reflection time is shortest. After that, the reflection time increases. As a result, a typical radar single similar with hyperbolic curve is obtained.

- The discontinuities between two adjacent lining segments induces a small dip or break in the continuous reflections, as shown in Fig. 2.9b.
- The interface between two kinds of materials with different dielectric constants (e.g., the interface between metal and concrete) shows a continuous line, as shown in Fig. 2.9cd.
- The obvious strong wave reflections are produced by damage, whereas, there are just signal perturbation (produced by noise) in no damage area of homogeneous concrete, as shown in Fig. 2.9e.
- The concrete with low compaction shows the multiple discontinuous chaotic reflections, , as shown in Fig. 2.9e.

The void bottom boundary may also induce a secondary hyperbolic image or a continuous line reflection. However, no enough energy reaches the void bottom to produce an obvious reflection especially the void filled with water, due to the most energy is reflected at the sub-surface of the void. Meanwhile, the steel arches with dense arrangement in tunnel lining also reflect and absorb most energy, resulting in an significant reduction of the detecting depth. A skilful and experienced operator can often make a meaningful interpretation by recognizing characteristic patterns in these results.

(4) Main application and limitation

In tunnel engineering, this technique is able to identify:

- Changes in the geological conditions, such as groundwater, interfaces between the lining and the ground;
- Constituent materials of the tunnel lining, such as reinforcement, arches, etc;
- Thickness variations, such as concrete thickness;
- Abnormalities in the lining, such as voids, cracks.

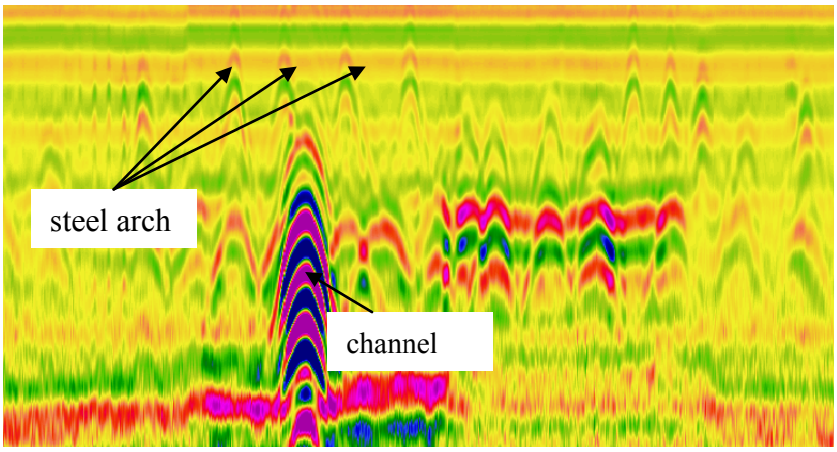

(a)

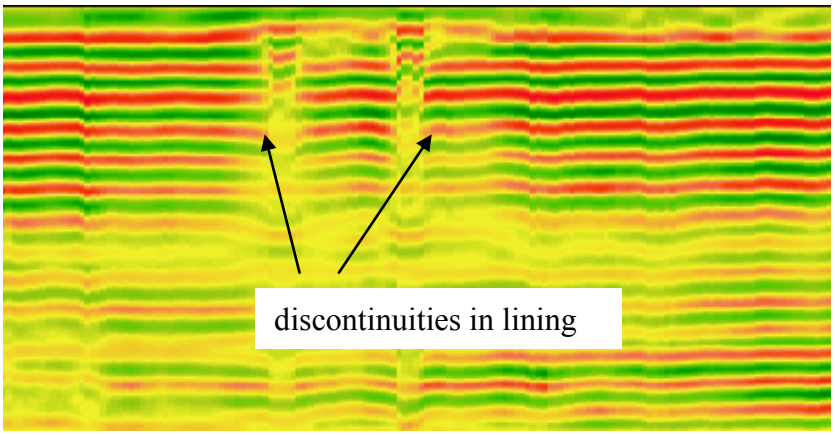

(b)

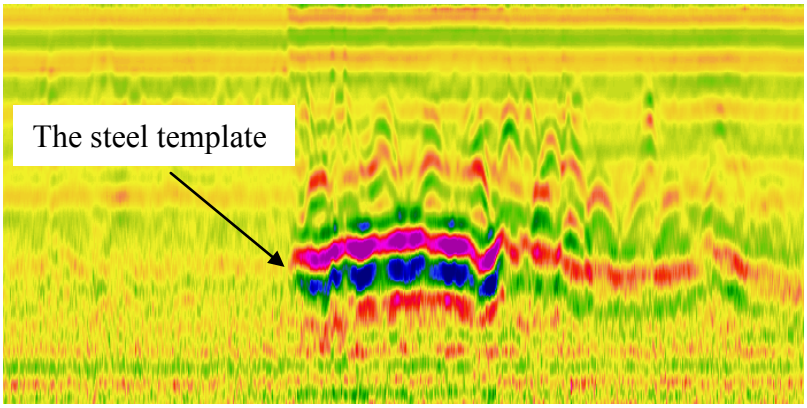

(c)

Fig. 2.9 The typical radar signals induced by defects. (To be continued)

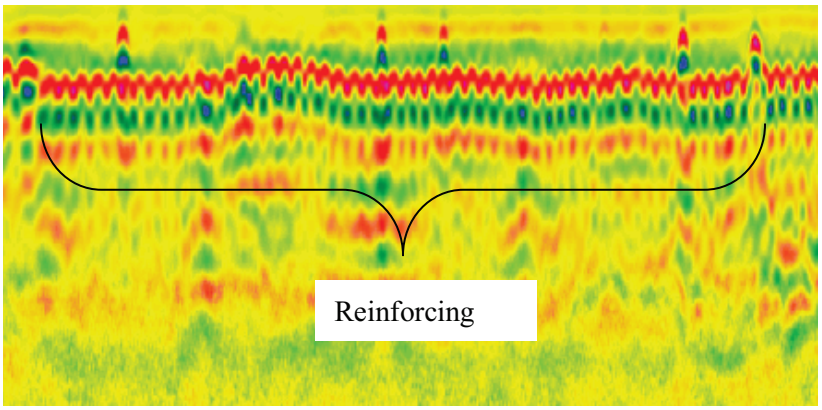

(d)

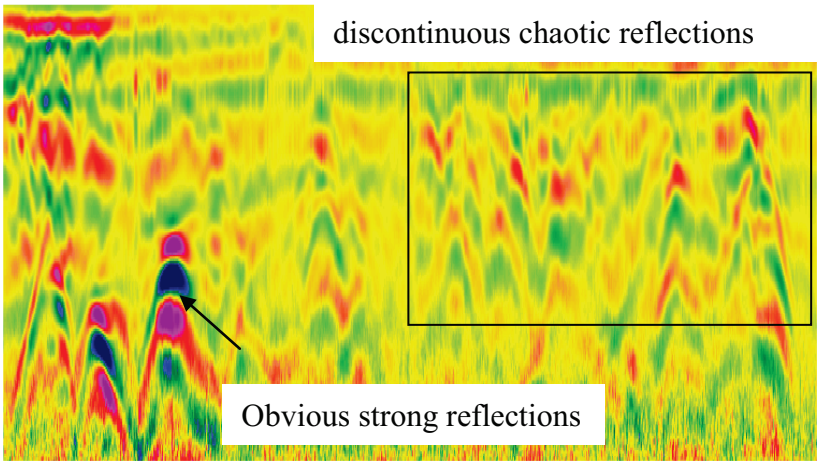

(e)

Fig. 2.9 The typical radar signals induced by defects. (a) The hyperbolic curve reflections induced by the channel and steel arches. (b) The discontinuities in lining. (c) The steel template left in lining. (d) The reinforcing mesh. (e) The obvious strong wave reflections and multiple discontinuous chaotic reflections.

There still are limitations in applying GPR method for tunnels:

- Interpretation of radar signals is generally non-intuitive to the novice;
- The bottom of the void is difficult to identify;
- Wave energy attenuates quickly in water and soil;
- The detection of defects is difficult due to the presence of steel.

2.2.3 Mechanical oscillation techniques

(1) Introduction

With the development and application of high sensitivity accelerometer, the low-cost vibration test has attracted much more attentions for evaluating the structural condition of

the whole structure of tunnel lining. Impact-echo is a technique based on the use of transient stress (sound) waves for the last 30 years. A short-duration mechanical impact (usually produced by tapping a small steel ball/hammer against a concrete surface) generates low frequency stress waves that propagates in to the structure and are reflected by the defects, interfaces or other surfaces (Carino and Sansalone, 1984).

This method was initially used to detect flaws in plate-like structures and was expanded in the experiment with the field instrument in 1992 (Pratt and Sansalone). The impact echo response of plates was firstly simulated by the finite element method, and the transient stress wave propagation in bounded solids with and without flaws were analyzed by the permitted detailed cases. These numerical studies provided an indispensable guide for the interpretation of experimental results. Finally, the basic capabilities of the method were established by a combination of numerical studies and companion controlled-flaw studies (Sansalone and Carino, 1988a, 1988b). Preliminary research also demonstrated the feasibility of using impact-echo testing to monitor setting and early-age strength development of concrete (Pessiki and Carino, 1998). So far, this method has been extended to the inspection of many concrete structures, particularly plate-like elements such as floor slabs, walls and large cylindrical structures (Davis, 2003, 2005).

(2) Theory

The surface vibration caused by the reflections are recorded by a transducer located adjacent to the impact and the vibration history is transform to frequency domain. The stress waves propagate through the structure at three different types of stress waves (a P-wave, an S-wave and an R-wave). The P- and S-waves travel into structure and reflect by internal and external boundaries and cause periodic displacements on the surface. If the transducer is placed close to the impact point, the response is dominated by P-wave echoes (Sansalone and Carino, 1986). Fig. 2.10 is a schematic of an impact-echo test on a plate with a large air void below the surface.

The periodic displacements on the surface are induced by the multiple reflections between the structure surface and the reflecting interface of defects. The frequency of the periodic displacements, f, can be approximated as:

$$f = \frac{C_{pp}}{h} \tag{2.4}$$

where C_{pp} is the P-wave speed through the thickness of the plate and h is the depth of the reflecting interface. The waveform is transformed into the frequency domain bu the fast Fourier transform technique, so that the periodicity of stress-wave arrivals can be accurately determined (Bracewell, 1978). For plate-like structures, the frequency associated with thickness usually be the dominant peak in the spectrum. The value of the peak frequency in the amplitude spectrum can be used to determine the depth of the reflecting internal flaws or external boundaries by expressing Eq. (2.4).

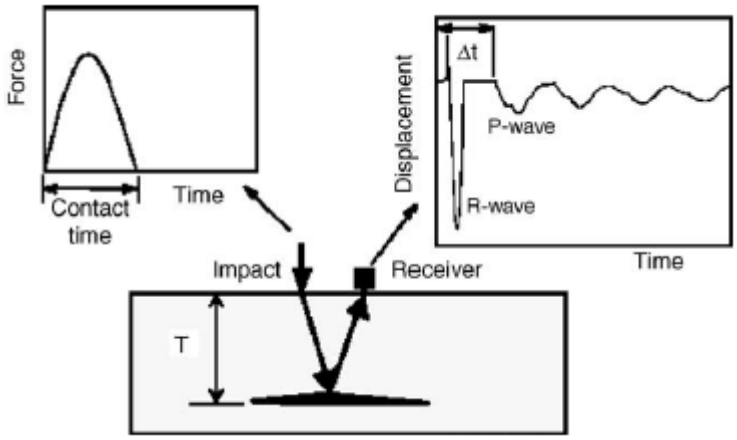

Fig. 2.10. The impact-echo method (Sansalone and Carino, 1986).

(2) Main application and limitation

The impact-echo method has been successful in detecting:

- Structure geometry, such as plates, circular or rectangular bars (columns or beams), hollow cylinders.
- A variety of defects, such as voids and honeycombed concrete in structural members, eliminations in bare and overlaid slabs, and voids in tendon ducts.
- The quality of the bond between an overlay and base concrete.

There still are limitations of this method for tunnels:

- The method is subjective, as it depends on the experience of the operator for data

interpretation.

- The wave alteration increases as the presence of water and clay increases, and it is limited to detecting near surface defects.
- A calibration is needed in order to determine the location of the damage.
    - Not effective for rebar detection.

2.3 Summary

In this chapter, three types of non-destructive health assessment techniques (Optical technique, electromagnetic technology and mechanical oscillation technique), which have wide applications in the inspection of in-situ tunnel lining, are presented in this chapter. Main applications, advantages and disadvantages of these technologies are compared and analyzed.

Visual inspection and infrared thermography techniques have low cost and easy operations, while it has the limitation of penetration depth and is influenced by the coating or installation on the surface of tunnel lining.

Impact-echo technique is effective for detecting defect interface in the lining concrete, while additional calibration is necessary and interpretation of data is very slow.

The application of Ground Penetrate Radar (GPR), which is introduced in details in this chapter as the most widely used method for tunnel lining inspection, still have many limitations and could not be proper in many cases and considerable time and cost are required to estimate the overall structural integrity.

A lot of tunnels have been in serve in over 50 years, and the maintenance of those old tunnels becomes to be an indispensable task. These techniques mentioned above all depend on the experiences of the operator for data interpretation and cannot be continued with the decrease of labor force and the increase of engineering quantities. It is necessary to make continued efforts on inspection technology to maintain the safety of old tunnels.

CHAPTER 3

Expanded Distinct Element Method and its application on the natural frequency of structure cracking.

3.1 Introduction

The damages in an elastic structure result in a localized reduction of the strength and stiffness of the whole structure. It has been found that the vibration modal parameters (e.g., the natural frequencies and damping ratios) of concrete structures are significantly sensitive to their damage status (Konno and Ohmachi, 1998). Meanwhile, the modal parameters can be acquired conveniently by dynamic tests (Vestroni and Capecchi, 2000; Lee, 2004), which provides a possible approach for effectively detecting the defects between the tunnel lining and the rock mass. One form of the damages that can lead to catastrophic failure is cracking of the structure elements (Chondros, et al., 1998). To analyze the mechanisms of cracking, a number of micromechanical models have been proposed on the basis of theoretical and experimental studies. However, most of those models focus on individual cracks and incapable of dealing with engineering problems with complicated elastic structures and boundary conditions.

With the rapid development of computing technologies in recent decades, the numerical simulation has become an effective and low-cost method to investigate the failure and vibration behavior of structures to handle complicated engineering problems. Currently, a number of numerical studies focusing on the crack growth problems have been performed by using the finite element method (FEM) (Bouchard et al., 2001 and 2005; Wong et al., 2002) and the boundary element method (BEM) (Lauterbach and Gross, 1998; Singh et al., 1998). In the FEM and DEM, the initiation and propagation processes of cracks are usually represented by using two approaches: the first one describes the cracking process as the evolution of damage through the material when the stress exceeds its critical value (the degradation of mechanical properties of the surrounding elements near the crack tips); and the second one simulates the crack growth by separating crack edges, which is accompanied by the continuous rebuilding of meshes near the crack tips according to the direction of crack propagation (Bouchard et al., 2000). Although those two approaches are widely used in numerical studies, the still have some shortcoming: the first approach cannot represent well the displacement discontinuity characteristic of cracks, which is important for estimating the mechanical behavior of rock masses; and the second one will face the difficulty of model remeshing at each step of the crack growth, which is a tough

and time-consuming problem.

Comparing with the traditional FEM and BEM, bound, the distinct element method (DEM) has attracted more and more attentions due to its inherent advantage in simulating the separation and slipping of cracks. Thereby, the DEM has been widely used in previous studies to estimate the mechanical and deformational behavior of cracks in engineering structures (Kulatilake et al., 1992; Souley and Homand, 1996; Shen and Barton, 1997; Suorineni et al., 1999; Jiang et al., 2000, 2001 and 2006). To investigate the failure process of rock mass, Jiang et al. (2009) and Nakagawa (1999) proposed an Expanded Distinct Element Method (EDEM) based on the DEM code of UDEC, and used this new method to simulate the cracking of large-scale rock structures due to tensile and shear failures. In this method, a mass of potential cracks with high strength are pre-defined in the regions where new cracks will likely be generated. When the tensile-shear criterion is satisfied, the potential cracks will be converted to real cracks and assigned with proper mechanical properties. The EDEM provides a novel way to address the failure problems of rock masses, which overcomes the difficulty of model remeshing without sacrificing the displacement discontinuity feature of rock fractures.

In this chapter, the EDEM based on the DEM code of UDEC is further developed and is applied to investigate the natural frequency of reinforcement concrete beam under loading. The tensile-shear failure criterion adopted by Jiang et al. (2009) has been implanted into the framework of EDEM to determine the initiation and propagation of 2-D cracks and to analyze the failure patterns of RC beam. To verify the validity and accuracy of this new numerical method, a loading experiment with RC beam was performed. The crack distributions and natural frequencies in different loading stages were recorded and compared with the numerical results.

3.2 Description of Expanded Distinct Element method (EDEM)

3.2.1 Introduction of the UDEC

In UDEC, the model is represented as an assembly of discrete blocks. The contact forces and displacements at the interfaces of a stressed assembly of blocks are found through a series of calculations which trace the movements of the blocks (Itasca, 2000). The stress wave propagation caused by applied loads or body forces can be simulated by the movements of the bock system.

The dynamic behavior is represented numerically by a timestepping algorithm in which the size of the timestep is sufficiently small so that velocities and accelerations are constant within the timestep, and during a single step, disturbances cannot propagate between one discrete element and its immediate neighbors. This solution scheme is identical to that used by the explicit finite-difference method for continuum analysis.

The calculations performed in the distinct element method alternate between application of a force-displacement law at all contacts and Newton's second law at all blocks. The force-displacement law is used to find contact forces from known (and fixed) displacements. Newton's second law gives the motion of the blocks resulting from the known (and fixed) forces acting on them. If the blocks are deformable, motion is calculated at the gridpoints of the triangular finite-strain elements within the blocks. Then, the application of the block material constitutive relations gives new stresses within the elements. Fig. 3.1 shows schematically the calculation cycle for the distinct element method. The equations in this figure are described in the following sections (Itasca, 2000).

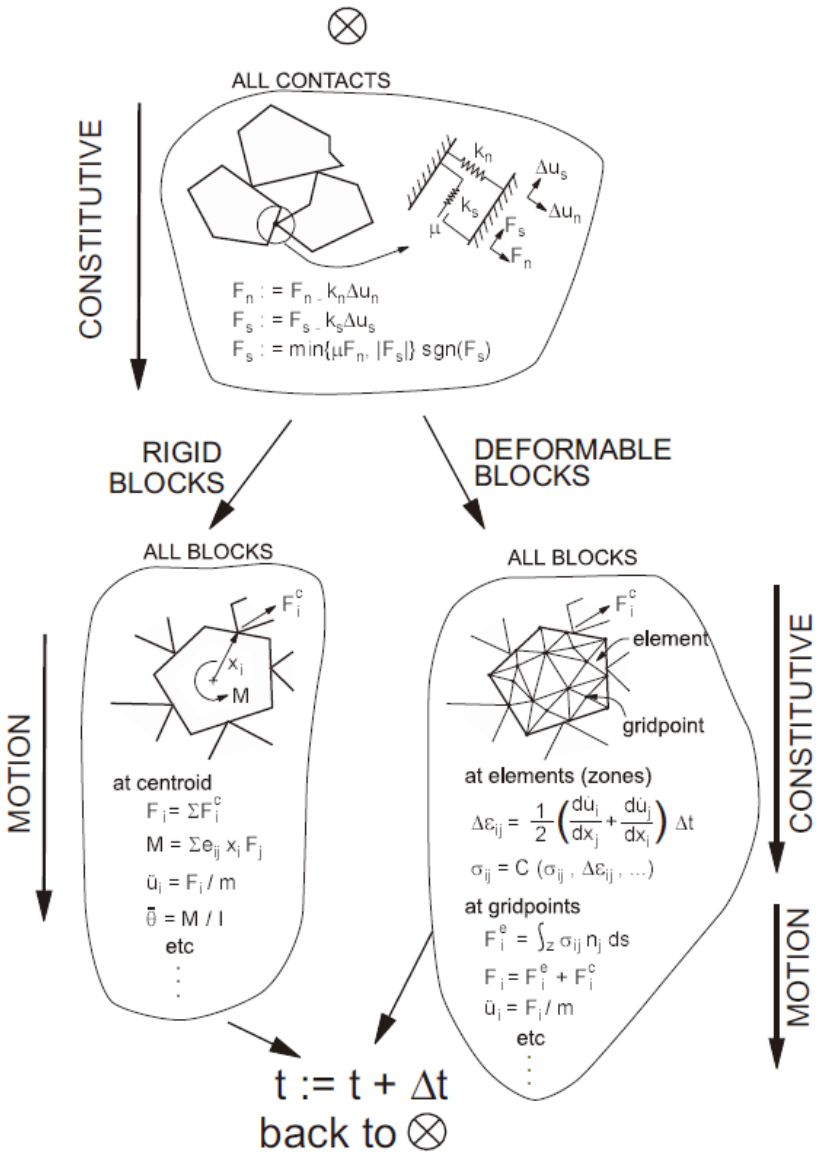

Fig. 3.1 Calculation cycle for the distinct element method (Itasca, 2000).

3.2.2 The principle of EDEM

The Universal Distinct Element Code of UDEC represents the rock mass as an assembly of discrete blocks and the fractures as interfaces between rock blocks. This code can realistically model the mechanical behavior (compression, slipping and separation) and geometrical properties (orientation, gap and spacing) of fractures, and thereby has a broad variety of applications in rock mechanics (Itasca, 2000). To simulate the cracking and failure of rock masses, the EDEM was developed within the UDEC framework by introducing specific rock mass failure criteria into the DEM, which accompanied by the processes of crack generation, propagation and coalescence. Fig 3.2 shows the flow chart of the EDEM, representing the basic principles of this method. The realization of crack initiation and propagation in an EDEM model mainly falls into four procedures: 1) definition of potential cracks in the model; 2) stress calculation for all contacts located at interfaces; 3) safety/failure judgment for all contacts; and 4) conversion of potential cracks into real cracks if a certain failure criterion is satisfied.

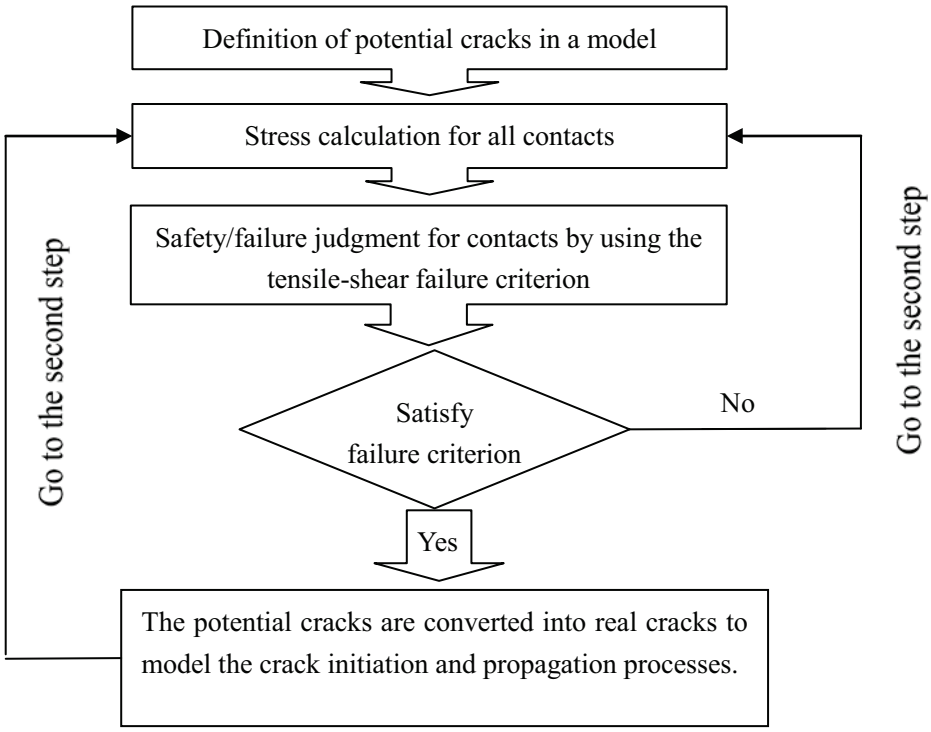

Fig. 3.2 The flowchart representing the processes of crack initiation and propagation based on the EDEM.

In the EDEM, a special treatment is performed by introducing six sets of gapped joints into the model, which separate the intact rock matrix into an assembly of hexagonal blocks, as shown in Fig. 3.3. The interfaces between blocks represent the potential cracks, which have a large bonding strength and act like the rock matrix before failure happens. Each hexagonal block is connected to adjacent blocks via point contacts located at the potential cracks, as shown in Fig. 3.3. The contact can be considered as a boundary condition, which applies external forces to each block. A number of triangular zones (meshes) are generated in each block to calculate the internal stress and strain. The principal stresses for a contact, which are used to determine the failure of safety status of the contact, can be estimated by using the average stress of four surrounding zones that have the shortest distances from the centroids of zones to the contact (e.g., the four zones denoted by Z_{A1} & Z_{A2} in Block A and Z_{B1} & Z_{B2} in Block B in Fig. 3.3). Assuming that the average stress tensor for four surrounding zones is and (under the plane strain condition), the principal stresses (σ_1, σ_2 and σ_3) at the corresponding contact can be calculated by using the expressions of elastic theory, as shown in Eqs. (3.1), (3.2) and (3.3).

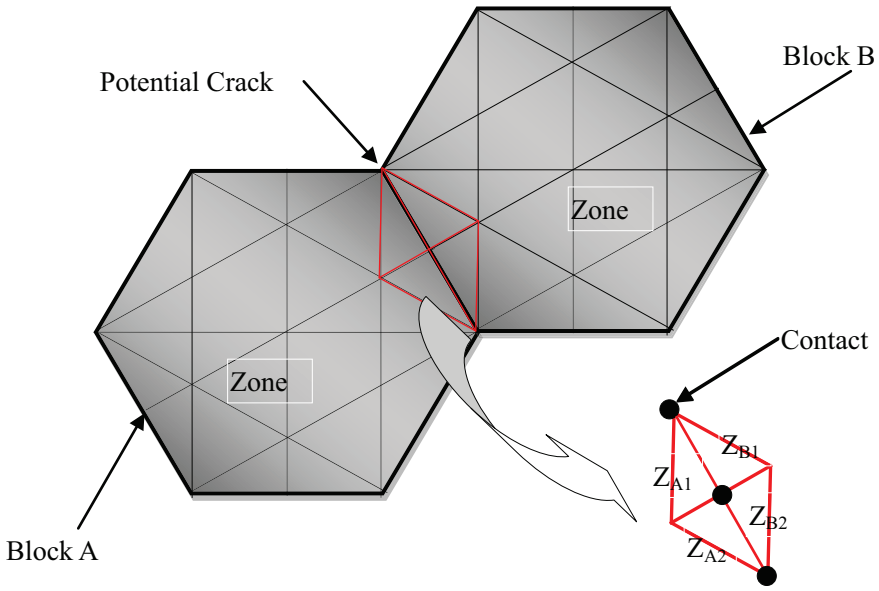

Fig. 3.3 The basic structure of the EDEM model and the determination of principal stresses at the contacts in the rock matrix.

$$\sigma_1 = \frac{\sigma_x + \sigma_y}{2} + \sqrt{\left(\frac{\sigma_x - \sigma_y}{2}\right)^2 + \tau^2_{xy}} \tag{3.1}$$

$$\sigma_2 = \frac{\sigma_x + \sigma_y}{2} - \sqrt{\left(\frac{\sigma_x - \sigma_y}{2}\right)^2 + \tau^2_{xy}} \tag{3.2}$$

$$\sigma_3 = \sigma_Z \tag{3.2}$$

It should be noted that these principal stresses are renumbered conventionally in descending order of magnitude, $\sigma_1 \geq \sigma_2 \geq \sigma_3$, so that they are the maximum, intermediate and minimum principal stresses.

To evaluate the safety/failure status of contacts, the tensile-shear failure criteria (Jiang et al., 2009) is adopted in the EDEM. The tensile-shear failure criterion has been widely adopted in rock mechanics and engineering practices because it can comprehensively describe the failure behavior of rock mass when subjected to tensile and shear stresses, as expressed in Eqs. (3.4) and (3.5) as bellows:

$$\sigma_3 = -\sigma_t \qquad \text{(for tensile failure)} \tag{3.2}$$

$$\sigma_1 = \frac{(1+\sin\varphi)\sigma_3}{1-\sin\varphi} + \frac{2c\cos\varphi}{1-\sin\varphi} \qquad \text{(for shear failure)} \tag{3.2}$$

where cymbols c, φ and σ_t denote the cohesion, the internal friction angle and the tensile strength of the rock or rock-like materials, respectively.

At each calculation step during the EDEM simulation, the principal stresses at all contacts that are located on potential cracks are calculated and substituted into the expressions of the tensile-shear failure criterion. For a low stress level, the failure of rock-like materials cannot occur, and the numerical simulation will move to the next loading step. When a certain failure criterion is satisfied for a contact due to the increased stress, the sections of a potential crack, which belongs to that contact, are converted to real cracks with the proper mechanical properties, representing the initiation and propagation of cracks. Through the procedures mentioned above, the failure process of rock and rock-like materials under various loading conditions can be simulated.

3.2.3 The verification of the natural frequency estimated by EDEM

To verify the validity of natural frequency identification of EDEM, numerical simulations about the impulse response of a beam were performed.

A two-dimensional EDEM model with the dimension of 10×1500 mm (height×length) was established, as shown in Fig. 3.4. The physico-mechanical properties of the concrete used in simulation were listed in Table 3.1 (Hatanaka et al., 2010). The properties of potential cracks are carefully chosen by calibration case studies to ensure that before the potential cracks change to real cracks (i.e. crack initiation), the natural frequencies of the numerical model are identical to theoretical solution. Due to no failure occurs before loading, the cohesion force, the friction angle and the tension strength have no influence on the vibration behaviors of the beam. Hence, only the influences of the stiffness of the potential cracks were analyzed. A group of potential cracks with different stiffness were simulated, as listed in Table 3.2.

A static equilibrium calculation was achieved before the start of dynamic analyses. In dynamical calculations, a short duration impulse with a frequency of 500 Hz was input on the top of beam in terms of a normal stress to represent the impulse induced by the hammer. The Rayleigh damping with a ratio of 0.7% was utilized during dynamic calculations to represent the attenuation of materials. 16384 discrete time signal data at each monitoring point were recorded during numerical simulations with a sampling interval of 0.001s. The natural frequency can be acquired by the Fast Fourier Transform (FFT).

The natural frequencies of numerical and theoretical solutions are plotted and compared in Fig. 3.5. The numerical results show that the natural frequency increases linearly with the increase of the crack stiffness until reaches the theoretical solution 158.2 Hz (Bishop and Johnson, 1956). The natural frequency of case P-C-3 is most closely to the theoretical value. Hence, the stiffness of this case can be used as a standard in the following simulations.

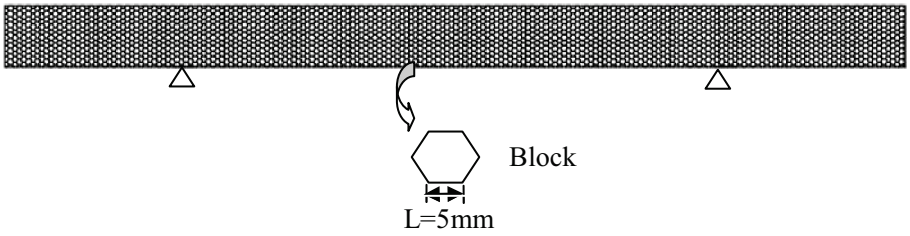

Fig. 3.4 The two-dimensional EDEM model of the concrete beam.

Table 3.1 Physico-mechanical properties of the concrete (Hatanaka et al., 2010).

Materials	Parameters	Units	Concrete
Concrete	Density	kg/m^3	2500
	Elastic modulus	GPa	33
	Poisson ratio	-	0.28
	Tensile strength	MPa	3.5
	Cohesion	MPa	2.7
	Friction angle	°	37

Table 3.2 Physico-mechanical properties of the potential crack.

Case	Normal stiffness (GPa/m)	Shear stiffness (GPa/m)
P-C-1	100	100
P-C-2	1000	1000
P-C-3	10000	10000
P-C-4	100000	100000

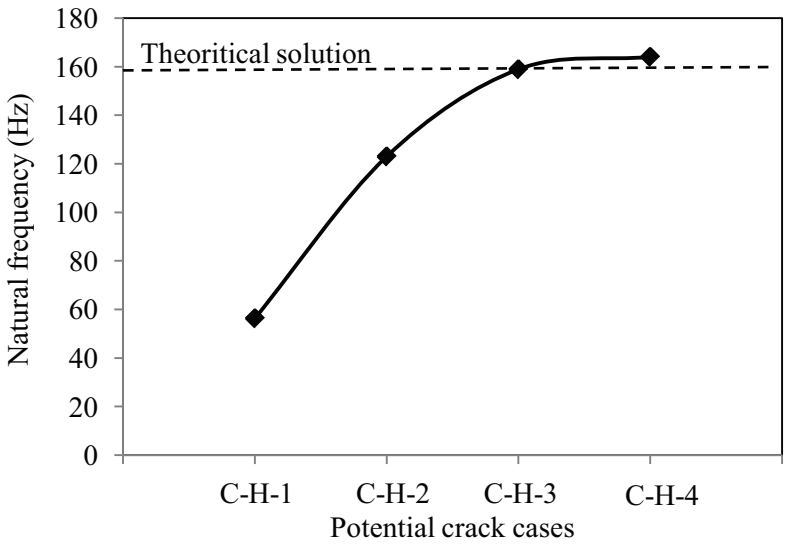

Fig. 3.5 Influence of the potential crack stiffness on the natural frequency of the beam.

3.3 Experimental tests about natural frequency measurement of the progressively cracking reinforced concrete (RC) beam and numerical models

3.3.1 Experimental preparation

Makino (2013) carried out an experiment to study the influence of the progressively cracking RC beam on its natural frequencies. A reinforcement concrete beam with the cross section of 100×100 mm (width×height) and span length of 1500mm (length)s was casted and tested, as shown in Fig. 3.6. The two-point loading with different values (e.g., 10kN, 20 kN, 25 kN and 30 kN) were applied on the middle of the beam in four stages. A schematic view of the loading test is shown in Fig. 3.7. A displacement meter was installed on the bottom at the mid-span to record the displacement in the vertical direction.

When the beam is statically loaded up to the designed level in each stage, the cracks of the tested beam will be recorded. And then, the beam is unloaded and is carried on the rubber supports in which the natural frequency will be measured, as shown in Fig. 3.8. A model analysis was performed to acquire the natural frequency. An impact hammer, which can apply a large frequency bandwidth impulse, was used to induce a vertical free vibration of beam, and accelerometer was fixed at the bottom of the beam to record the vibration response. The natural frequency can be acquired based on the frequency response. After the vibrations were measured, the beam was loaded in next stage.

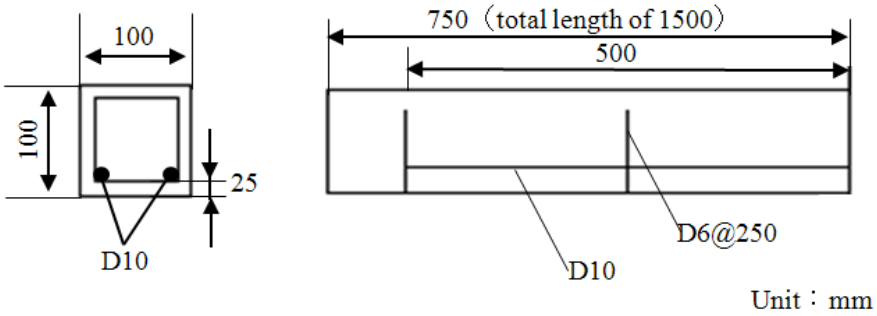

Fig. 3.6 The reinforced concrete beam.

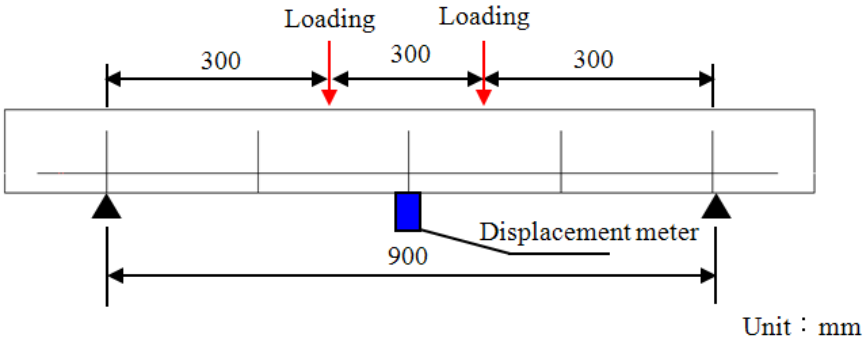

Fig. 3.7 The schematic view of loading experiment.

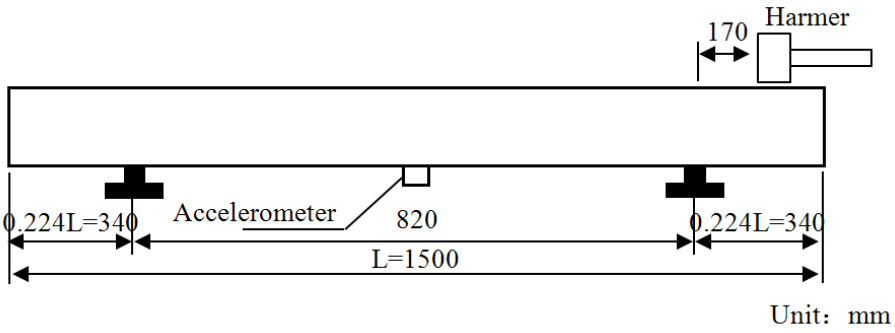

Fig. 3.8 The schematic view of vibration test.

3.3.2 Establishment of EDEM models

Corresponding to the experimental beams mentioned above, two-dimensional EDEM models with the same dimension of 10×1500 mm (height×length) was established, as shown in Fig. 3.9. To accurately simulate the propagation and coalescence of cracks, a large number of hexagonal blocks were created throughout the entire model with a side length of L=1cm. The interfaces between hexagonal blocks, which were pre-defined as potential cracks, represent the potential growth paths of cracks. When a certain failure criterion (the tensile-shear failure criterion) is satisfied, the potential cracks can be converted into real cracks by changing their mechanical properties. At the beginning of numerical simulations, the mechanical properties of the potential cracks should be chosen carefully based on lots of calibrations to ensure that the model behaves identically to the intact beam before the cracking occurs. After the hexagonal blocks were created, a mass of triangular zones (meshes) with the maximum side length of 1 cm were also generated in the interior of the hexagonal blocks to estimate the stress and deformation in the

concrete matrix during simulations. The internal zones divide potential cracks into smaller sections. Therefore, the cracking process can be executed section by section, which improves the accuracy of simulations.

The Mohr-Coulomb model and Coulomb slip model were adopted to represent the mechanical behavior of rock mass and pre-existing & newly-generated cracks, respectively. The cable element was used to simulate the reinforcement bar in the beam. Those types of elements can effectively simulate the dynamic deformational behavior of concrete, cracks and reinforcement bars. The physic-mechanical properties of the concrete and rebar are as listed in Tables 3.1 and 3.3 based on the typical properties of concrete and rebar used in the experiment (Hatanaka et al., 2010). For newly-generated crack, its mechanical properties listed in Table 3.4 can be estimated by using the test approaches described by Jiang et al. (2004) and Li et al. (2010). The high performance direct shear test apparatus, which supports the shear tests under both Constant Normal Load (CNL) and Constant Normal Stiffness boundary conditions, was adopted to evaluate the mechanical properties of the cracks.

The normal loading tests on concrete samples containing single fractures were performed to measure the normal stiffness of crack, and the direct shear tests under different normal stresses were carried out to measure the shear stiffness, the internal friction angle and the cohesion of the crack. Reducing 3D problems with regularly spaced reinforcement bars to 2D problems involves averaging the effect in 3D over the distance between the elements. Donovan et al. (1984) suggest that linear scaling of material properties is a simple and convenient way of distributing the discrete effect of elements over the distance between elements in a regularly spaced pattern. The element spacing, S=0.05 m, can be used to scale the reinforcement bar properties (i.e., elastic modulus, tensile yield strength, compressive yield strength listed in Table 3.4.).

A static equilibrium calculation was achieved before the start of dynamic analyses. In dynamical calculations, one cycle of sine wave with a frequency of 500 Hz was input on the top of the beam in terms of a normal stress to represent the exciting source. The Rayleigh damping with a ratio of 1% was utilized during dynamic calculations to represent the attenuation of materials.

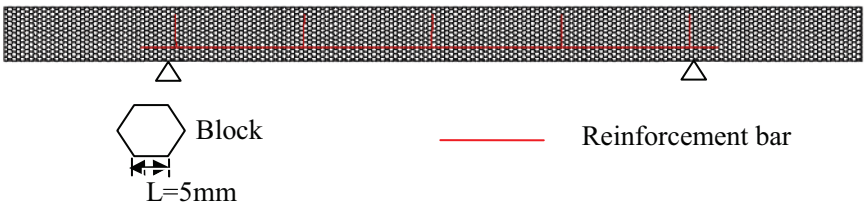

Fig. 3.9 EDEM models corresponding to the experiment.

Table 3.3 Physico-mechanical properties of the reinforcement (Hatanaka et al., 2010).

Materials	Parameters	Units	Concrete
Reinforcement	Density	kg/m^3	7500
	Elastic modulus	GPa	200
	Tensile strength	MPa	310

Table 3.4 Mechanical properties of cracks in numerical simulations.

Parameters	Units	Pre-existing crack	New crack
Shear stiffness	Gpa/m	10000	3.3
Normal stiffness	Gpa/m	10000	17.7
Cohesion	MPa	-	0.28
Friction angle	°	-	13
Tensile strength	MPa	-	0

3.4 Results of the experiment and numerical simulations

3.4.1 The relationship between loading and mid-span displacement

Fig. 3.10 represent the mid-span displacement-loading curves of the experiment and numerical simulations. In the early portion of the curve (loading < 5 kN), the displacement is proportional to the loading with a steep slope, which indicates a larger stiffness (the blue dash line) and an elastic state. As the loading is increased, the slope decreases. This nonlinearity reveals that tensile stress on the bottom of the beam exceeds the tensile strength of the concrete and cracks occur in the beam, which reduces the stiffness of the beam (the red dash line). When the loading exceeds 25 kN, the significant increment of displacement indicates the reinforcement bars yields.

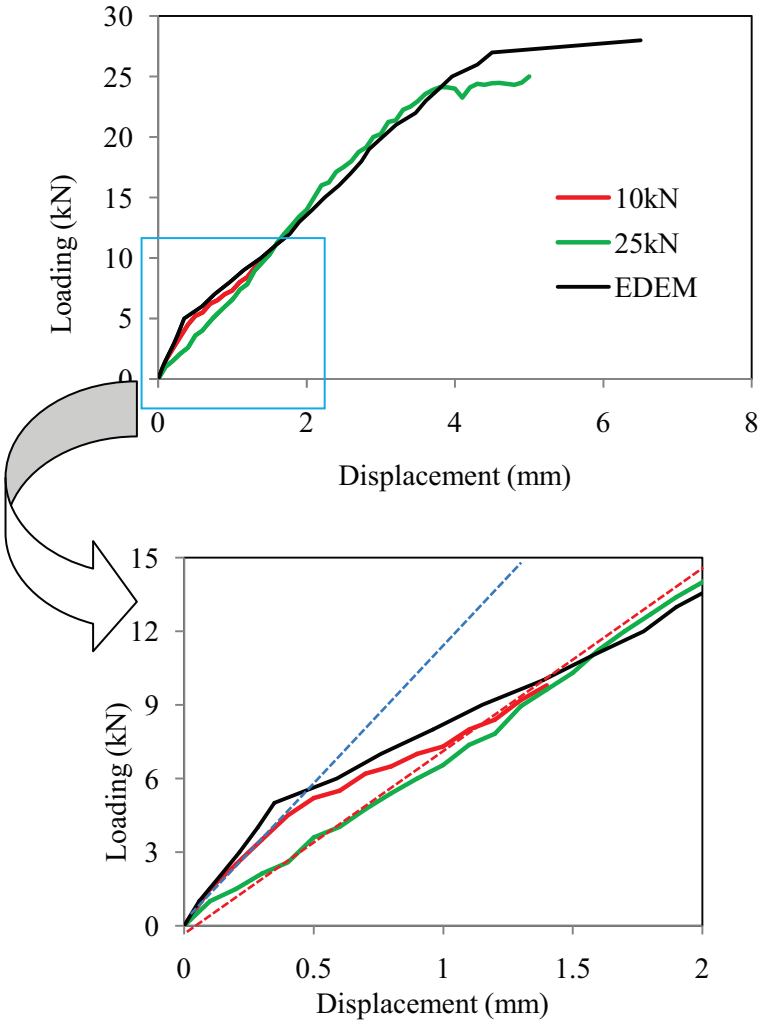

Fig. 3.10 The mid-span displacement-loading curves of the experiments.

Fig. 3.11 show the failure distributions of the beam with different loadings. When the loading = 10 kN (see Fig. 3.11a), no obvious cracks can be identified, even though the displacement-loading curves indicates cracks occur. When the loading = 20 kN, cracks are identified in the bottom (see Fig. 3.11b). With the increment of loadings, the open cracks grow from the bottom up (see Figs. 3.11cd).

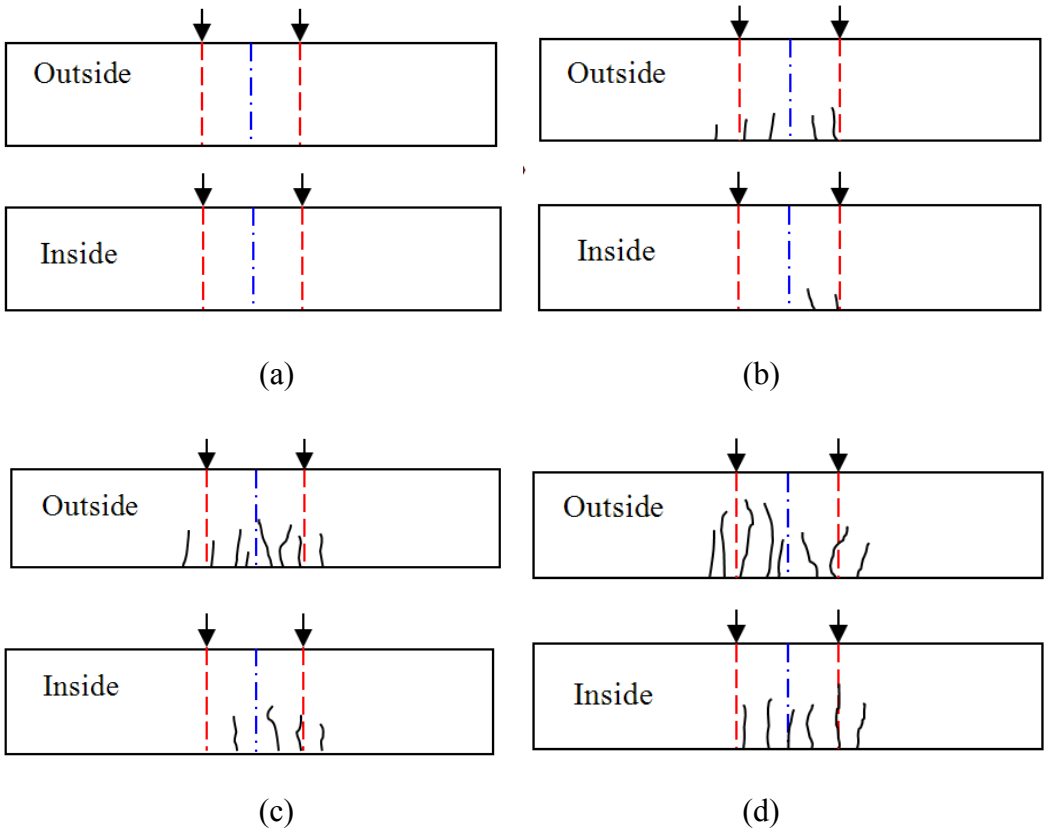

Fig. 3.11 The failure distributions of the beam. (a) 10 kN. (b) 20 kN. (c) 25 kN. (d) 30 kN.

3.4.2 The growth of cracks

The failure statuses of models obtained from the EDEM simulations is shown in Fig. 3.12. In this study, the loading is too low to induce a steel-concrete slipping (Massenzio et al., 2005).

When the loading = 6 kN, the closed cracks were generated in the bottom of the beam due to the concentrated tensile stress (see Fig. 3.12a), which reveal the reason of stiffness degradation indicated by displacement-loading curve.

With the increment of loadings, cracks grow upward and the damaged concrete expanded as shown in Fig. 3.12bcd. When these cracks penetrate three-quarters of the beam, cracks open in the bottom. While in the experiment, no cracks can be identified on the surface of the beam even loading = 10 kN. It is because the crack aperture is too small to identify by eyes or cracks only occurs inside of beam. With the initiation of cracks, the concrete is damaged around the crack resulting in a decrease of stiffness. As the loading continues to increase, these cracks stop growing, and additional cracks initiates and grows. As shown in Fig. 3.13, a sudden increase of the axial force of the longitudinal tensile reinforcement bar occurs when loading > 5 kN, indicating the reinforcement embedded in concrete carrying the most of loading increment after cracks initiate.

When the loading exceeds 25 kN, the tensile stress exceeds the tensile yield strength of the longitudinal tensile reinforcement bar, resulting in a large deflection of the beam and the failure of the beam which agrees well with the experimental phenomena (see Fig. 3.11). Meanwhile, the cracks due to shear failure also occur in the top of the beam. When the loading = 28 kN, the upper-propagating cracks due to tensile failure and the cracks due to the shear failure are connected and the beam failed finally.

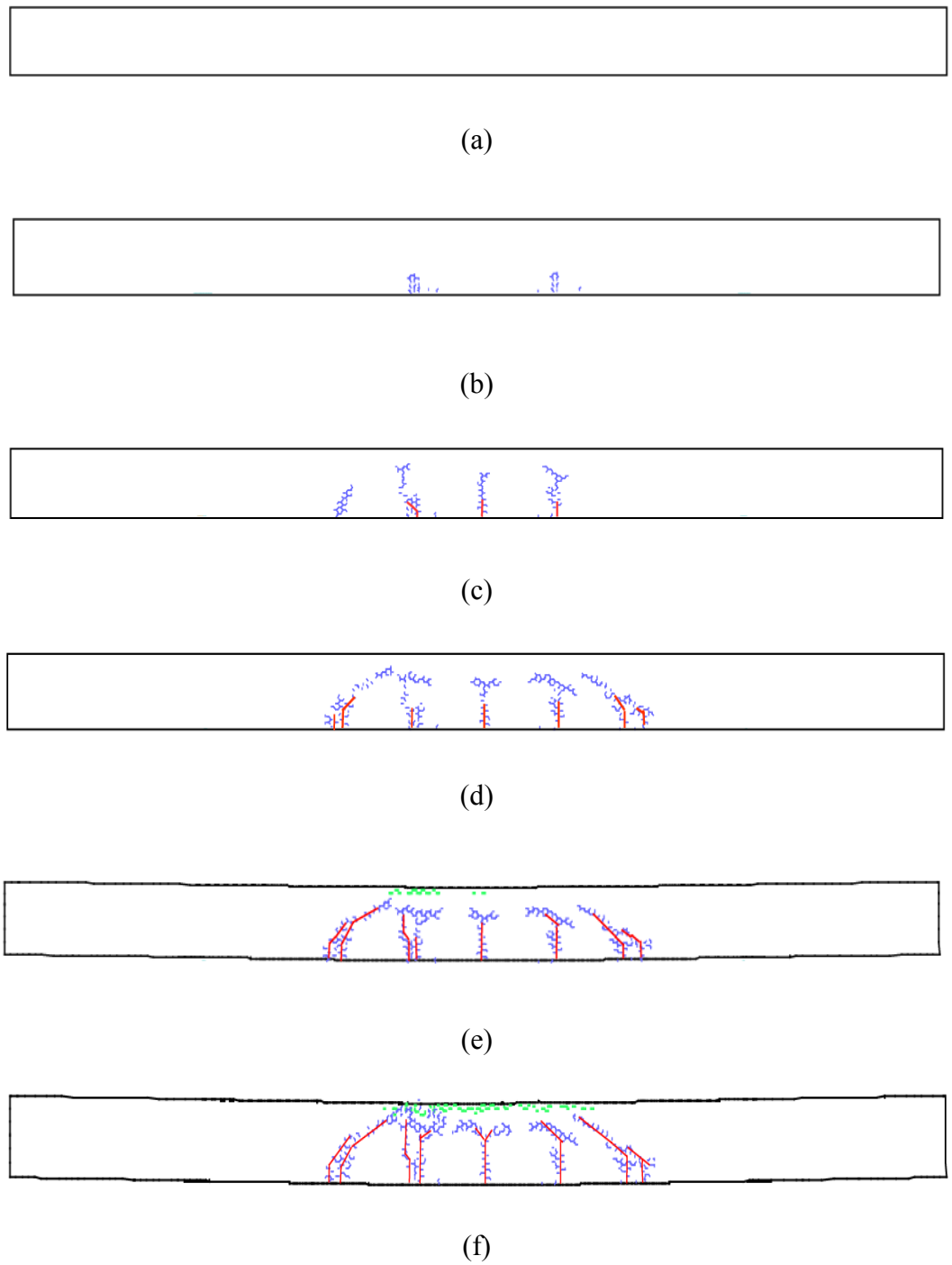

Fig. 3.12 The failure statuses of models obtained from the EDEM simulations. (a) 1 N. (b) 6 kN. (c) 10 kN. (d) 20 kN. (e) 25 kN. (f) 28 kN.

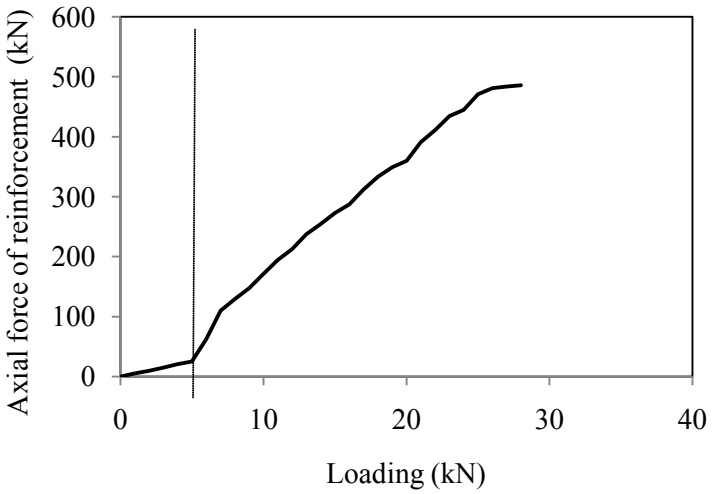

Fig. 3.13 The variation of axial force of longitudinal tensile rebar from the EDEM simulations.

3.4.2 The natural frequency analysis

A static equilibrium calculation was achieved before the start of dynamic analyses. In dynamical calculations, a short duration impulse with a frequency of 500 Hz was input on the top of beam in terms of a normal stress to represent the impulse induced by the hammer. The Rayleigh damping with a ratio of 0.7% was utilized during dynamic calculations to represent the attenuation of materials. 16384 discrete time signal data at each monitoring point were recorded during numerical simulations with a sampling interval of 0.001s. The natural frequency can be acquired by the Fast Fourier Transform (FFT). The measured natural frequencies during the experiment and numerical simulations are compared and plotted in Fig. 3.14.

The experimental and numerical results indicate four stages characteristic. In the range of 0 ~ 5 kN, due to the transverse deformation of the RC beam under loading, the natural frequency decreases slowly before the crack occurs (loading < 5 kN). In the range of 5 kN ~ 10 kN, the natural frequencies decrease rapidly. In this stage, the cracks initiate and grow, resulting obvious stiffness degradation. The descending natural frequency revels damages occur in the beam. In the range of 10 kN ~ 24 kN, the variation of frequency become gentle. It is because the reinforcement bars carry the most of loading increment and the changes of whole structure stiffness are not as obvious as the previous stage. In the range of 25 kN ~ 30 kN, the frequency decreases rapidly again due to the decrement

of beam stiffness decreases induced by the yielding of longitudinal tensile reinforcement. Before loading, the natural frequency difference of the beam in experiment and simulation are small, while the difference increases with the increment of loading especially after cracks occurring. It is induced by the differences between the 3D experimental beam and 2D numerical model. In the experiment, due to the inhomogeneity of the RC beam, cracks could initiates in the local region without penetrating the beam in the width direction, as shown in Fig. 3.8b. While in 2D numerical model the generated cracks distribute through the beam in the width direction, which can reduce the natural frequency obviously.

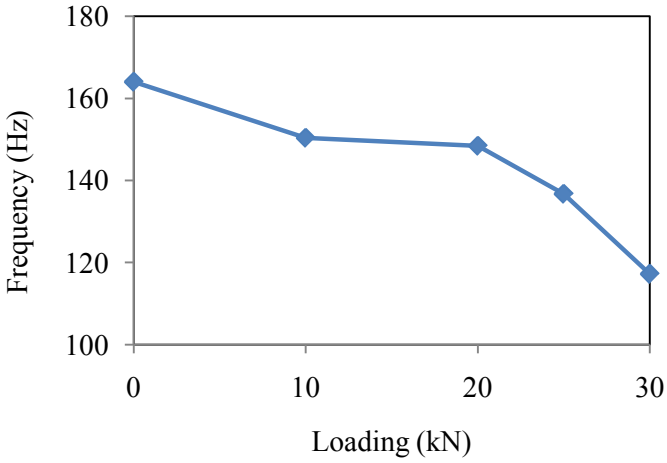

(a)

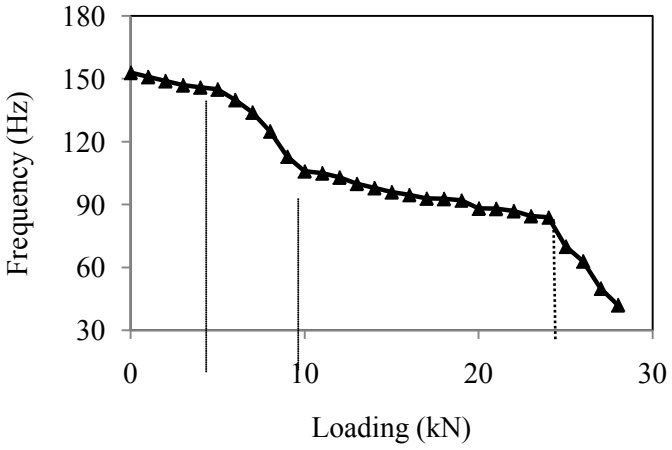

(b)

Fig. 3.14 The measured natural frequencies of both the experiment and numerical simulations. (a) The experiment. (b) The numerical simulations.

3.5 Summary

In this chapter, the EDEM based on the tensile-shear failure criterion was used to investigate the failure behavior and natural frequency of RC beam in the loading test. Numerical simulations were carried out based on the EDEM models to compare with the experiment. The displacement-loading curve and the failure status of the EDEM simulations agree well with the experimental tests. In both EDEM simulations and the experiments, similar variation of natural frequency can also be concluded that: the cracking process in the RC beam, that decreases its stiffness, can be identified based on the continuously descending of the natural frequency.

Additionally, the EDEM can serve as an effective and low-cost approach to investigate the mechanical parameters of fractured rock masses or rock-like materials, such as the cohesion and the internal friction angle.

CHAPTER 4

A two-dimensional vibration model for mountain tunnel lining built with poling-board method

4.1 Introduction

A mountain tunnel lining can be treated as a cylindrical shell structure of which the thickness is much smaller than other dimensions. Meanwhile, the vibration amplitude of the tunnel lining mainly caused by traffic is fairly small, usually ranging from hundreds of mgals to several gals. Hence, the thin shell theory can be adopted for the analysis of tunnel lining vibration. The vibration of thin elastic shells has been studied by many researchers and numerous different shell theories have been derived in the literature (Leissa 1973; Soedel 1981; Cremer, Heckl and Ungar 1988). The different shell theories represent a simplification of the three-dimensional theory of linear elasticity.

In this chapter, both the Love-Timoshenko shell theory and Donnell-Mushtari shell theory are adopted and are extended to the elastic boundary conditions to analyze the vibration characters of tunnel lining built with poling-board method. The rock-concrete contacts between rock mass and concrete lining, is considered as elastic boundaries which can be represented by the distributed springs between the rock and the tunnel shell lining. The voids, which usually exist between concrete linings and rock masses and can be considered as the additional distribution load which is equivalent in magnitude to the elastic boundary load but opposite in direction acting on the outer surface. The influence of the additional load on the natural frequencies can be estimated by the modal expansion approach. It is found that the stiffness of elastic supports has significant effect on the natural frequency of the lining. This stiffness can also be estimated by nature frequencies of tunnel lining. Numerical results are compared with analytical solutions proposed in this chapter. The nature frequencies estimated by Love-Timoshenko shell theory and Donnell-Mushtari shell agree well with the numerical results. The first order frequency of the tunnel lining with a void is influenced significantly by the void size and can also be estimated exactly by the proposed approach.

4.2 Theoretical formulation

4.2.1 Love-Timoshenko shell theory

The basic theoretical approach is due to Love (1888), who published the equations in their essential form toward the end of the 19th century. The material is considered to be linearly elastic, isotropic and homogeneous. In the classical theory of thin shells, the following assumptions were made by Love:

- The thickness of the shell is small compared with the other dimensions.
- Displacements are assumed to be small to yield linear equations.
- Normals to the undeformed middle surface remain straight and normal to the deformed middle surface and suffer no extension.
- Shear deformation and rotary inertia effects are neglected.

The geometry and the coordinate system for the circular cylindrical shell are shown in Fig. 4.1. R is the radius of curvature of the middle surface of the shell, h is the shell's thickness, x, r and e are the cylindrical coordinates and u, v and w the orthogonal components of displacement of the shell.

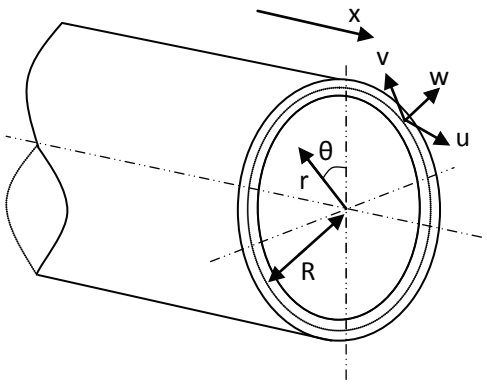

Fig. 4.1 Geometry and cylindrical coordinate system.

By Kirchhoff' theory (1850), the displacement varies linearly through the shell thickness:

$$u^* = u - (r - R)\frac{\partial w}{\partial x} \qquad (4.1a)$$

$$v^* = v - \frac{r - R}{R}\left(\frac{\partial w}{\partial \theta} - v\right) \qquad (4.1b)$$

$$w^* = w \qquad (4.1c)$$

where the subscript '*' refers to the non-neutral surface of the shell.

The strain-displacement equations for thin shell are shown in a form where membrane strains (independent of (*r*-*R*) and bending strains) and bending strains (proportional to (*r*-*R*)) are separated:

$$\varepsilon^*_x = \varepsilon + (r-R)k_x \quad (4.2a)$$

$$\varepsilon^*_x = \varepsilon + (r-R)k_x \quad (4.2b)$$

$$\gamma^*_{x\theta} = \gamma_{x\theta} + (r-R)k_{x\theta} \quad (4.2c)$$

where the membrane strains are

$$\varepsilon_x = \frac{\partial u}{\partial x} \quad (4.3a)$$

$$\varepsilon_\theta = \frac{1}{R}\frac{\partial v}{\partial \theta} + \frac{w}{R} \quad (4.3b)$$

$$\varepsilon_{x\theta} = \frac{\partial v}{\partial x} + \frac{1}{R}\frac{\partial u}{\partial \theta} \quad (4.3c)$$

and where the change-in-curvature terms (bending strains) are

$$k_x = \frac{\partial \beta_x}{\partial x} \quad (4.4a)$$

$$k_\theta = \frac{1}{R}\frac{\partial \beta_\theta}{\partial \theta} \quad (4.4b)$$

$$k_{x\theta} = \frac{\partial \beta_\theta}{\partial x} + \frac{1}{R}\frac{\partial \beta_x}{\partial \theta} \quad (4.4c)$$

where β_x and β_θ become

$$\beta_x = -\frac{\partial w}{\partial x} \quad (4.5a)$$

$$\beta_\theta = \frac{v}{R} - \frac{1}{R}\frac{\partial w}{\partial \theta} \quad (4.5b)$$

The normal stress, which acts in the normal direction to the neutral surface, is much smaller than that in other directions and can be neglected: $\sigma_r = 0$. The stress-strain equations are:

$$\sigma_x = \frac{E}{1-\mu^2}\left(\varepsilon^*_x + \mu\varepsilon^*_\theta\right) \quad (4.6a)$$

$$\sigma_\theta = \frac{E}{1-\mu^2}\left(\varepsilon^*{}_\theta + \mu\varepsilon^*{}_x\right) \quad (4.6b)$$

$$\tau_{x\theta} = \frac{E}{2(1+\mu)}\gamma^*{}_{x\theta} \quad (4.6c)$$

where E is Young's modulus of elasticity and μ is Poisson's ratio. Substituting Eqs. (4.2) gives

$$\sigma_x = \frac{E}{1-\mu^2}\left(\varepsilon_x + \mu\varepsilon_\theta + (r-R)(k_x + \mu k_\theta)\right) \quad (4.7a)$$

$$\sigma_x = \frac{E}{1-\mu^2}\left(\varepsilon_\theta + \mu\varepsilon_x + (r-R)(k_\theta + \mu k_x)\right) \quad (4.7b)$$

$$\sigma_{x\theta} = G\left(\varepsilon_{x\theta} + k_{x\theta}(r-R)\right) \quad (4.7c)$$

where G is the shear modulus. Thus, the relationships between the force per unit length of neutral surface and strain of neutral surface can be calculated as:

$$N_x = K(\varepsilon_x + \mu\varepsilon_\theta) \quad (4.8a)$$

$$N_\theta = K(\varepsilon_\theta + \mu\varepsilon_x) \quad (4.8b)$$

$$N_{x\theta} = N_{\theta x} = \frac{K(1-\mu)}{2}\varepsilon_{x\theta} \quad (4.8c)$$

$$M_x = D(k_x + \mu k_\theta) \quad (4.8d)$$

$$M_\theta = D(k_\theta + \mu k_x) \quad (4.8e)$$

$$M_{x\theta} = \frac{D(1-\mu)}{2}k_{x\theta} \quad (4.8f)$$

where $K = E\,h\,/\,(1-\mu^2)$ and $D = E\,h^3\,/12\,/\,(1-\mu^2)$.

Although the strains in radial direction vanish by assumption, the corresponding forces and moments N_x, N_θ, $N_{x\theta}$, M_x, M_θ and $M_{x\theta}$ cannot be neglected. The equations of motion for per unit length of circular cylindrical shell are:

$$\frac{\partial N_x}{\partial x} + \frac{1}{R}\frac{\partial N_{\theta x}}{\partial \theta} = \rho h\frac{\partial^2 u}{\partial t^2} \quad (4.9a)$$

$$\frac{\partial N_{x\theta}}{\partial x}+\frac{1}{R}\frac{\partial N_{\theta}}{\partial \theta}+\frac{Q_{\theta}}{R}=\rho h\frac{\partial^2 v}{\partial t^2} \quad (4.9b)$$

$$\frac{\partial Q_{x}}{\partial x}+\frac{1}{R}\frac{\partial Q_{\theta}}{\partial \theta}-\frac{N_{\theta}}{R}=\rho h\frac{\partial^2 w}{\partial t^2} \quad (4.9c)$$

$$Q_x=\frac{\partial M_x}{\partial x}+\frac{1}{R}\frac{\partial M_{\theta x}}{\partial \theta} \quad (4.9d)$$

$$Q_{\theta}=\frac{\partial M_{x\theta}}{\partial x}+\frac{1}{R}\frac{\partial M_{\theta}}{\partial \theta} \quad (4.9e)$$

The volume forces, like gravity stress, and the damping have been neglected. Substituting Eqs. (4.3) - (4.5) and (4.8), the equation of neutral surface in differential form can be written as

$$\frac{\partial^2 u}{\partial x}+\frac{(1-\mu)}{2}\frac{\partial^2 u}{R^2\partial\theta^2}+\frac{1+\mu}{2}\frac{\partial^2 v}{R\partial x\partial\theta}+\mu\frac{\partial w}{R\partial x}=\frac{1}{K}(\rho h\frac{\partial^2 u}{\partial t^2}) \quad (4.10a)$$

$$\frac{1+\mu}{2}\frac{\partial^2 u}{R\partial x\partial\theta}+\frac{(1-\mu)}{2}\frac{\partial^2 v}{\partial x^2}+\frac{\partial^2 v}{R^2\partial\theta^2}+\frac{\partial w}{R^2\partial\theta}+ \quad (4.10b)$$
$$b\left[\frac{(1-\mu)}{2}\frac{\partial^2 v}{\partial x^2}+\frac{\partial^2 v}{R^2\partial\theta^2}-\frac{\partial^3 w}{\partial x^2\partial\theta}-\frac{\partial^3 w}{R^2\partial\theta^3}\right]=\frac{1}{K}(\rho h\frac{\partial^2 v}{\partial t^2})$$

$$\frac{12}{h^2}\left\{\mu\frac{\partial u}{R\partial x}+\frac{\partial^2 v}{R^2\partial\theta^2}+\frac{w}{R^2}-b\left[\frac{\partial^3 v}{\partial x^2\partial\theta}+\frac{\partial^3 v}{R^2\partial\theta^3}\right]\right\}+\nabla^2\nabla^2 w \quad (4.10c)$$
$$=\frac{1}{D}(-\rho h\frac{\partial^2 w}{\partial t^2})$$

where

$$\nabla^2=\frac{\partial^2}{\partial x^2}+\frac{\partial^2}{R^2\partial\theta^2} \quad (4.11a)$$

$$b=\frac{h^2}{12R^2} \quad (4.11b)$$

As the length of mountain tunnel is much larger than its cross section, transverse and circumferential modes in cross section are easier to excite and are much larger than that of axial mode. That is to say, the deformations mainly exist in cross section. Meanwhile, there are similar boundary conditions along the axial direction. Therefore, the mountain tunnel can be simplified as a plane strain model of the cylindrical shell with infinite length.

The physical quantities (displacements, membrane force, etc) do not depend upon location along the length. The displacement functions illustrated in Fig. 1 can be represented as follows

$$u \equiv 0 \tag{4.12a}$$

$$v = v(\theta) \tag{4.12b}$$

$$w = w(\theta) \tag{4.12c}$$

Substituting Eqs. (4.12) in Eqs. (4.10), the equations governing the vibrations in a plane strain model become

$$\frac{\partial^2 v}{\partial \theta^2} + \frac{\partial w}{\partial \theta} + b\left(\frac{\partial^2 v}{\partial \theta^2} - \frac{\partial^3 w}{\partial \theta^3}\right) = \frac{R^2}{K}\left(\rho h \frac{\partial^2 v}{\partial t^2}\right) \tag{4.13a}$$

$$\frac{\partial v}{\partial \theta} + w - b\left(\frac{\partial^3 v}{\partial \theta^3} - \frac{\partial^4 w}{\partial \theta^4}\right) = \frac{R^2}{K}\left(-\rho h \frac{\partial^2 w}{\partial t^2}\right) \tag{4.13b}$$

In the old tunnels that were built with the poling-board method, the poling-board was used instead of shotcrete so that incomplete contacts usually exist between rock mass and poling-boards, as shown in Fig. 4.2. The unbounded contacts and poling-board can be simplified to weak concrete-rock interfaces which can be represented by the distributed springs with small magnitudes of normal stiffness *kn* and shear stiffness *ks*. The elastic foundation boundary included in Love's shell theory through the additional load terms q_r and q_θ is refined as (neglecting damping effects):

$$q_\theta = -k_s v \tag{4.14a}$$

$$q_r = -k_n v \tag{4.14b}$$

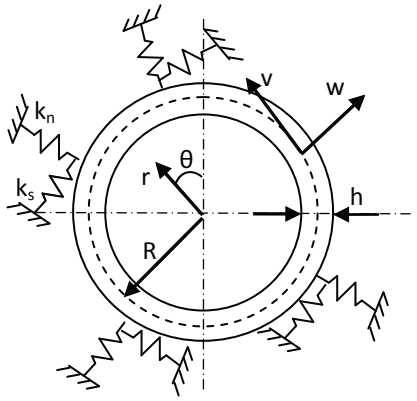

Fig. 4.2 The schematic diagram of a circular cylindrical shell.

Eqs. (4.13) therefore becomes

$$\frac{\partial^2 v}{\partial\theta^2}+\frac{\partial w}{\partial\theta}+b\left(\frac{\partial^2 v}{\partial\theta^2}-\frac{\partial^3 w}{\partial\theta^3}\right)-\frac{R^2 k_s v}{K}=\frac{R^2}{K}\left(\rho h\frac{\partial^2 v}{\partial t^2}\right) \tag{4.15a}$$

$$\frac{\partial v}{\partial\theta}+w-b\left(\frac{\partial^3 v}{\partial\theta^3}-\frac{\partial^4 w}{\partial\theta^4}\right)+\frac{R^2}{K}k_n w=\frac{R^2}{K}\left(-\rho h\frac{\partial^2 w}{\partial t^2}\right) \tag{4.15b}$$

It is possible to approach the solution using the Laplace transformation. However, in certain, it is possible to take a shortcut. Special displacements functions can be chosen for the plane strain model of the cylindrical shell with infinite length

$$v=Ve^{j\omega t}=B\sin n\theta e^{j\omega t} \qquad (n=0,1,2,\ldots) \tag{4.16a}$$

$$w=We^{j\omega t}=C\cos n\theta e^{j\omega t} \tag{4.16b}$$

where B and C are the amplitudes of the displacements in r and θ directions. Substituting the displacements corresponding v and w into Substituting the displacements corresponding v and w in to Eqs. (4.15) gives

$$\frac{\partial^2 V}{\partial\theta^2}+\frac{\partial W}{\partial\theta}+b\left(\frac{\partial^2 V}{\partial\theta^2}-\frac{\partial^3 W}{\partial\theta^3}\right)-\frac{R^2}{K}k_s V+\frac{\rho h R^2}{K}\omega^2 V=0 \tag{4.17a}$$

$$\frac{\partial V}{\partial\theta}+W-b\left(\frac{\partial^3 V}{\partial\theta^3}-\frac{\partial^4 W}{\partial\theta^4}\right)+\frac{R^2}{K}k_n W-\frac{R^2\rho h}{K}\omega^2 W=0 \tag{4.17b}$$

Substitute Eqs. 4.16 in Eqs. 4.17

$$\left(n^2+bn^2+\frac{R^2}{K}k_s-\Omega^2\right)B+\left(n+bn^3\right)C=0 \tag{4.18a}$$

$$\left(n+bn^3\right)B+\left(1+bn^4+\frac{R^2}{K}k_n-\Omega^2\right)C=0 \tag{4.18b}$$

where

$$\Omega^2=\frac{\rho hR^2}{K}\omega^2 \tag{4.19a}$$

This system of equations can be written in matrix form and the determinant of the matrix is zero for non-trivial solutions as follows:

$$\begin{vmatrix} n^2+bn^2+\frac{R^2}{K}k_s-\Omega^2 & n+bn^3 \\ n+bn^3 & 1+bn^4+\frac{R^2}{K}k_n-\Omega^2 \end{vmatrix}=0 \tag{4.20a}$$

The frequency factor can be calculated as:

$$\Omega^2=1+\frac{R^2}{K}k_n \qquad \text{(n=0)} \tag{4.21a}$$

$$\Omega^2=\frac{1}{2}\left[1+\frac{R^2}{K}k_n+\frac{R^2}{K}k_s+n^2\left(1+b\right)+bn^4\right] \pm\frac{1}{2}\sqrt{\left[1+\frac{R^2}{K}k_n+\frac{R^2}{K}k_s+n^2\left(1+b\right)+bn^4\right]^2 +4n^2\left(1+bn^2\right)^2-4\left(n^2+bn^2+\frac{R^2}{K}k_s\right)\left(1+bn^4+\frac{R^2}{K}k_n\right)} \tag{4.21b}$$

(n≠0)

4.2.2 Simplified shell theory: Donnell–Mushtari Equations

Except for a few special cases, explicit solutions are not available for Love's equations. Many approximate solution approaches were proposed to overcome this limit. Of all the simplifications presented, that of by Donnell and Mushtari have been used most widely in shell vibrations (Soedel, 1981). It neglects neither bending nor membrane effects.

The first basic assumption of Donnell–Mushtari theory is that the tangential displacements and their derivatives in bending strain expressions Eqs. (4.4) but not in the membrane strain expressions. Therefore, the bending strains are

$$k_x = \frac{\partial \beta_x}{\partial x} = -\frac{\partial^2 w}{\partial x^2} \tag{4.22a}$$

$$k_\theta = \frac{1}{R}\frac{\partial \beta_\theta}{\partial \theta} = -\frac{1}{R^2}\frac{\partial^2 w}{\partial \theta^2} \tag{4.22b}$$

$$k_{x\theta} = \frac{\partial \beta_\theta}{\partial x} + \frac{1}{R}\frac{\partial \beta_x}{\partial \theta} = -\frac{2}{R}\frac{\partial^2 w}{\partial x \partial \theta} \tag{4.22c}$$

The second assumption is that the influences of inertia $\rho h\partial^2 u/\partial t^2$ & $\rho h\partial^2 v/\partial t^2$ and shear force Q_θ/R are neglected. The equations of motion are

$$\frac{\partial N_x}{\partial x} + \frac{1}{R}\frac{\partial N_{\theta x}}{\partial \theta} = \rho h \frac{\partial^2 u}{\partial t^2} \tag{4.23a}$$

$$\frac{\partial N_{x\theta}}{\partial x} + \frac{1}{R}\frac{\partial N_\theta}{\partial \theta} = \rho h \frac{\partial^2 v}{\partial t^2} \tag{4.23b}$$

$$-D\nabla^4 w - \frac{N_\theta}{R} = \rho h \frac{\partial^2 w}{\partial t^2} \tag{4.23c}$$

Considering the weak concrete-rock interfaces, the Eqs. (4.15) governing the vibrations in a plane strain model become

$$\frac{\partial^2 v}{\partial \theta^2} + \frac{\partial w}{\partial \theta} - \frac{R^2 k_s v}{K} = \frac{R^2}{K}\left(\rho h \frac{\partial^2 v}{\partial t^2}\right) \tag{4.24a}$$

$$\frac{\partial v}{\partial \theta} + w + b\frac{\partial^4 w}{\partial \theta^4} + \frac{R^2 k_n w}{K} = \frac{R^2}{K}\left(-\rho h \frac{\partial^2 w}{\partial t^2}\right) \tag{4.24b}$$

Proceeding similarly with the calculation from Eqs. (4.15) to (4.21), the frequency factor can be obtained:

$$\Omega^2 = 1 + \frac{R^2}{K}k_n \qquad (n=0) \tag{4.25a}$$

$$\Omega^2 = \frac{1}{2}\left[1 + \frac{R^2}{K}k_n + \frac{R^2}{K}k_s + n^2 + bn^4\right] \pm \frac{1}{2}\sqrt{\left[1 + \frac{R^2}{K}k_n + \frac{R^2}{K}k_s + n^2 + bn^4\right]^2 + 4n^2 - 4\left(n^2 + \frac{R^2}{K}k_s\right)\left(1 + b^4 + \frac{R^2}{K}nk_n\right)} \qquad (n\neq 0) \tag{4.25b}$$

4.2.3 The natural frequency influenced by the void

Voids, usually existing between concrete linings and rock masses (Fig. 4.3), are unfavorable to the supporting system and may invoke lining structure failures, such as water leakage, reinforcement corrosion and cracking. The voids can induce increased deformation and stresses in the close vicinities, which are one of the main sources that cause serious damages on tunnel linings. Meanwhile, the existence of the void changes the elastic foundation boundary into the free boundary on the outer surface of tunnel lining. At here, outer surface stands for the surface of lining closer to the void. The void can be considered as the additional distribution load which is equivalent in magnitude to the elastic boundary load but opposite in direction acting on the outer surface.

$$q_{v\theta} = k_s v \tag{4.26a}$$

$$q_{vr} = k_n w \tag{4.26b}$$

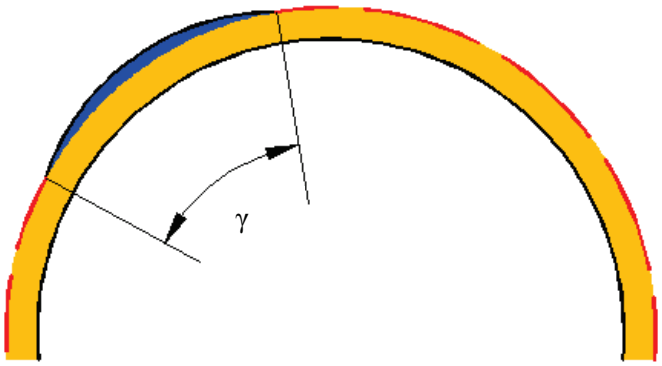

Fig. 4.3 Schematic view of a void at rock-concrete interface. Void arc length: sector angle γ.

The motion equations can be rewritten as

$$\frac{K}{R^2}\frac{\partial^2 v}{\partial \theta^2} + \frac{K}{R^2}\frac{\partial w}{\partial \theta} - k_s v - \rho h \frac{\partial^2 v}{\partial t^2} = -k_s v \delta(\theta) \tag{4.27a}$$

$$-\frac{K}{R^2}\frac{\partial v}{\partial \theta} - \frac{K}{R^2} w - b\frac{K}{R^2}\frac{\partial^4 w}{\partial \theta^4} - k_n w - \rho h \frac{\partial^2 w}{\partial t^2} = -k_n w \delta(\theta) \tag{4.27b}$$

where $\delta(\theta) = \begin{cases} 1 & -\gamma/2 \le \theta \le \gamma/2 \\ 0 & else \end{cases}$

As the natural frequency have been analyzed in Section 2.1, the influence of the additional load on the frequencies can be estimated by the modal expansion approach introduced by Soedel (1981). The displacement of continuous systems can be written in an infinites series as:

$$v(\theta,t)=\sum_{n=1}^{\infty}\eta_n(t)V_n \tag{4.28a}$$

$$w(\theta,t)=\sum_{n=1}^{\infty}\eta_n(t)W_n \tag{4.28b}$$

where η_n is the modal participation factor. The lining shell section where the void exists can be regarded as a slightly curved plated, of which vibration modes are associated primarily with transverse motion. Therefore, only the vibration in the radial direction is considered. Substituting in Eq. (4.27b) gives

$$\sum_{n=1}^{\infty}\left[\left(\frac{K}{R^2}\frac{\partial V_n}{\partial\theta}+\frac{K}{R^2}W_n+b\frac{K}{R^2}\frac{\partial^4 W_n}{\partial\theta^4}+k_nW_n\right)\eta_n+\rho h\ddot{\eta}_nW_n\right]=\sum_{n=1}^{\infty}k_n\delta(\theta)\eta_nW_n \tag{4.29}$$

Based on the eigenvalue analysis, it has been know that

$$\frac{K}{R^2}\frac{\partial V_n}{\partial\theta}+\frac{K}{R^2}W_n+b\frac{K}{R^2}\frac{\partial^4 W_n}{\partial\theta^4}+k_nW_n=\rho h\omega_n{}^2W_n \tag{4.30}$$

where ω_n is the natural frequency of tunnel lining without voids. Substituting this in Eq. (4.29) gives

$$\sum_{n=1}^{\infty}\left(\rho h\omega_n{}^2\eta_n+\rho h\ddot{\eta}_n\right)W_n=\sum_{n=1}^{\infty}k_n\delta(\theta)\eta_nW_n \tag{4.31}$$

Since the vibration modes W_n are orthogonal, Eq. (4.31) can be written by multiplying with a mode W_p where p is either equal to n or not equal:

$$\left(\rho h\omega_n{}^2\eta_n+\rho h\ddot{\eta}_n\right)W_n^2=k_n\delta(\theta)\eta_nW_n{}^2 \tag{4.32}$$

Integrating over the lining shell and substituting Eq. (4.16b) gives

$$\ddot{\eta}_n+\omega_n{}^2\eta_n=\frac{\eta_n}{\rho hN_n}\int_{-\theta_1}^{\theta_1}k_n\cos^2 n\theta Rd\theta \tag{4.33}$$

where $N_n=\int_0^{2\pi}\cos^2 n\theta Rd\theta$.

Therefore, the natural frequencies ω_{vn} , which are affected by the void, can be calculated as

$$\omega_{vn} = \sqrt{\omega_n^2 - \frac{1}{\rho h N_n}\int_{-\gamma/2}^{\gamma/2} k_n \cos^2 n\theta R d\theta} \qquad (4.34)$$

4.3 Numerical simulations and discussions

4.3.1Numerical simulations of tunnel vibrations

To verify the analytical methods discussed above, numerical simulations were performed by using the Distinct Element Method (DEM) code of UDEC to investigate the nature frequency of tunnel lining.

In numerical simulations, the unbonded contact and the poling-board can be represented by the interface element with low normal and shear stiffness, which are treated as discontinuities between distinct bodies (i.e., the discontinuity is treated as an inner boundary in the DEM) (UDEC 2000). The Mohr-Coulomb model and Coulomb slip model were adopted to represent the mechanical behavior of rock masses and interfaces, respectively. Those types of elements can effectively simulate the dynamic deformational behavior of rock masses, lining concretes and interfaces. The shape and size of the numerical model are shown in Fig. 4.4. The physic-mechanical properties of the surrounding rock mass, lining concrete and concrete-rock interfaces are listed in Table 4.1, which are determined according to the properties of rock mass and concrete lining of a tunnel in Japan (Gao et al. 2014). The physico-mechanical properties of the rock samples used in simulation were obtained from the unconfined and triaxial compression tests.

In dynamic calculations, a stationary Gaussian white noise with a frequency range from 0 to 100Hz was input on the floor of tunnel to represent the exciting source (e.g., passing vehicles). The element size was set to be 0.2 m in order to simulate the propagation of stress waves accurately. The damping ratio was set to 0 during dynamic calculations. The boundaries of model were set as viscous boundaries to minimize wave reflections at boundaries. The vibration histories of the lining surface in both the horizontal direction

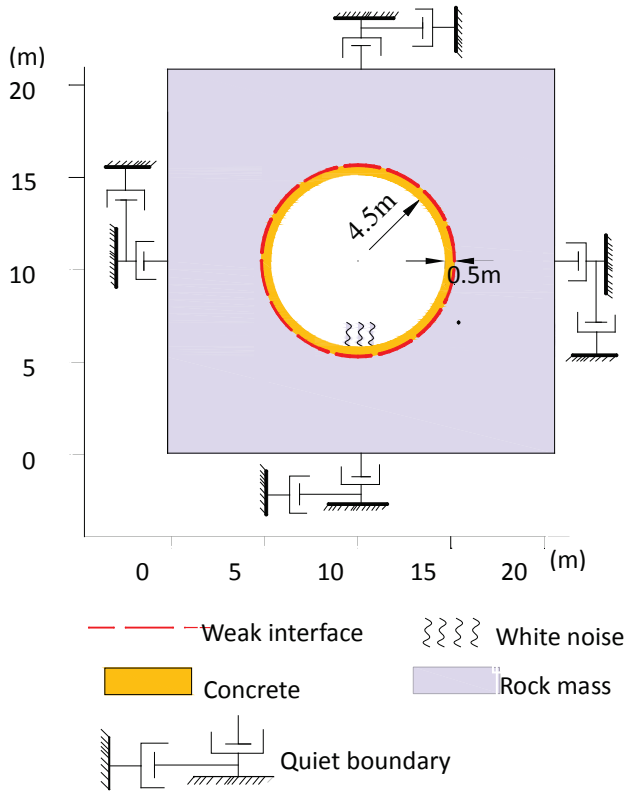

Fig. 4.4 Model of numerical simulation.

Table 4.1. Material properties used in the numerical simulations (Gao et al. 2014).

Parameters		Units	Values
Intact rock	Density	kg/m^3	2550
	Elastic modulus	GPa	30
	Poisson's ratio	-	0.22
Concrete	Density	kg/m^3	2500
	Elastic modulus	GPa	22
	Poisson's ratio	-	0.28
Interface	Normal stiffness	MPa/m	200
	Shear stiffness	MPa/m	20

and the vertical direction were recorded to obtain the nature frequencies. 32768 discrete time signal data at the monitoring point were recorded during numerical simulations with a sampling interval of 0.001s.

The 'spectrum peak-picking method', which was widely used in spectrum analyses, was adopted for the peak frequency identification in data analyses. The Power Spectrum Density (PSD) P(f), is given by

$$P(f) = \frac{1}{T}\left|X(f)\right|^2 \qquad (4.35)$$

where f is the frequency, T is the time and X(f) is the frequency spectrum. The PSD of measured microtremor was calculated to acquire the peak frequency, by using the Welch's averaged periodogram method implanted in MATLAB (MATLAB 2003). In the Welch's method , the PSD $P_{Welch}(f)$ can be calculated as (Welch, 1967):

$$P_{Welch}(f) = \frac{1}{F_s LU}\int_{-F_s/2}^{F_s/2}\left|W(f-f')\right|^2 P(f')df' \qquad (4.36)$$

where P(f) is the PSD estimated by the discrete-time Fourier transform, F_s is the sampling frequency, L is the length of the data segments and U is the same normalization constant present in the definition of the modified periodogram and W(f) is the Fourier transform of the window function.

A hamming window with a length of 2048 and 50% data overlapping was adopted to smooth the curve and to reduce the leakage error. The spectrum resolution is 0.488Hz. The PSD amplitudes were normalized by using the sum of the squares of the PSD corresponding to each frequency, as given by

$$NPSD(f) = P(f)\Big/\sqrt{\sum_{k=1}^{m} P(f)^2} \qquad (4.37)$$

where *P(f)* is the Power Spectrum Density (PSD), *NPSD(f)* is the normalized PSD corresponding to the frequency *f* and *k* is the number of frequency points.

The average of all normalized PSD at an individual monitoring point was calculated and a so-called ANPSD spectrum was obtained:

$$ANPSD(\omega_k) = \frac{1}{n}\sum_{i=1}^{n} NPSD_i(\omega_k) \qquad (4.38)$$

where $NPSD_i(\omega_k)$ is the normalized PSD for the frequency ω_k at the monitoring point *i*.. One typical example was shown in Fig. 4.5, and the corresponding mode shapes were plotted in Fig. 4.6. The nature frequencies can be identified by the peak-picking method, even though the frequency peak around 46.31 Hz are not as obvious as others. The nature frequencies were analyzed and compared to the results of Eqs. (4.21) and (4.25) as shown in Fig. 4.7, and the first four modes were listed in Table 4.2. Two sets of natural frequencies can be indentified in analytical solutions. Due to the limitation of accelerometer, only the frequencies below 100 Hz were discussed here. A relative error parameter in Table 4.2 is defined as following:

$$Error = \frac{f_{theory} - f_{DEM}}{f_{DEM}} \times 100\% \qquad (4.39)$$

The errors of the frequencies are very small (less than 3%), therefore, these results are considered to be reliable and accurate.

In Fig.4.7, two nonzero sets of natural frequencies can be confirmed. Low-order natural frequencies, which can be excited easily, are widely adopted in modal analysis for the damage identification. In this study, the natural frequencies bellow 100Hz was analyzed primarily due to the accuracy limitations of measurements. The nature frequencies estimated by the Donnell theory is slightly larger than that of Love theory due to the neglecting of the tangential displacements and their derivatives.

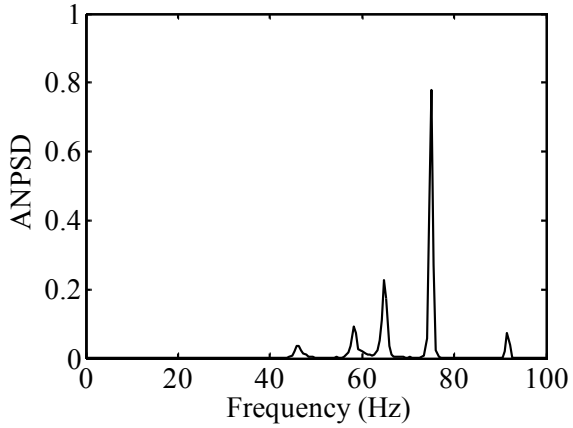

Fig. 4.5 The normalized power spectrum of vibration on the surface of tunnel lining

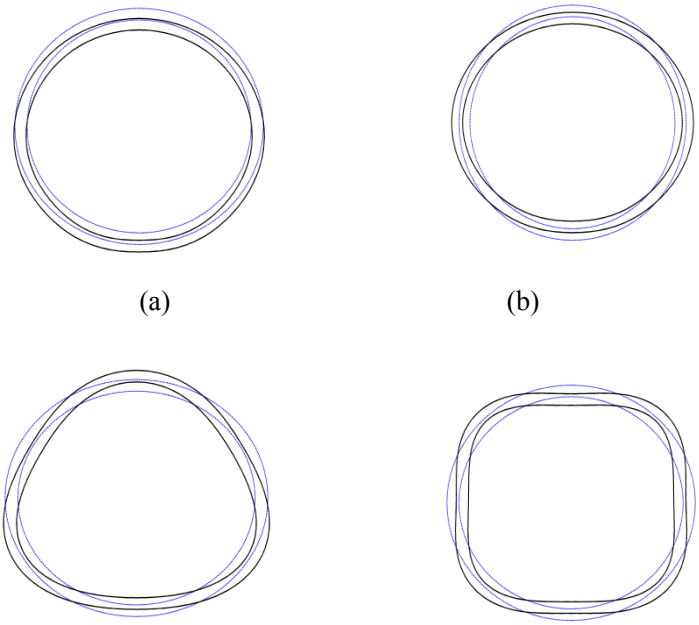

Fig. 4.6 Calculated mode shapes. (a) 46.31 Hz. (b) 58.25 Hz. (c) 64.93 Hz. (d) 74.96 Hz.

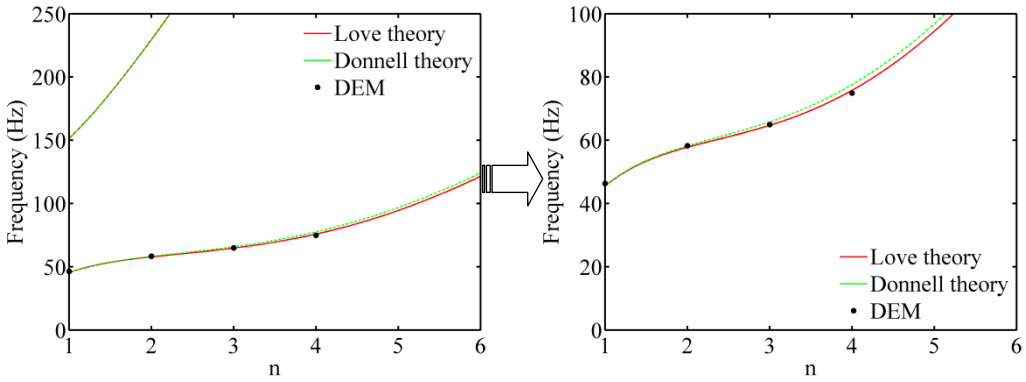

Fig. 4.7 The natural frequencies of analytical solution and DEM simulation.

Table 4. 2. Comparison of natural frequencies.

n	DEM (Hz)	Love theory (Hz)	Error (%)	Donnell theory (Hz)	Error (%)
1	46.31	45.48	2	45.52	2
2	58.25	57.79	1	58.25	0
3	64.93	64.73	0	65.83	1
4	74.96	75.80	1	77.59	3

In the thin shell theory, the transverse shear deformation in shell-bending behavior is ignored. As the thickness-to-radius ratio increases, the shear deformation trends to be significant. The influence of h/R on the nature frequency error was plotted in Fig. 4.8. The relative error of each vibration mode increases with the increment of h/R except at $n = 1$. For $n \leq 2$, the error is relatively small in all cases (below 3%), which indicates that h/R has few influences on low frequency modes. For $n = 4$, the error increases greatly with the increment of h/R. Therefore, the thick shell theory is recommended to give a more accurate result for high frequency modes when $h/R > 0.1$.

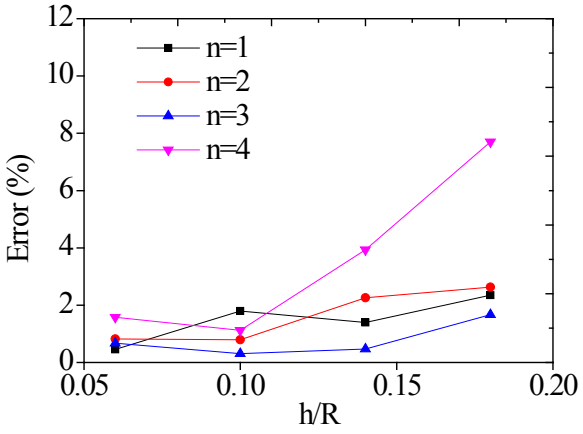

(a)

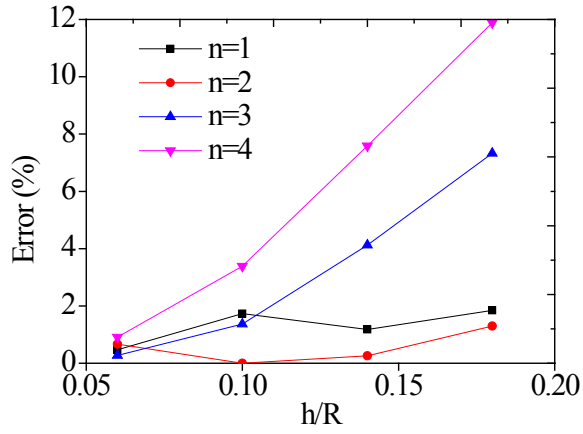

(b)

Fig. 4.8 Influence of h/R on nature frequency error. (a) Error of Love theory. (b) Error of Donnell theory.

4.3.2 Influence of the void on the natural frequency

A series of simplified circular voids with different sector angles were simulated to verify the analytical results calculated by the modal expansion approach. Their natural frequencies and the mode shapes are plotted in Fig. 4.9 and Fig. 4.10.

In both the analytical and DEM results, the natural frequencies decrease with the increment of the void size (defined by sector angle γ in Fig. 4.3). The significant influence of the void size on the natural frequency and the mode shape exists in the first order frequency, and the variation declines in higher modes.

For n=1, vibrations in the radial direction are induced primarily (Fig. 4.10a), which agrees with the assumption in Section. Hence the frequency errors defined in Eq. (4.38) are very tiny (less than 0.5%). While for $n \geq 2$, the errors increase (still less than 3%) . It is because the circumferential deflections increase with the vibration mode and the ignorance of circumferential deflections in higher order modes will result in the lower estimated frequencies. However, the proposed approach can still be viewed as a proper method for the estimation of the first order frequency of the lining with the void.

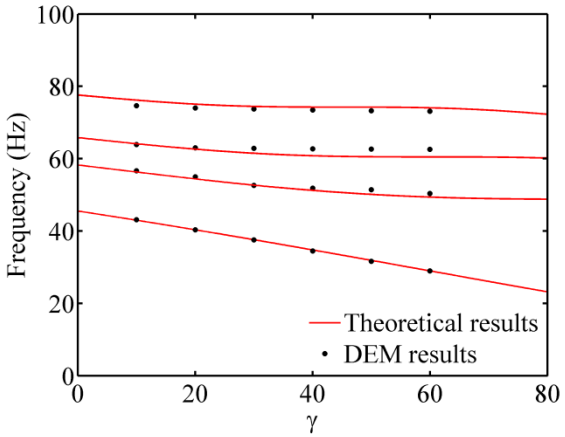

Fig. 4.9 The nature frequencies influenced by the void sector angle.

4.3.3 Influence of the rock-concrete interface stiffness on the nature frequency

The supporting system has a great influence on the natural frequency of a structure, and the decrease of the contact stiffness between the rock mass and the lining can reduce the natural frequency of the system (Chowdhury 1990). In Donnell theory, the influence of the interface stiffness on the nature frequency is illustrated in Fig. 4.11.

As expected, the nature frequencies increase with stiffness, and the most significant increase exists when the nature frequencies are small (vibration modes of n =1, 2, 3), as shown in Figure 6a. Since the shear stiffness is much smaller than normal stiffness, the nature frequencies are mainly affected by the normal stiffness. There is almost no variation of frequencies when the shear stiffness changes (Fig. 6b).

It is difficult to directly measure the exact stiffness of concrete-rock interfaces through conventional mechanical testing apporaches; nevertheless, the nature frequency measuring provides a new approach to estimate the stiffness.

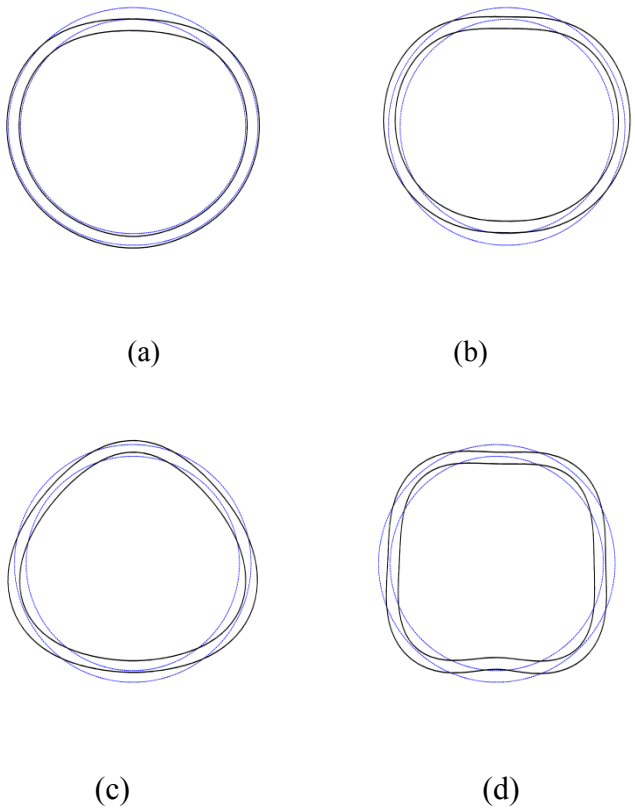

Fig. 4.10 One group of calculated mode shapes with the void sector angle of 60 °. (a) 28.98 Hz. (b) 50.40 Hz. (c) 62.61 Hz. (d) 73.11 Hz.

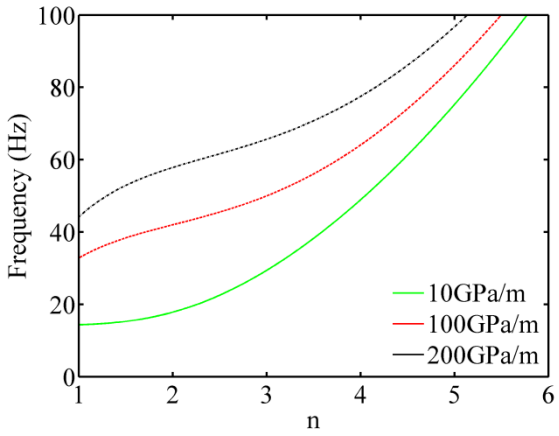

(a)

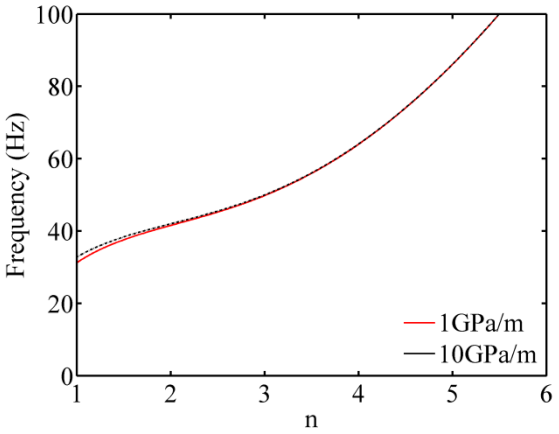

(b)

Fig. 4.11 Influence of concrete-rock interfaces on nature frequencies. (a) Nature frequencies corresponding to different normal stiffness of concrete-rock interfaces (the shear stiffness is 10 GPa/m.). (b) Nature frequencies corresponding to different shear stiffness of concrete-rock interfaces (the normal stiffness is 100 GPa/m.).

4.4 Summary

The nature frequencies of tunnel lining shell with the supporting of elastic rock-concrete interfaces were analyzed based on the Love-Timoshenko shell theory and Donnell-Mushtari shell theory. The accuracy and validity of proposed approach in the plane strain model were confirmed by comparison with the results of DEM numerical simulations.

When $n \geq 1$, the nature frequency estimated by Love theory is slight smaller than that of Donnell theory due to the neglecting of the tangential displacements and their derivatives. The relative error among the methods used in this paper is small in low frequency modes and increases with the increment of h/R. Even at the condition of $h/R > 0.1$, the nature frequencies in low modes ($n \leq 2$) can still be estimated accurately.

The natural frequencies decrease with the increment of the void size and the significant influence of the void size exists in the first order frequency. The first order natural frequency can be estimated accurately.

The elastic rock-concrete interface has a great influence on natural frequencies of the tunnel lining. For $n \geq 1$, the nature frequencies are mainly affected by the normal stiffness. The interface stiffness has the largest influence on low nature frequencies in vibration modes of $n = 1, 2, 3$. The tunnel lining shell frequency measurement also provides a new approach to estimate the interface stiffness.

CHAPTER 5

Field investigation on microtremors characteristics of tunnel concrete lining

5.1 Introduction

The damages of lining result in a localized reduction of the strength and stiffness of lining concrete. It has been found that the vibration modal parameters (e.g., the natural frequencies and damping ratios) of concrete structures are significantly sensitive to their damage status (Konno and Ohmachi, 1998). Meanwhile, the modal parameters can be acquired conveniently by dynamic tests (Vestroni and Capecchi, 2000; Lee, 2004), which provides a possible approach for effectively detecting the defects between the tunnel lining and the rock mass.

Microtremor as one type of ambient vibration, recently, has attracted more and more attentions in the study of the microtremor dynamic properties of concrete structures. Microtremors are low amplitude ambient vibrations (in the order of micrometers) of the ground caused by daily human activates such as movement of machinery in factories, motor cars and even people walking; as well as natural phenomena such as ocean waves, wind and volcano. Through analyzing the microtremor waves, some useful dynamic properties of a structure, like the natural frequency and amplitude, can be obtained. Thus far, the ambient test has been applied to various types of structures, such as bridges (Magalhas et al., 2009), buildings (Michel et al., 2008), historical structures (Júlio et al., 2008), and mechanical structures (Pierro et al., 2008). However, few attentions have been focused on the microtremor measurements for the damage identification of mountain tunnel linings (Gao, et al., 2012; Jiang, et al., 2012).

In this chapter, the feasibility of lining damage identification utilizing microtremor measurements was explored. The microtremors were measured on three spans of a tunnel, among which, the span S1 contains both cavities and cracks, the span S2 contains only cracks and the span S3 is healthy with no obvious cavities and cracks, The modal parameters including nature frequencies and damping ratios were extracted from the measured data. Finally, the relation between microtremor characteristics and the health conditions of tunnel was discussed.

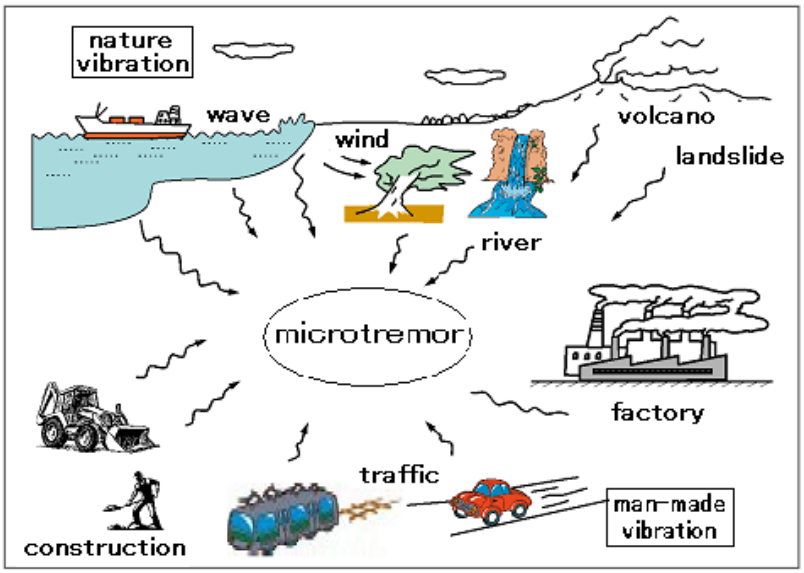

Fig. 5.1 The introduction of microtremor.

5.2 Description of microtremor measurement

5.2.1 Test tunnel

The measurement was carried out on the Satomi tunnel (see Fig. 5.2) located in the Sasebo City, Nagasaki Prefecture, Japan. The Satomi tunnel was built in 1992 with a length of 529 m. Some defects such as cracks and cavities began appearing in the lining concrete after it had been in service for over twenty years, due to the deterioration of lining concrete and the alteration of geological conditions. The tunnel inspection was carried out in detail in 2009 and some defects in the tunnel lining were confirmed. According to the inspection results, three spans with different health conditions were chosen for measurements (marked as S1, S2 and S3, as shown in Fig. 5.3). During the measurement, the traffic was controlled temporarily.

Fig. 5.2 Satomi tunnel.

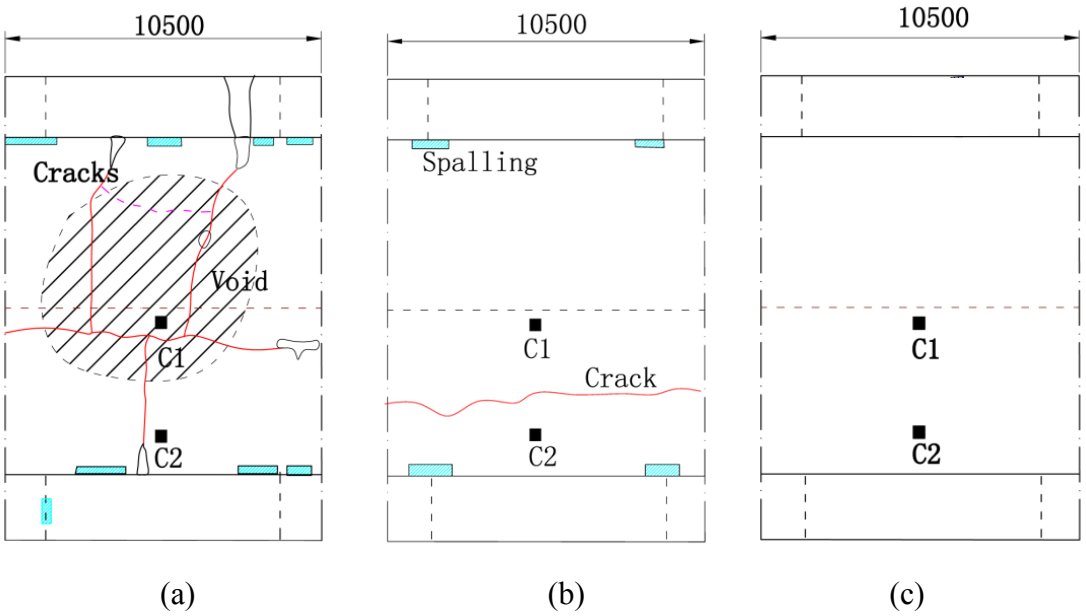

Fig. 5.3 Inspection results of spans S1, S2 & S3. (a) S1, severely damaged span (voids, three circumferential cracks and one axial crack on the lining surface). (b) S2, moderately damaged span (One axial crack on the lining surface). (c) S3, healthy span.

5.2.2 Measurement system

Since the amplitudes of microtremors usually range from several mgals to tens of mgals, accelerometers with high accuracy are required in microtremor measurements. In this study, compact type accelerometers with a resolution of 1 mgal were utilized (the specification parameters of the accelerometer is shown in Table 5.1). The measurement

system consists of the power, the PC & data acquisition device and two accelerometers, as shown in Fig. 5.4. One side alternation traffic regulation was implemented during measurements so that the tunnel lining on the other side could be measured. Tunnel inspection results showed that the defects often occur on the crown and arch (C1 & C2, see Fig. 5.5), therefore, only two measuring points on the crown and arch were selected during the limited measuring time. The measurements last for 300 seconds with an interval of 0.001 second, recording the microtremors when no traffic is allowed and only one side alternation traffic is allowed. The interfering signals which may be induced by the heavy traffic (e.g., heavy trucks) or measurement system are cut out. Accordingly a data record must be sufficiently long in order to reduce the influence of interfering signals. One example of the measured microtremors on the surface of tunnel lining in S3 are shown in Fig. 5.6.

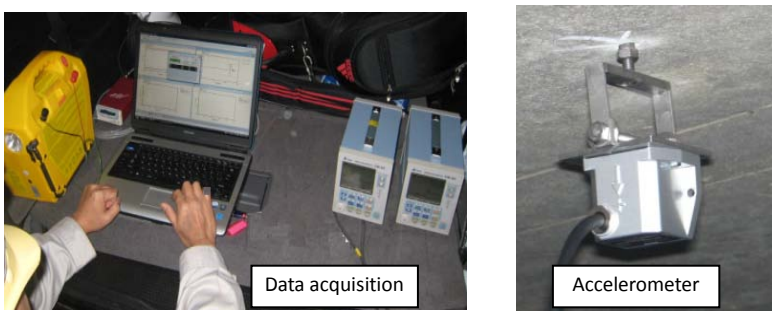

Fig. 5.4 Measurement system.

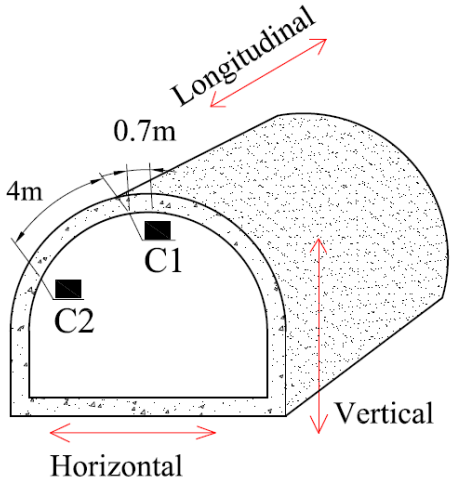

Fig. 5.5 Accelerometer configurations.

Table 5.1 Specification of accelerometer.

Max. Acceleration	±30m/s^2
Frequency Range	DC~100Hz
Resolution	1mgal
Size	37(H)×37(W)×40(D)
Weight	220g (include Cord)

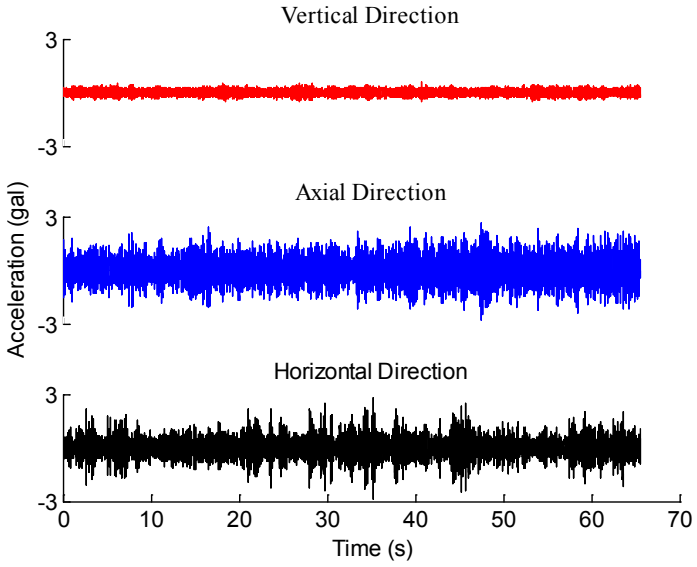

(a)

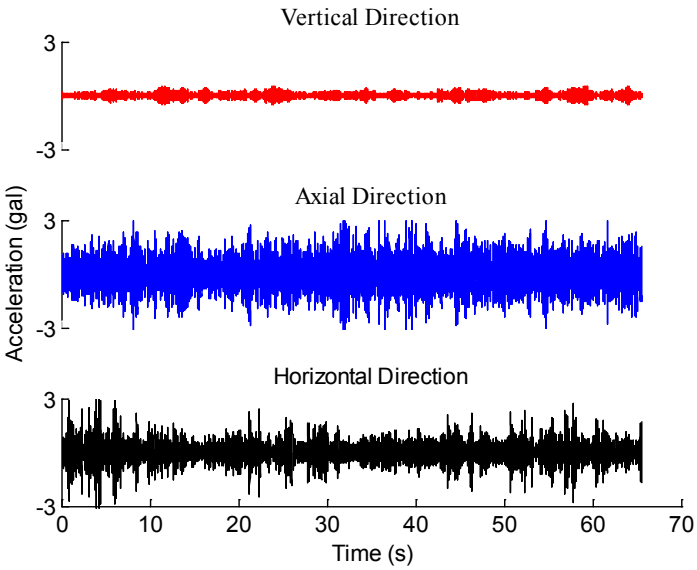

(b)

Fig. 5.6 The measured microtremors of accelerometer C1 in span S3. (a) No traffic allowed. (b) One side alternation traffic allowed.

5.3 Identification of natural frequencies

Due to the microtremors of tunnel lining have a high signal-to-noise ratio, the modal parameters are difficult identified in complicated method. Therefore, the simplest spectral peak-picking method (Bendat and Piersol, 1993), in which natural frequencies are simply determined from the peaks of the averaged frequency spectral, is adopted during the modal analysis. Relation between excitation inputs *F(t)* and output response *x(t)* can be expressed as (Bendat and Piersol, 1986):

$$P_{xx}(\omega) = \bar{H}(\omega) P_{FF}(\omega) H^T(\omega) \tag{5.1}$$

where the superscript overbar and *T* denote conjugate and transpose operations; ω is the frequency; $P_{FF}(\omega)$ and $P_{xx}(\omega)$ are the power spectra density (PSD) of inputs and outputs; $H(\omega)$ is the frequency response function (FRF). The FRF can be written as:

$$\begin{aligned} H(\omega) &= \sum_{i=1}^{N} \left(\frac{A_i}{j\omega - \lambda_i} + \frac{\bar{A}_i}{j\omega - \bar{\lambda}_i} \right) \\ &= \sum_{i=1}^{N} \left(\frac{\gamma_i \phi_i \phi_i^T}{j\omega - \lambda_i} + \frac{\bar{\gamma}_i \bar{\phi}_i \bar{\phi}_i^T}{j\omega - \bar{\lambda}_i} \right) \end{aligned} \tag{5.2}$$

where *N* is the number of modes, A_i and λ_i are the residue and pole, φ_i and γ_i are the mode shape vector and scaling factor. Suppose the natural excitation is white noise inputs, i.e.

$$P_{FF}(\omega) = C \tag{5.3}$$

where C is the constant, then Eq. (5.1) becomes

$$P_{xx}(\omega) = C\bar{H}(\omega) H(\omega)^T \tag{5.4}$$

It indicates that the PSD $P_{xx}(\omega)$ only depends on the FRF $H(\omega)$ of the structure and has a similar shape. FRF reveals extremely large values around the natural frequencies due to the resonance. Therefore, modal parameters (the natural frequency and the damping ratio) can be extracted from the PSD.

In this method, the input forces are assumed to be while noise and the dynamic resonant response is only dominated by one mode. This method is suitable only for the well separated modes and the lightly damped recording data. In spite of these limitations, the

spectral peak-picking method are still widely used for many civil engineering structures due to its intuitive frequency results, implementation simplicity, processing speed and low computational complexity even suffering from the peak merger problems.

The ANPSD was calculated from the node point accelerations and component of motion using Matlab (2003) with the Welch's averaged according to Eq. (4.38). Using the averaged algorithm, those energy peaks were eliminated in each individual spectrum that were caused by short-term disturbances (e.g. the passing trucks during measurement). Meanwhile, the loss of peak frequencies on nodes where mode shape was zero could also be avoided. Fig. 5.7 ~ 5.15 shows the calculated PSD of three spans, and Table 5.2 lists the identified peak frequencies.

- In the case of seriously damaged span S1 (Fig. 5.3a) in which voids and cracks exist, the NPSD in vertical direction is relatively small and is distributed at a wide range of frequencies (40-100 Hz) with ambiguous peaks especially when no traffic, and the peak nature frequency 32.2 Hz which is the lowest in all spans can be identified in the horizontal direction. Meanwhile, when one side alternation traffic is allowed, six frequency peaks (32.2 Hz, 68.4 Hz, 73.2 Hz, 79.1 Hz, 83.1 Hz and 88.9 Hz) can be identified.

- In the case of span S2 (Fig. 5.3b) in which only a crack exists, the first peak (around 60 Hz) in the vertical direction of C1 covers a wide range of frequency in Fig. 5.10a (no traffic) but has a narrow peak in Fig. 5.10b (one side traffic). In Fig. 5.12, three frequency peaks (60.5 Hz 81.0 Hz and 89.8 Hz) can be identified in both no traffic and one side traffic.

- In the case of the healthy span S2 (Fig. 5.3b), the frequency response curves have narrow and sharp shapes in three directions, as shown in Fig. 5.13 and Fig. 5.14. When one side alternation traffic is allowed, three frequencies (59.6 Hz, 78.1 Hz and 86.9 Hz) can be identified in Fig. 5.15b. When no traffic, only two peaks (78.1 Hz and 86.9 Hz) occur in Fig. 5.15a and the low frequency peak 59.6 Hz cannot be identified.

As mentioned above, the damages existing in seriously damaged span S1 (voids and cracks) change the dynamic parameters and result in great variations in peak frequencies: the lowest peak frequency 32.2 Hz and multiple frequency peaks. The identified peak frequencies in S2 (one axial crack) and S3 (health span) are similar even though there are some differences in the values. It indicates the voids behind the tunnel lining have the significant influences on the frequency response of tunnel lining. Compared to the condition that no traffic is allowed, the passing traffic can invoke more frequency peaks and some frequencies could not be identified when no traffic. In spite of that, the identified peak frequencies in both conditions are still identical and can be considered as natural frequencies of tunnel lining.

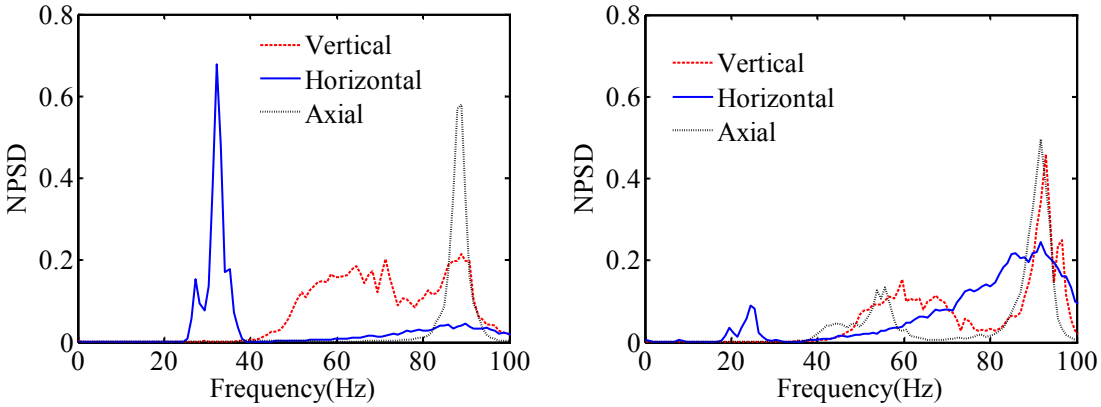

Fig. 5.7. The normalized PSD of S1 when no traffic is allowed. (a) C1. (b) C2.

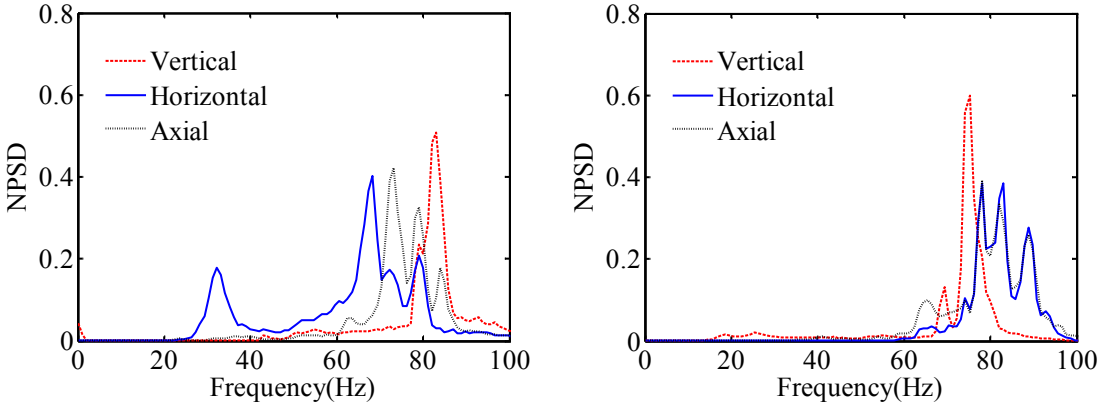

Fig. 5.8 The normalized PSD of S1 when one side alternation traffic is allowed. (a) C1. (b) C2.

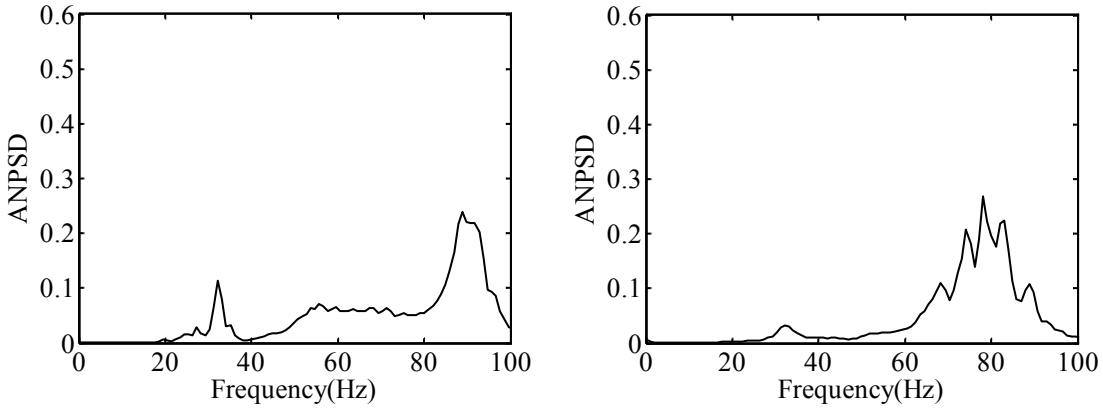

Fig. 5.9 The ANPSD of S1 (a) No traffic. (b) One side alternation traffic.

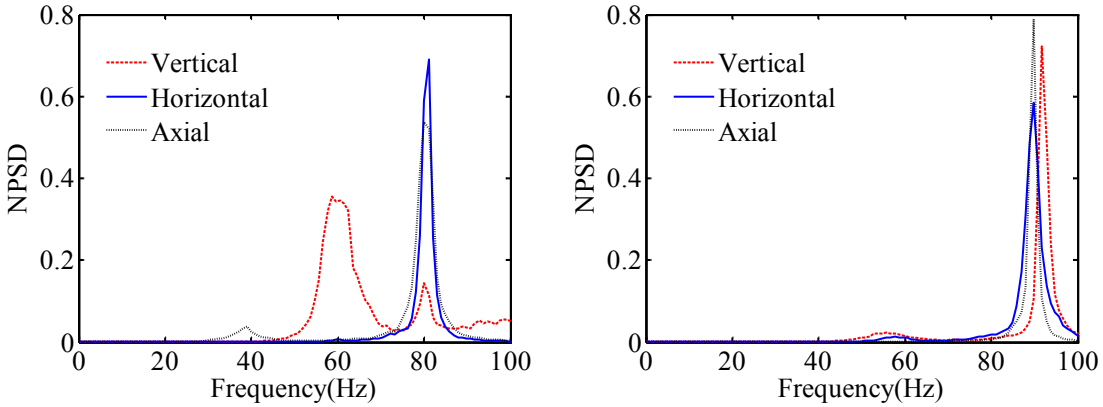

(a) (b)

Fig. 5.10 The normalized PSD of S2 when no traffic is allowed. (a) C1. (b) C2.

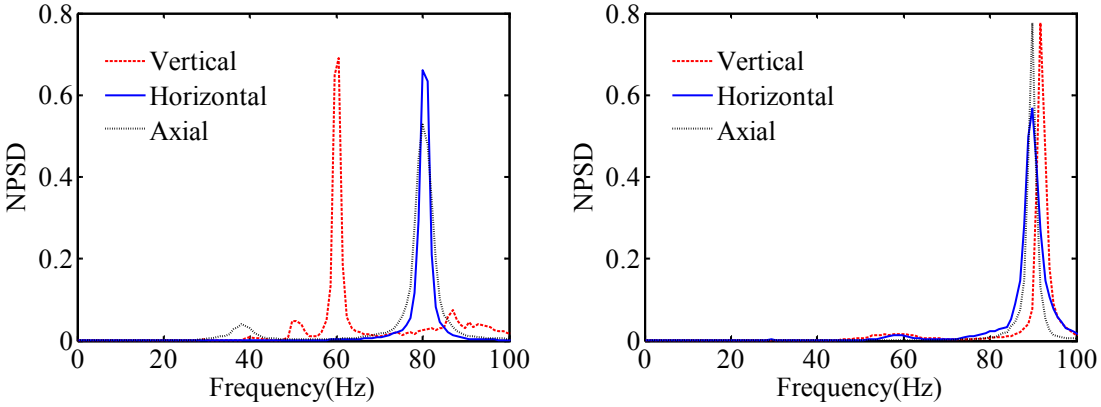

(a) (b)

Fig. 5.11 The normalized PSD of S2 when one side alternation traffic is allowed. (a) C1. (b) C2.

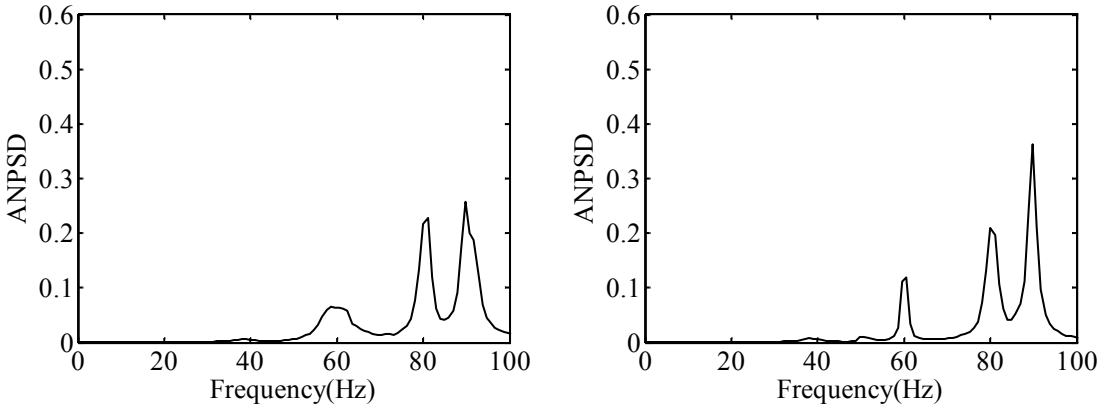

(a) (b)

Fig. 5.12 The ANPSD of S2. (a) No traffic. (b) One side alternation traffic.

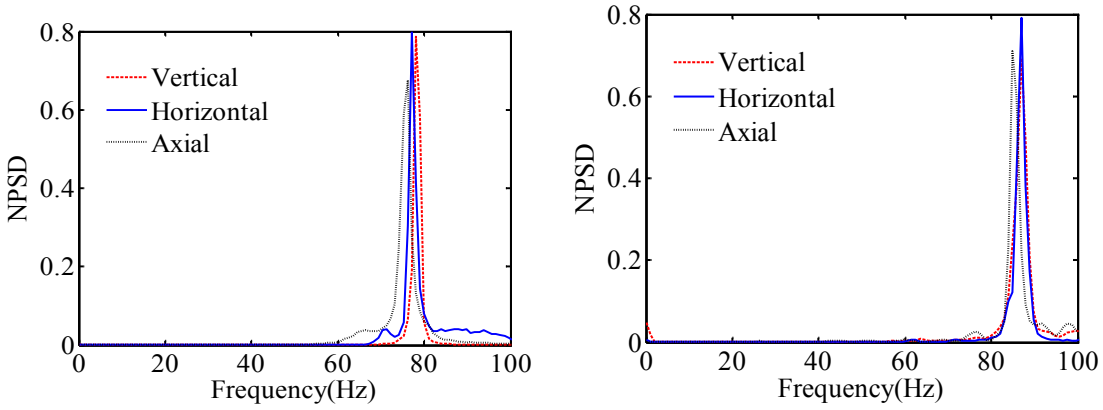

(a) (b)

Fig. 5.13 The normalized PSD of S3 when no traffic is allowed. (a) C1. (b) C2.

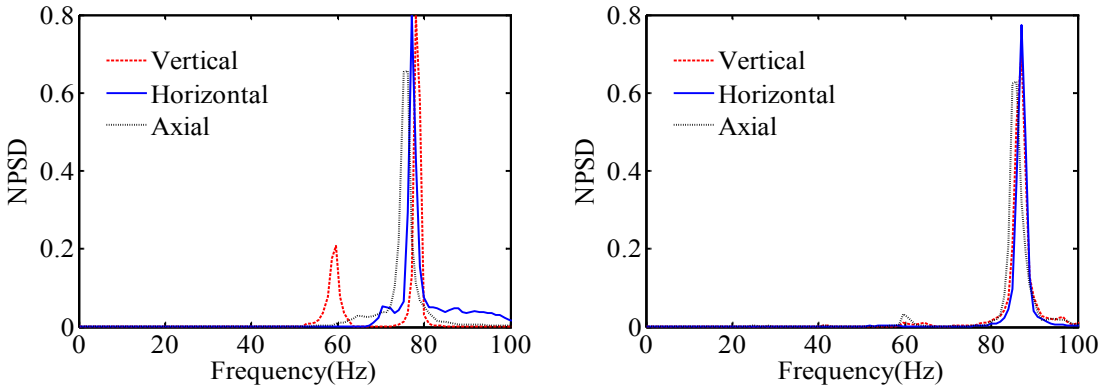

(a) (b)

Fig. 5.14 The normalized PSD of S3 when one side alternation traffic is allowed. (a) C1. (b) C2.

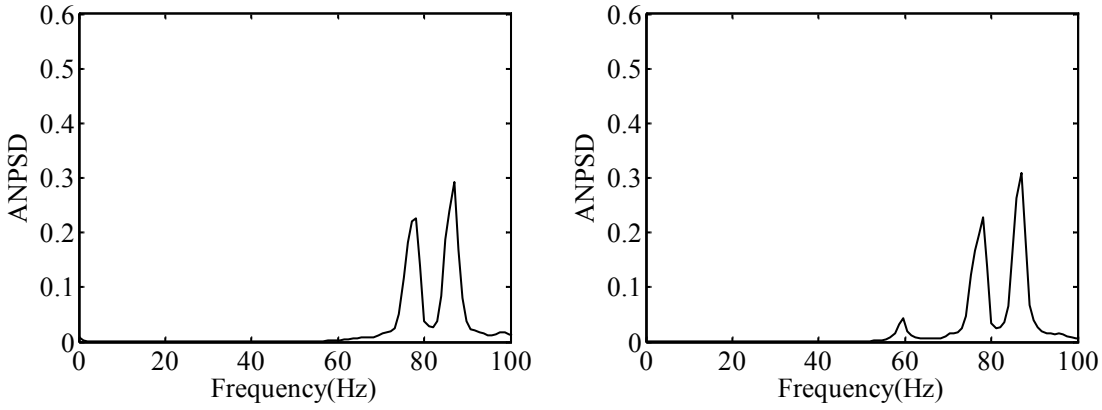

(a) (b)

Fig. 5.15 The ANPSD of S3. (a) No traffic. (b) One side alternation traffic.

Table 5.2 Calculated peak frequencies.

Span	Traffic condition	Peak frequencies (Hz)
S1	No traffic	32.2, 88.9
	One side alternation traffic	32.2, 68.4, 73.2, 79.1, 83.1, 88.9
S2	No traffic	60.5, 81.0, 89.8
	One side alternation traffic	60.5, 81.0, 89.8
S3	No traffic	78.1, 86.9
	One side alternation traffic	59.6,78.1,86.9

5.4 Identification of damping ratio

Compared to frequencies, damping properties have been less used for damage detection due to the difficulty in quantifying its magnitude (Williams and Salawu, 1997). However, recently researches suggest that damping is much more sensitive to local minor damage in structures, especially for small visually undetectable cracks (Modena et al., 1999).

In single-degree-of-freedom system, the FRF is given by

$$H(f)=\frac{f^2 f_n^2}{\left|k\left(f_n^2-f^2+j2Df_n f\right)\right|} \tag{5.8}$$

where f is the physical frequency in hertz (Hz), k is the stiffness, D is the damping ratio, f_n is the nature frequency. Substitute Eq. (5.8) in to Eq. (5.4), the PSD $G_{xx}(f)$ can be written as

$$G_{xx}(f)=C\left(\frac{f^2 f_n^2}{\left|k\left(f_n^2-f^2+j2Df_n f\right)\right|}\right)^2 \tag{5.9}$$

In this study, the NPSD curve was used to determine the damping ratio D, as shown in Fig. 5.16. The data points around the frequency peak in the curve were selected, and then the best-fit curve of these points was calculated according to Eq. (5.9). The damping ratio can be estimated using the function of best-fit curve. This method performs well only for structures with lightly damped and well separated modes. Since the concrete is a material with relatively small damping ratio (Malmgren et al., 2006), the damping ratio of tunnel lining concrete was estimated in most cases as listed in Table 5.3.

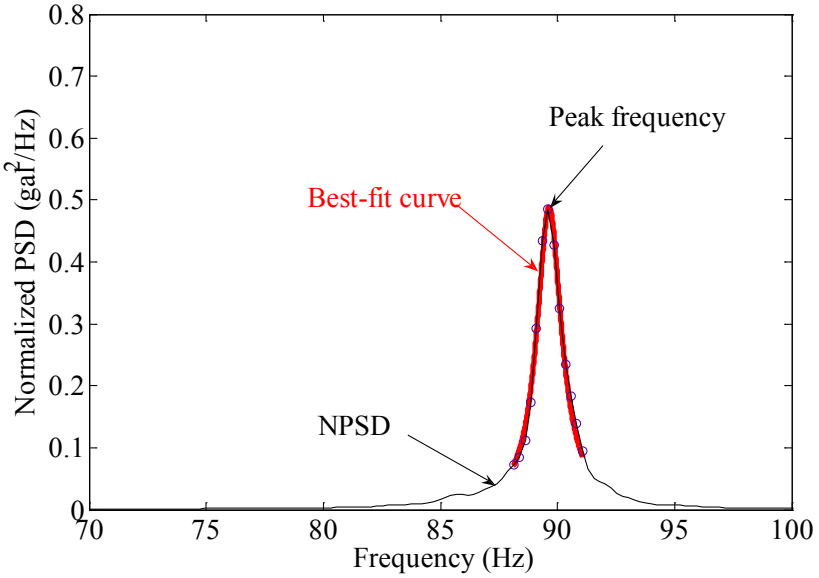

Fig. 5.16 NPSD and best-fit function for determination of predominant nature frequency fn and damping ratio D.

- In the healthy span S3, the damping ratios range from 0.011 to 0.015 (0.013 in average).

- In the moderate damaged span S2 in which one axial crack exists, the max damping ratio increases to 0.025 (0.018 in average) and larger than that of the healthy span S3. In other words, a larger damping ratio is measured due to the damage, which indicates that the damping ratio can be used as an indicator for the health status assessment in a tunnel lining.

- In the severely damaged span S1, the max damping ratio of C1 is 0.061, reveling that the damping ratio increases with the damage degree. The friction among the interacting surfaces of defects induces the dissipation of energy, which results in an increase of the apparent damping ratio. It is also worthy to notice that a few damping ratios (i.e. the vibration in vertical direction of C1 in S2) can't be estimated because they are heavily damped with close modes which cause the significant approximations as shown in Fig. 5.7.

Table 5.3 The calculated predominant nature frequency *fn* and damping ratio *D*.

Span	Direction	CH01				CH02			
		No traffic		One side alternation traffic		No traffic		One side alternation traffic	
		Frequency (Hz)	Damping Ratio	Frequency (Hz)	Damping Ratio	Frequency (Hz)	Damping Ratio	Frequency (Hz)	Damping Ratio
S1	V	-	-	83.1	0.029	91.8	0.021	74.6	0.023
		32.2	0.049	**32.2**	0.061	-	-	78.1	0.014
	H	-	-	68.4	0.033	-	-	83.0	0.024
		-	-	79.1	0.031	-	-	88.9	0.023
		-	-	73.2	0.035	-	-	78.1	0.014
	A	-	-	79.1	0.025	-	-	82.1	0.026
		88.9	0.021	83.9	0.020	90.8	0.027	88.9	0.023
S2	V	60.5	-	60.5	0.016	-	-	-	-
		81.0	0.021	-	-	91.8	0.017	89.8	0.014
	H	81.0	0.018	80.1	0.017	89.8	0.019	89.8	0.021
	A	81.0	0.023	80.1	0.025	89.8	0.015	89.8	0.014
S3	V	-	-	59.6	0.030	-	-	-	-
		78.1	0.012	78.1	0.013	86.9	0.014	86.9	0.014
	H	77.1	0.011	77.1	0.012	86.9	0.010	86.9	0.012
	A	76.1	0.015	76.1	0.015	85.0	0.014	85.5	0.015

5.5 Summary

In this chapter, the microtremors on the lining of the Satomi tunnel were measured at three spans, including the S1 span (with cracks and cavities existing in the lining concrete), the S2 span (only cracks exist) and the S3 span (healthy lining without obvious cracks and cavities). The normalized power spectrum density (NPSD) were calculated and analyzed, and the modal parameters including natural frequencies and damping ratio were extracted with the peak picking methods. The main conclusions are summarized as following:

(1) In the healthy span S3 and moderately damaged span S2 (one axial crack), the identified peak frequencies are similar, even though some differences still exist between these values.

(2) In seriously damaged span S1 (voids and cracks), multiple frequency peaks with the lowest peak frequency 32.2 Hz occur. Compared to span S2, the damages in span S1 result in great variations in peak frequencies, reveling that the voids behind the tunnel lining have the significant influences on the frequency response.

(3) The passing traffic can invoke more frequency peaks and some frequencies could not be identified when no traffic. In spite of that, the identified peak frequencies in both conditions are still identical and can be considered as natural frequencies of tunnel lining.

(4) For the purpose of quantitative evaluation of the span health, the damping ratios are calculated and analyzed. As the span healthy worsens, the damping ratio increases. However, damping ratios couldn’t be indentified in some cases because of heavily damped and the closely spaced modes.

CHAPTER 6

Numerical simulation about vibration characteristics of mountain tunnel lining

6.1 Introduction

Comparing with theoretical and experimental studies, the numerical simulation provides a convenient and low-cost approach to study the dynamic problems, especially when theoretical solutions are difficult to obtain.

In this chapter, numerical simulations were performed by using the UDEC to investigate the vibration behavior of tunnel lining. The natural frequency and the mode shape were calculated and analyzed. The rock-concrete interfaces represented by the interface element and their stiffness were estimated based on the frequency response. The influences of the voids and their geometrical parameters, rock type and concrete type on frequency response of tunnel lining were studied. The relationship between the peak frequency and the stress state of the tunnel lining were also discussed based on the numerical results.

6.2 Numerical simulations

6.2.1 Numerical model

In these old tunnels that were built with the fore-poling method, the poling board was used instead of shotcrete so that incomplete contacts usually exist between rock mass and poling board, as shown in Fig. 6.1. The coring survey of lining showed that the temporary supports (wooden boards) were closely bonded with the lining concrete. They were substantially consolidated subjected to the compression stresses from the surrounding rock mass and achieved high strength. Therefore, instead of treating the temporary support as a separate layer, we considered them as a part of concrete lining in numerical simulations for simplification. Their contacts with the surrounding rock mass were simplified to weak concrete-rock interfaces with low normal and shear stiffness. (i.e., the interfaces are treated as inner boundaries in the DEM) (UDEC 2000). The Mohr-Coulomb model and Coulomb slip model were adopted to represent the mechanical behavior of rock mass and interface, respectively. Those types of elements can effectively simulate the dynamic deformational behavior of rock mass, lining concrete and rock-concrete interface. The size of the numerical model and the positions of monitoring points (C1 and C2) are in accordance with the tested tunnel, as shown in

Fig. 6.2. In the two-dimensional model, only the vibration histories in vertical and horizontal directions were recorded. Stress equivalent to an overburden of 35 m was applied on the upper boundary of the model. The physico-mechanical properties of the surrounding rock mass and lining concrete are listed in Table 6.1 which are typical values of properties of the rock mass and concrete lining encountered in the construction of this tunnel and can be obtained from the unconfined and triaxial compression tests (Gao et al. 2014). Since the microtremor doesn't cause the failure of rock mass and lining concrete, the tensile strength, cohesion and friction angle have no influence on the microtremor vibration behavior of the model.

A static equilibrium calculation was achieved before the start of dynamic analyses. In dynamical calculations, a stationary Gaussian white noise with power of 60 dBW and a frequency range of 0 to 100 Hz was input on the floor of tunnel in terms of a normal stress to represent the exciting source (e.g., passing vehicles). The Rayleigh damping with a ratio of 1% was utilized during dynamic calculations to represent the attenuation of materials. The boundaries of model were set as viscous boundaries to absorb the stress waves passing by and minimize wave reflections at boundaries. 32768 discrete time signal data at each monitoring point were recorded during numerical simulations with a sampling interval of 0.001s.

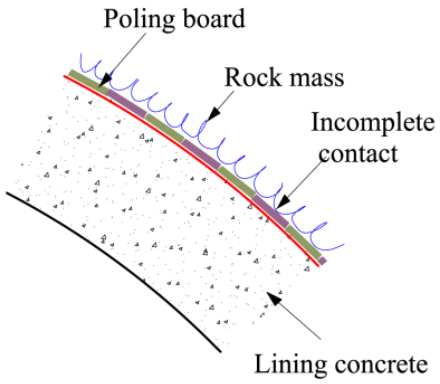

Fig.6.1 A cross-sectional view of the tunnel lining built by the fore-poling method.

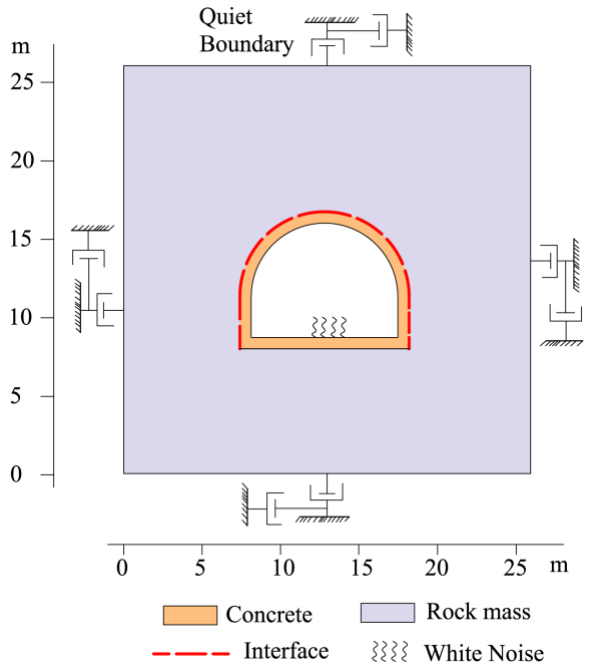

Fig.6.2 Model of numerical simulation.

Table 6.1 Material properties of rock mass and lining concrete used in the numerical simulations. The material properties of rock mass and lining concrete were acquired from in-situ investigation data of this tunnel (Gao et al. 2014).

Parameters	Units	Rock mass	Concrete
Density	kg/m^3	2550	2500
Elastic modulus	GPa	30	22
Poisson ratio	-	0.22	0.28
Tensile strength	MPa	7.2	1.4
Cohesion	MPa	10.3	2.7
Friction angle	°	30	35

6.2.2 Parameter optimization

The proper size of the spatial elements needs to be determined by taking into account the lowest velocity and the highest frequency of the wave propagation (Saenger et al. 2000). Rayleigh wave is generally considered as the lowest wave velocity (Zerwer et al., 2002) and its velocity V_R can be calculated by the following equation (Jaeger et al., 2007):

$$V_R = \frac{(0.874032 + 0.200396v - 0.0756704v^2)}{\sqrt{\frac{2(1-v)}{1-2v}}} V_P \tag{6.1}$$

where V_p is the longitudinal wave and v is the Poisson's ratio of the concrete. In the numerical simulations, V_p of concrete was assumed as 3127 m/s, and V_R was calculated by Eq.(5) as 1857 m/s. Maximum frequency f_{max} of the white noise is 100 Hz, and the minimum wave length λ_{min} (λ_{min}= V_R / f_{max}) was calculated as 18.57 m. The element size should be smaller than approximately one-tenth of the wavelength associated with the highest frequency to simulate the wave transmission accurately (Kuhlmeyer and Lysmer, 1973). Hence, an element size of 0.2 m was adopted in this study in order to acquire the accurate results.

The supporting system has a great influence on the natural frequency of a structure, and the decrease of the contact stiffness of concrete-rock interface will reduce the natural frequency of the system (Chowdhury, 1990). It is difficult to directly measure the exact stiffness of concrete-rock interface through conventional mechanical testing; nevertheless, its stiffness can be estimated from the vibration properties of tunnel lining. The frequency responses of lining in low frequency range are defined by the dynamic stiffness of the structural element which can be expressed by rock mass and concrete stiffness, concrete thickness and element support condition (Allen et al., 2005). After measuring the stiffness of rock mass and concrete and the thickness of concrete, the stiffness of concrete-rock interface, which plays the role of supporting, can be estimated based on the frequency response of the preliminary numerical studies.

A group of rock-concrete interfaces with different stiffness were simulated and their mechanical properties are listed in Table 6.2. The power spectra of obtained vibration histories in cases J-2-10, J-4-10 and J-2-100 were calculated to find the peak frequencies,

as shown in Fig. 6.3a. The power spectra are influenced greatly by the normal stiffness (cases J-2-10 and J-4-10) while there is almost no variation at different shear stiffness (cases J-2-10 and J-2-100), which indicates that the normal stiffness rather than the shear stiffness plays dominated role in the frequency response of tunnel lining. With the decrease of the normal stiffness of interfaces, the peak frequency decreases, and the frequency difference between the first and the second modes increases, as shown in Fig. 6.3b. The peak frequency-normal stiffness curves approximate linear relations, indicating that the peak frequencies change proportionally with the normal stiffness of the rock-concrete interface. Based on the results of numerical simulations, the normal stiffness of the rock-concrete interface of the healthy span S1 can be estimated as around 265 MPa/m. By using this normal stiffness, the simulated peak frequencies for the first, second and third modes are 56.8 Hz, 77.2 Hz and 85.6 Hz (see Fig. 6.3b), respectively, which agree well with those measured values (56.6 Hz, 78.1 Hz and 86.9 Hz), thus giving reasonable verification to the performance of the numerical approach used in this study.

The in-plane bending and symmetric mode shapes of the tunnel lining could be calculated based on the recorded vibration histories of lining. The mode shapes of models with different interface stiffness are similar, and one typical group of modes are plotted in Fig. 6.4.

Table 6.2 Material properties of rock-concrete interface used in the numerical simulations.

Cases	Normal stiffness (MPa/m)	Shear stiffness (MPa/m)	Tensile strength MPa
J-5-10	500	50	0
J-4-10	400	40	0
J-3-10	300	30	0
J-2-100	200	2	0
J-2-10	200	20	0
J-1-10	100	10	0

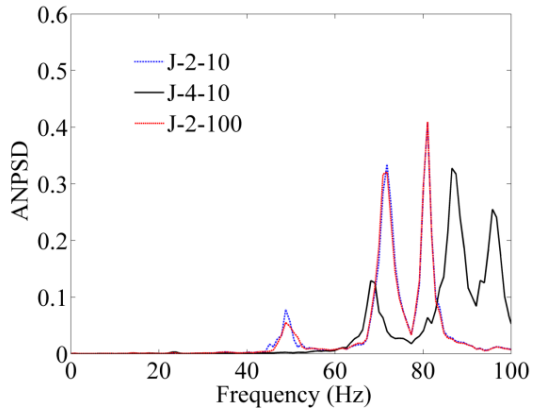

(a)

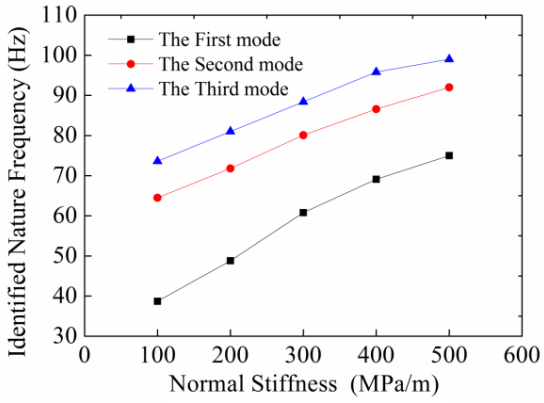

(b)

Fig. 6.3 Influence of the concrete-rock interface on the power spectrum. (a) The power spectra of tunnel lining corresponding to different normal and/or shear stiffness of concrete-rock interface in cases J-2-10, J-4-10 and J-2-100. (b) The relation between the peak frequency and the normal stiffness of concrete-rock interface in cases J-1-10, J-2-10, J-3-10, J-4-10 and J-5-10.

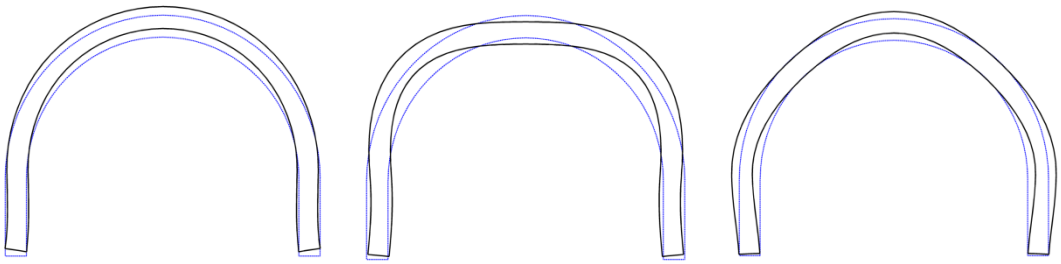

(a) (b) (c)

Fig. 6.4 One group of calculated mode shapes with the normal stiffness of 200 MPa/m (the ratio of shear to normal stiffness is 10%). (a) 48.0 Hz. (b) 71.8 Hz. (c) 81.0 Hz.

6.3 Influence of voids

The voids can induce the increment of deformation and stress in the close vicinities, causing serious damages on tunnel linings. For a planer model, the void location, the void depth and the void arc length are the main geometrical parameters of voids influencing the interacting between lining and rock mass. A series of simplified circular voids located at the arch and crown of tunnel lining where voids usually exist according to in-situ survey, were simulated to analyze the response of vibration behavior of lining to these parameters. A schematic view showing the parameters defining the status of voids is presented in Fig. 6.5, and the parameters of different cases are listed in Table 6.3. Mechanical properties of interface adopted the values of case J-2-10 in the following simulations. It should be noticed that the actual voids existing behind lining are three-dimensional in shape. To satisfy the plane strain assumptions in two-dimensional models, at here, voids with long length in the orientation of the tunnel axis were assumed.

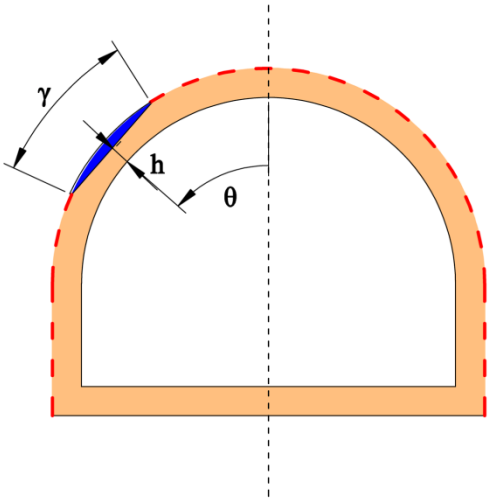

Fig. 6.5 Schematic view of a void at rock-concrete interface. Void location: angle θ (VL), void arc length: sector angle γ (VS) and void depth: h (VD).

Table 6.3 Values of void parameters for different cases. Void location: angle θ (VL), void arc length: sector angle γ (VS) and void depth h (VD).

Case	θ (°)	γ (°)	h (m)	Peak frequencies(Hz)
VL-1	0	60	0.6	32.4, 66.5, 78.5
VL-2	30	60	0.6	28.7, 38.3, 45.0, 65.1, 78.5
VL-3	60	60	0.6	26.3, 44.1, 65.1, 75.6, 80.8
VS-L0-1	0	10	0.6	47.3, 71.2, 81.0
VS-L0-2	0	20	0.6	42.9, 70.6, 79.8
VS-L0-3	0	30	0.6	34.5, 69.0, 78.7
VS-L0-4	0	40	0.6	33.2, 68.4, 78.6
VS-L0-5	0	50	0.6	32.7, 68.7, 78.7
VS-L0-6	0	60	0.6	32.4, 66.5, 78.5
VS-L60-1	60	10	0.6	30.9, 49.3, 68.9, 80.8
VS-L60-2	60	20	0.6	30.7, 48.1, 66.9, 80.5
VS-L60-3	60	30	0.6	30.4, 48.0, 66.2, 80.2
VS-L60-4	60	40	0.6	29.0, 47.7, 65.2, 80.5
VS-L60-5	60	50	0.6	26.8, 44.5, 65.0, 75.9 80.8
VS-L60-6	60	60	0.6	26.3, 44.1, 65.1, 75.6 80.8
VD-L0-1	0	60	0.2	35.4, 64.3, 78.3
VD-L0-2	0	60	0.4	33.9, 65.7, 79.1
VD-L0-3	0	60	0.5	33.7, 68.3, 79.0
VD-L0-4	0	60	0.6	32.4, 66.5, 78.5
VD-L60-1	60	60	0.2	30.0, 40.2, 65.7,75.7, 80.4
VD-L60-2	60	60	0.4	28.2, 43.7, 65.7, 75.7, 78.8
VD-L60-3	60	60	0.5	27.2, 44.3, 65.5, 75.7, 80.4
VD-L60-4	60	60	0.6	26.3, 44.1, 65.1, 75.6, 80.8
V-L0-L60	0 & 60	30	0.6	24.3, 32.0, 47.5, 62.9, 69.6, 72.9, 80.6, 87.6

6.3.1 Influence of void location (angle θ)

The influence of void location defined by angle θ was analyzed by using the cases VL-1, VL-2 and VL-3 with a void depth of 0.6 m and a sector angle of 60°. Their power spectra are shown in Fig. 6.6, peak frequencies are listed in Table 4 and the corresponding mode shapes are shown in Fig. 6.7.

In case VL-1, three frequency peaks (32.4 Hz, 68.7 Hz and 78.5 Hz) can be identified, and their mode shapes are symmetric, which are similar to the mode shapes of models without voids (Fig. 6.4). In cases VL-2 and VL-3, five frequency peaks can be identified (28.7 Hz, 38.3 Hz, 45.0 Hz, 65.1 Hz and 78.5 Hz in case VL-2; 26.3 Hz, 44.1 Hz, 65.1 Hz, 75.6 Hz and 80.8 Hz in case VL-3), and their mode shapes are non-symmetric because the void is not located on the central axis (Fig. 6.8). Except the first peak frequency, the peak frequencies of VL-2 are smaller than that of VL-3 with similar mode shapes. Meanwhile, the first peak frequency decreases gradually in these three cases (32.4 Hz in case VL-1, 28.7 Hz in case VL-2 and 26.3 Hz in case VL-3) as angle θ increases. In summary, as angle θ increases, the first peak frequency decreases and a few additional peak occurs due to the existence of voids not located on the central axis, which are in accordance with the in-situ measurement results in span S2 in which voids exist.

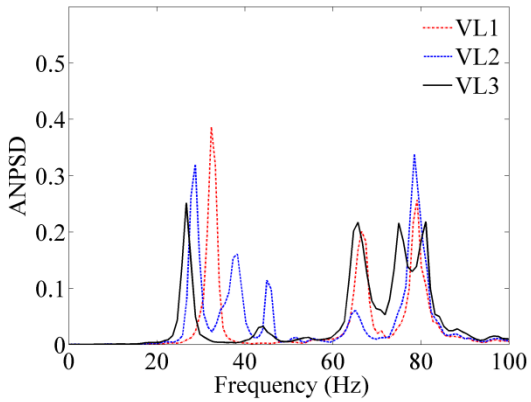

Fig. 6.6 The power spectrum of tunnel lining corresponding to different void locations (angle θ).

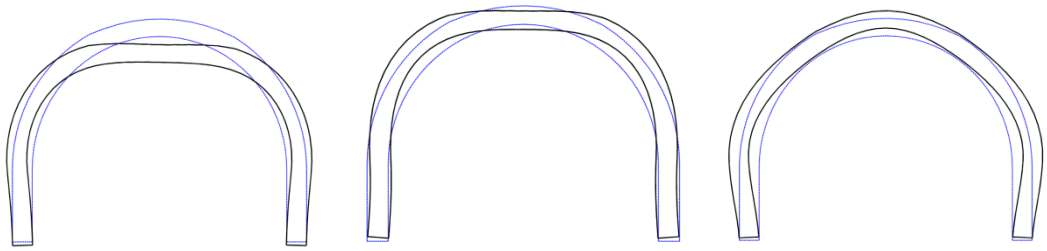

(a) (b) (c)

Fig. 6.7 The mode shapes of tunnel lining incase VL-1. (a) 32.4 Hz. (b) 68.7 Hz. (c) 78.5 H.

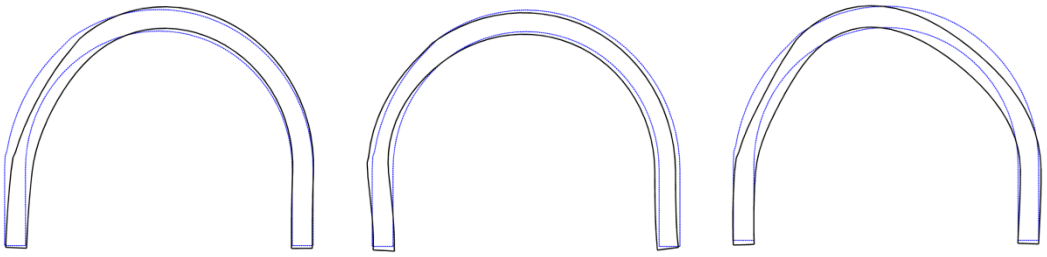

(a) (b) (c)

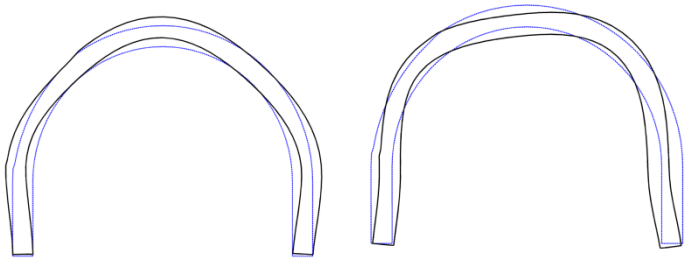

(d) (e)

Fig. 6.8 The mode shapes of tunnel lining incase VL-3. (a) 26.3 Hz. (b) 44.1 Hz. (c) 65.1 Hz. (d) 75.6 Hz. (e) 80.8 Hz.

6.3.2 Influence of void arc length (sector angle γ)

The influence of void arc length defined by sector angle γ was analyzed using the cases with different void locations, but equivalent void depth of 0.6 m located in tunnel crown (cases VS-L0-1 ~ VS-L0-6) and in arch (cases VS-L60-1 ~ VS-L60-6), respectively. The calculated power spectra are shown in Fig. 6.9 and the relations between the peak frequency and the sector angle are shown in Fig. 6.10.

In the cases with a void in crown ($\theta = 0°$), three frequency peaks can be identified (Fig. 6.9a). In the cases with a void in arch ($\theta = 60°$), four frequency peaks (cases VS-L60-1, VS-L60-2 and VS-L60-3) and five frequency peaks (cases VS-L60-4 and VS-L60-5) can be identified, even though the second peak (around 45 Hz) is not as obvious as others, as shown in Fig. 6.9b. These reveal that additional vibration modes can be evoked due to the increase of void size (arc length). In Fig. 6.10, as the void size increases, peak frequencies decrease. The first peak frequency of the case with a void in crown descents sharply when $\gamma < 30°$, while no obvious changes occur in other two peak frequencies (Fig. 6.10a). The first peak frequencies in the cases with avoid in arch are much smaller than those with voids in crown with the same void size, and the difference becomes larger when the void size is small. This indicates that the smaller peak frequency could be evoked when voids exist in arch.

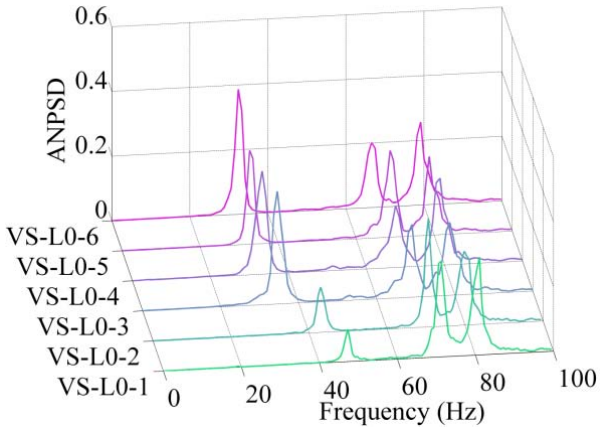

(a)

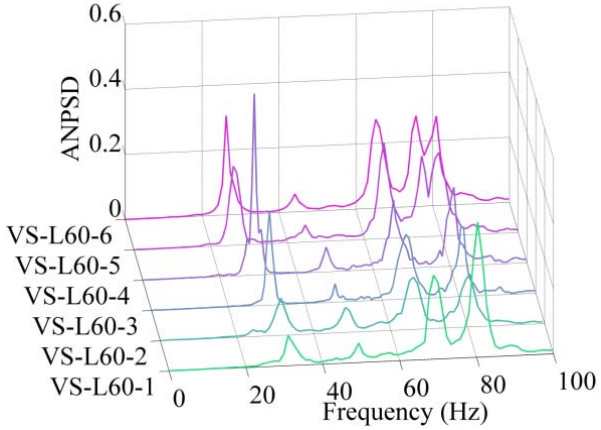

(b)

Fig. 6.9 The power spectrum of tunnel lining corresponding to different void sector angles.

(a) $\theta = 0°$. (b) $\theta = 60°$.

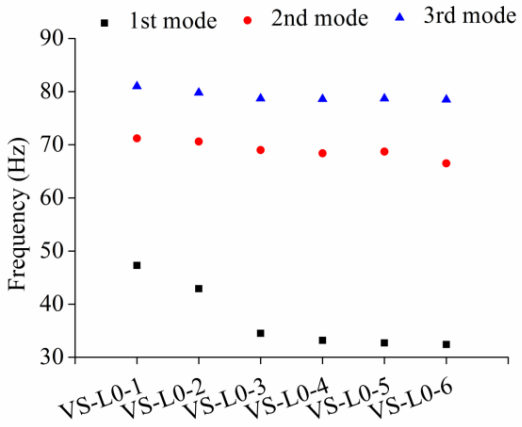

(a)

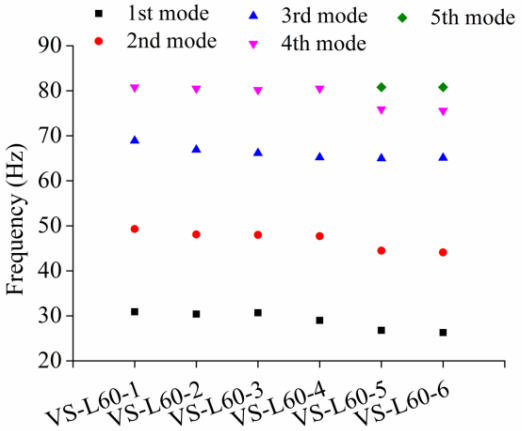

(b)

Fig. 6.10 The relations between the peak frequency and the void sector angle. (a) $\theta = 0°$. (b) $\theta = 60°$

6.3.3 Influence of void depth *h*

The influence of void depth was analyzed by using the cases with different void depths when a void is located in tunnel crown (cases VD-L0-1, VD-L0-2, VD-L0-3 and VD-L0-4) and arch(cases VD-L60-1, VD-L60-2, VD-L60-3 and VD-L60-4), respectively. The calculated power spectra are shown in Fig. 6.11.

The variations of peak frequencies in different models are relatively small (less than 4 Hz). That is to say the void depth is probably a negligible parameter influencing the frequency response of tunnel lining with voids. However, the existence of voids usually reduces the thickness of the lining, causing a considerable reduction of the lining resistance. Especially in some occasional cases, the thickness of lining could drop to below 20 cm as shown in Cases VD-L0-1 and VD-L60-1, in which the steep decrease of lining thickness resulted in significant increase of stress. Therefore, attention needs to be paid on the void thickness which could not be identified by the frequency response, and additional damage detecting methods (e.g., boring) are recommended if necessary.

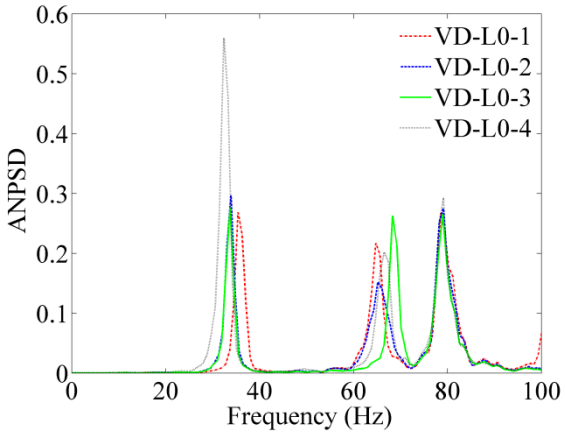

(a)

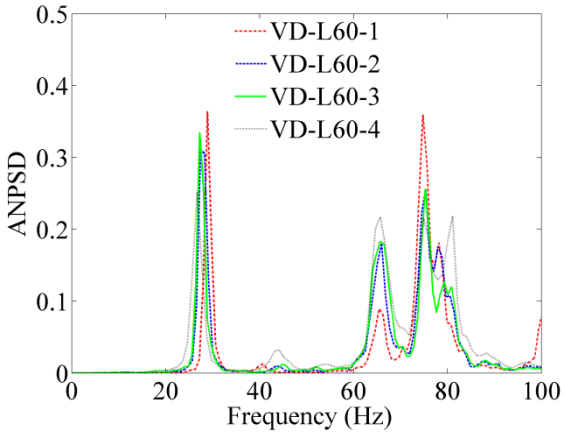

(b)

Fig. 6.11 The power spectrum of tunnel lining corresponding to different void depths. (a) $\theta = 0°$. (b) $\theta = 60°$.

6.3.4 Influence of multiple voids

Not only a single void, but also multiple voids are often detected between the rock mass and the tunnel lining in a single span (as shown in damaged span S2), and it is difficult to detect the void distribution exactly due to the limitation of the detection method. One model with two simplified voids (case V-L0-L60, one void on the crown and the other on arch as listed in Table 6.3) was adopted as a typical example to analyze the influences of multiple voids. The calculated power spectra are shown in Fig. 6.12.

Eight frequency peaks (24.3 Hz, 32.0 Hz, 47.5 Hz, 62.9 Hz, 69.6 Hz, 72.9 Hz, 80.6 Hz, and 87.6 Hz) could be identified, revealing that additional vibration modes can be evoked due to the increase of the void number. Meanwhile, the first peak frequency of this case is less than those of the cases VS-L0-3 and VS-L60-3, which indicates that the first peak frequency of the lining with multiple voids is less than that of the lining with a single void.

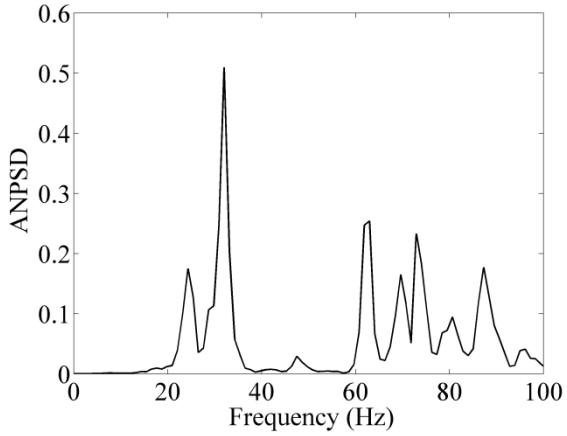

Fig. 6.12 The power spectrum of tunnel lining corresponding to multiple voids.

6.4 Influence of lining concrete type

The mechanical properties of three typical types of concrete that are commonly used in tunnel lining constructions are listed in Table 6.4. The variation of elastic modulus usually causes changes in the peak frequency of tunnel lining, as demonstrated in Fig. 6.13. As the elastic modulus decreases, the peak frequencies also decrease gradually, and larger variation occurs in the second and third frequency peaks, showing that the peak frequencies in higher modes are more sensitive to the change of elastic modulus of lining concrete.

Table 6.4 Properties of different types of concrete used in numerical simulations (Hatanaka et al., 2010)

Concrete type	Density (kg/m^3)	Elastic modulus (GPa)	Poisson's ratio
C20	2500	22	0.27
C30	2500	30	0.25
C50	2500	35	0.2

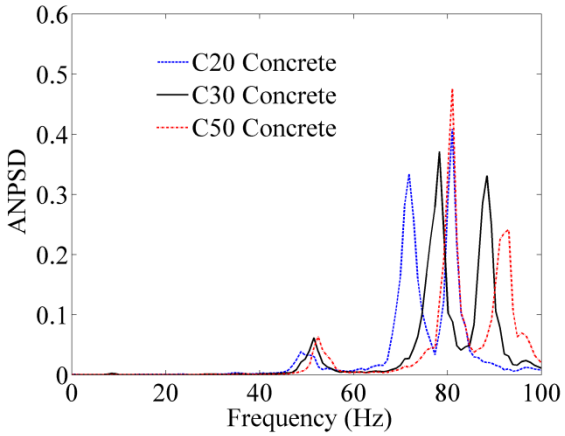

Fig. 6.13 The power spectrum of the tunnel lining constructed with different types of concrete.

6.5 Influence of rock type

Besides the rock-concrete interface and concrete lining, the surrounding rock mass remains as another key factor affecting the dynamic properties of the tunnel system. The properties of typical types of rocks are listed in Table 6.5 and the power spectra of tunnel lining supporting different rock types are shown in Fig. 6.14. Except the case of the weathered rock, there is no obvious influence of rock type on the peak frequencies and the variation of the spectrum amplitudes among them is less than 10%. In the case of the weathered rock, a number of peaks with low peak frequencies appear, rendering it difficult to clearly identify the peak frequencies. These results indicate that variations of peak frequencies of the tunnel lining that induced by flaws in lining (e.g., voids) can be identified obviously when the surrounding rock mass is unweathered, while special attentions need be paid in the peak picking if the rock mass is highly weathered.

Table 6.5 Properties of rocks used in numerical simulations (Song and Cho, 2010).

Material	Density (kg/m^3)	Elastic modulus (GPa)	Poisson ratio
Hard rock	2600	47	0.2
Medium rock	2550	30	0.22
Soft rock	2500	20	0.25
Weathered rock	2260	7	0.3

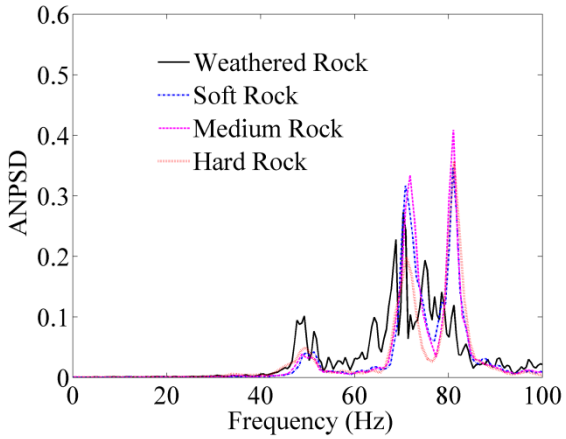

Fig. 6.14 The power spectrum of tunnel lining with different types of rocks.

6.6 Evaluation of influences of the voids on the lining stress

When a void exists behind a tunnel lining, the stress state of the lining will change significantly around the void into the state that the lining undergoes compression on the inner surface and tension on the outer surface. At here, outer surface stands for the surface of lining closer to the rock mass. The stress variation around the unsupported surfaces of the void may cause large deformation. These surfaces also contribute to the deflection of waves, and change the peak frequencies of lining. Furthermore, the unsupported length of the void changes the stiffness of the total supporting system, thus strongly affecting their frequency responses.

In-situ measurement and numerical simulation results have revealed that the first peak frequency of the lining decreases due to the existence of voids and is closely related to the geometrical parameters of the voids. The relations of the first peak frequency and the lining stresses (e.g. maximum principal stress σ_1, minimum principal stress σ_3, difference stress σ_1-σ_3 and maximum bending moment M) are shown in Fig. 6.15. Those presented indicators were normalized by ρhr and the first peak frequency f was normalized by f_I, where ρ is the unit weight of the ground material, h is the overburden depth, r is the tunnel radius and f_I is the first peak frequency of the models without voids (i.e. case J-2-10) (Meguid and Dang, 2009). Best-fit curves of the data points (σ_1, σ_1-σ_3 and M) exhibit high determination coefficients (0.91 in Figs. 6.15ab and 0.85 in Fig. 6.15c), which means that σ_1, σ_1-σ_3 and M could be well estimated based on the first peak frequency by the best-fit function. There is a larger dispersion of data around the curves in Fig. 6.15c (σ_3), and the estimated coefficient of determination is around 0.66.

In Fig. 6.15, the distribution of stress indicators (σ_1, σ_3, σ_1-σ_3 and M) exhibits a two-stage character. In the range of $f / f_I > 0.75$, the indicators are relatively small and vary in a small range, indicating that the tunnel lining is in a stable state with low stresses. Cases In-Ro-1~5 and In-Co-1~3 fall within this range, revealing that the influences of rock type and concrete type on stresses are small. In the range of $f / f_I < 0.75$, as the normalized frequency decreases, the indicators increase significantly. The voids in arch usually induce larger stress and deformation than that in crown with the same size. As the location angle and sector angle increase, the stress indicators increase

and the first peak frequency decreases.

In cases VD-L0-2~4 and VD-L60-2~4 in which the void depth is no less than 0.4 m, the changes of stress indicators and the first peak frequency are located within a limited range. Therefore, the void depth could be considered as a secondary influencing parameter in most cases. However, in the cases VD-L0-1 and VD-L60-1, the significant increase in stress can be induced due to the steep decrease of lining thickness, as marked by red circles in Figs. 6.15abd.

These limited numerical case studies suggest the first peak frequency descending can be considered to be intimately linked with the stress indicators. In order to get more accurate results, a preliminary investment is necessary to acquire the tunnel information such as lining concrete type. The void location and size can be considered as the key parameters changing stress state of the tunnel lining in most cases. More in-situ measurements are necessary to enhance the reliability and applicability of this method.

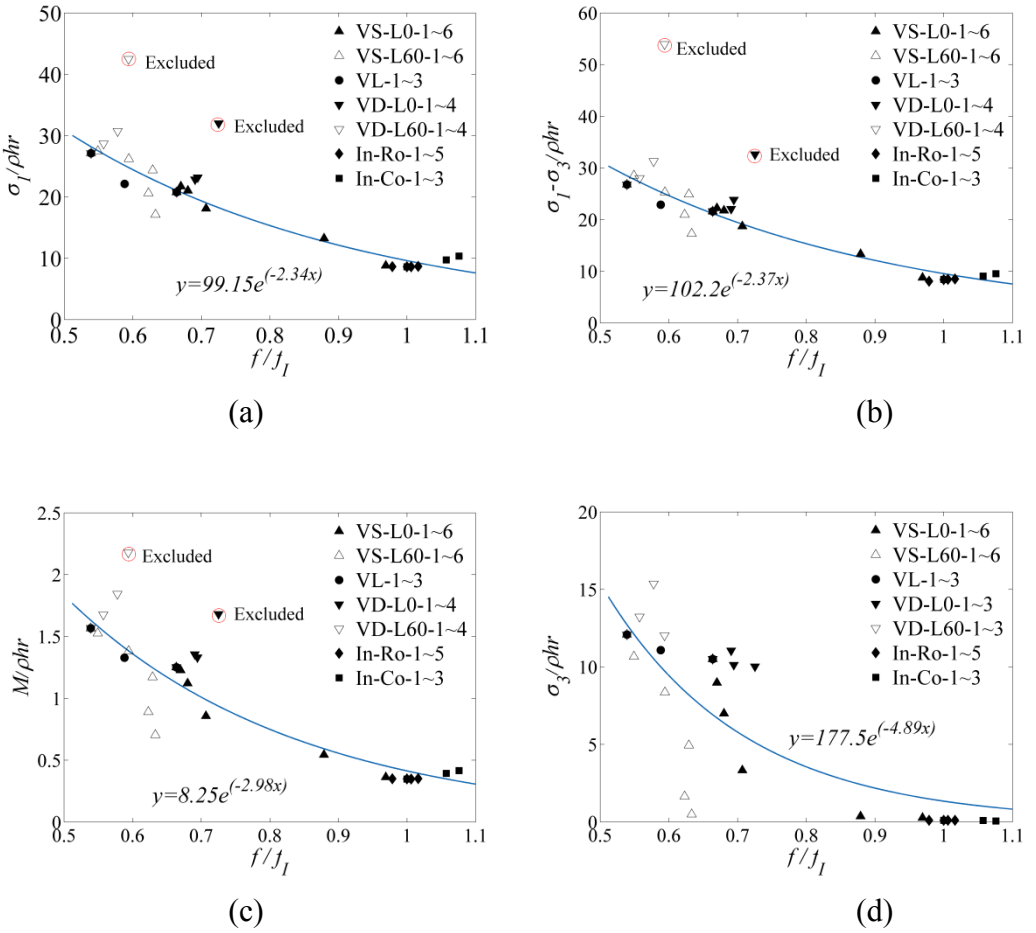

Fig. 6.15 Evaluated results of lining safety state based on the first peak frequency (ρ is the unit weight of the ground material, h is the overburden depth and r is the tunnel radius). (a) The maximum principal stress (determination coefficient = 0.91). (b) The difference between the maximum and minimum principal stress (determination coefficient = 0.91). (c) The maximum bending moment (determination coefficient = 0.85). (d) The minimum principal stress (determination coefficient = 0.66).

6.7 Numerical simulations of the model with cracks

The repeated and extreme loadings of surrounding rock mass and the degradation of lining also cause cracks, which introduce a local flexibility and affect the lining vibration response. A series of axial cracks located at the arch and crown of tunnel lining where cracks usually exist according to in-situ survey were simulated. A schematic view showing the parameters defining the status of axial cracks is presented in Fig. 6.16, and the parameters of different cases are listed in Table 6.6. Coulomb slip model were adopted to represent the mechanical behavior of cracks.

The influence of void location defined by angle θ was analyzed by using the cases VL-1, VL-2 and VL-3 with a normal stiffness of 20 GPa/m and a shear stiffness of 2 GPa/m. Their power spectra are shown in Fig. 6.17, peak frequencies are listed in Table 6.6 and the corresponding mode shapes are shown in Fig. 618. In each case, three frequency peaks (listed in Table 6.6) can be identified, and the peak frequencies in the three cases are almost the same (variations < 1 Hz). Meanwhile, the identified natural frequencies are also similar with those of the healthy span as shown in Fig. 6.3.

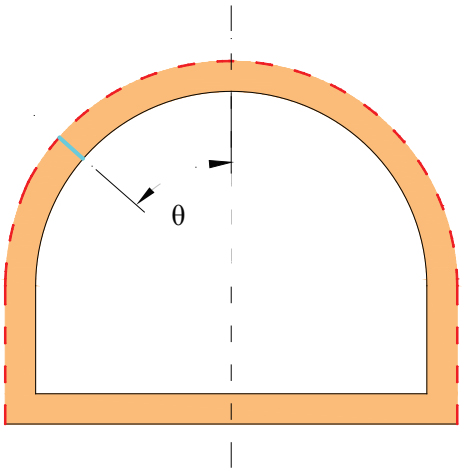

Fig. 6.16 Schematic view of an axial crack in the tunnel lining. Crack location: angle θ (CL).

Table 6.6 Values of crack parameters for different cases. Crack location: angle θ (CL); Crack stiffness: normal stiffness and shear stiffness (CN).

Case	θ (°)	Normal stiffness (GPa/m)	Shear stiffness (GPa/m)	Peak frequencies (Hz)
CL-1	0	20	2	46.2, 68.6, 80.1
CL-2	30	20	2	46.9, 69.9, 80.1
CL-3	60	20	2	46.2, 69.9, 80.1
CN-1-10	0	200	20	48.0, 70.4, 80.1
CN-2-10	0	20	2	46.2, 69.9, 80.1
CN-3-100	0	20	0.2	46.2, 70.2, 80.1

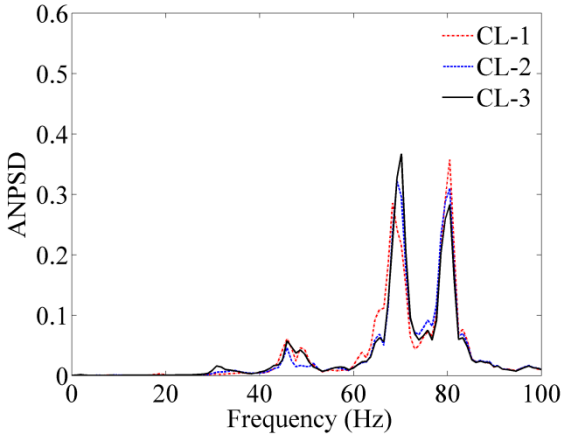

Fig. 6.17 The power spectrum of tunnel lining corresponding to different crack locations (θ).

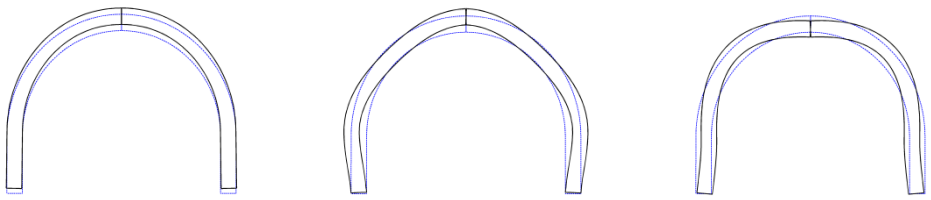

(a) (b) (c)

Fig. 6.18 The mode shapes of tunnel lining incase CL-1. (a) 46.2 Hz . (b) 68.6 Hz. (c) 80.1 Hz.

A group of axial cracks with different stiffness were simulated and their mechanical properties are listed in Table 6.6. The power spectra of obtained vibration histories in cases CN-1-10, CN-2-10 and CN-3-100 were calculated to find the peak frequencies, as shown in Fig. 6.19. With the increment of the normal stiffness of cracks, the first peak frequency increases while the almost no variation are induced in high modes.

These results indicate that influences of the axial crack on the frequency response are not as obvious as that of voids, and the axial crack can hardly be identified based on the frequency response. The void exists behind a tunnel lining causes significant increases in compressive stress on the outer surface and tensile stress on the inner surface, usually resulting in the crack generation and propagation in the lining and increasing the complex of the vibration problem. A further study will be carried out the influence of the crack propagation induced by the voids.

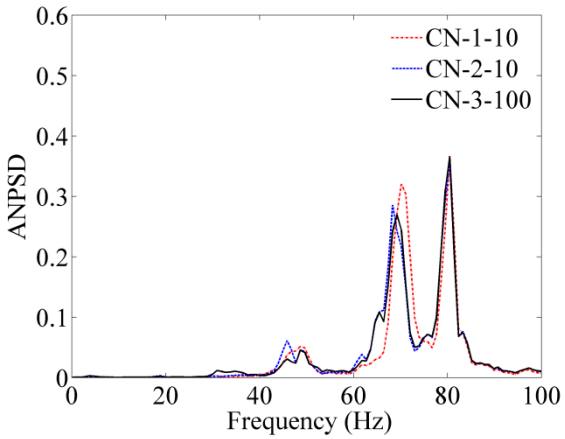

Fig. 6.19 The power spectra of tunnel lining corresponding to different normal and/or shear stiffness of concrete-rock interface in cases CN-1-10, CN-2-10 and CN-3-100.

6.8 Summary

This chapter presented a simple technique for the void identification of tunnel lining, through both in-situ measurements and numerical simulations of the microtremor characteristics of an aged mountain tunnel. By using the average of normalized power spectrum density (ANPSD) of microtremor, the peak frequencies of concrete lining in this tunnel were identified and the stress state of tunnel lining was evaluated based on the variation of first peak frequency. The following conclusions are drawn from this study.

(1) The voids between the tunnel lining and the rock mass induced the decrease of the first peak frequency, and the additional frequency peaks occurred when the void was not located on the central axis. The decrease of the first peak frequency was found to be dependent mainly on the void size and location. The larger the void size and location angle, the larger the decrease of the first peak frequency.

(2) The discontinuous contact between rockmass and lining concrete can be simplified as weak interfaces with low stiffness, which can be considered as an elastic supporting system during the dynamic calculation, and the normal stiffness of this weak interface can be estimated from the measured peak frequency.

(3) As the concrete stiffness decreases, the peak frequencies also decrease gradually and the peak frequencies in higher mode are more sensitive to the changes of lining stiffness. In the case of unweathered rock, the elastic modulus of rock has no obvious influence on the peak frequencies, while in the case of weathered rock, the peak frequency decreases slightly with the decrease of elastic modulus, and the identification of the peak frequencies become difficult due to the appearance of several small frequency peaks.

(4) The first peak frequency variation can be considered to be intimately linked with the stress state. Except for the cases with extremely small void depth, the void location and size are key parameters changing the stress state of the tunnel lining.

(5) Influences of the axial crack on the frequency response are not as obvious as that of voids, and the axial crack can hardly be identified based on the frequency response.

CHAPTER 7

Voids delineation behind tunnel lining based on the vibration intensity of microtremors

7.1 Introduction

Voids between concrete linings and rock masses, either produced during construction by outdated construction methods (e.g., fore-piling method) or generated along with the degradation of rock masses and lining concrete, are unfavorable to the stability of the supporting system and may invoke lining structure failures, such as water leakage, reinforcement corrosion and cracking. With the age-cold method of voids inspection, the lining voids can be identified by tapping the lining surface with the hammer and listening to the hollow drum sound. As impact-generated vibrations reflect between the lining and void surfaces, lining concrete where the voids exist resonates weakly and produces airborne sound through seismic-acoustic wave conversion. It provides a possible approach for the void detection if the measured seismic waves could be digitized and quantified. The propagation process of microtremors is significantly affected by the internal structure of materials, which can be used to detect flaws existing in materials and to assess the integrity of structures.

In this chapter, Vibration intensity ratio of the measured microtremors on three spans of Satomi tunnel was analyzed based on the mean value of the power spectrum density. Dynamic numerical simulations based on the features of these spans were performed by using the DEM to investigate the vibration intensity behavior of tunnel lining. Influences of the properties of rock-concrete interfaces, the voids and their geometrical parameters, and the mechanical properties of rock and concrete on the vibration response of tunnel linings were studied.

7.2 Vibration intensity analysis of in-situ microtremor on the tunnel lining

The microtremor measurements were carried out on the Satomi tunnel as mentioned in Chapter 5. Accelerometers were installed to measure the microtremors on the lining surface in each span. Three components of the microtremors in the vertical, horizontal and axial directions were measured, and then the microtremors in the radial and circumferential orientations of the tunnel were calculated through the vector conversion, as shown in Fig. 7.1.

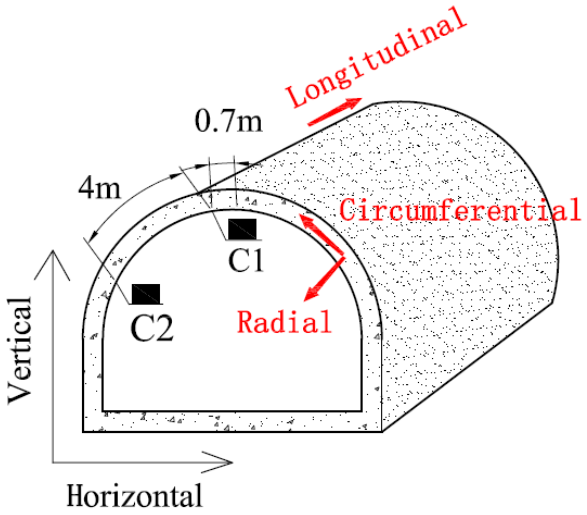

Fig. 7.1 Accelerometer configurations and vector conversions in field tests.

The predominant frequency can be obtained from the PSD given by Eq. 5.1, and the frequency-domain spectra of measured microtremors are plotted in Figs. 5.7 ~ 5.15. The frequency spectra show different characteristics at the low-frequency range (0-100 Hz) and the high-frequency range (100-500 Hz). The predominant frequencies of measured lining concrete are located in the low-frequency range, which can be measured accurately by the accelerometer used in this study. The high-frequency range mainly consists of some high-frequency noises mainly produced by the measurement system itself. Therefore, in this study, only the frequency spectrums in the range of 0-100 Hz were analyzed.

Because there are no external normal and shear stresses acting on the boundary of a void inside of a tunnel lining, the free oscillations or resonance, and the reflection and diffraction of waves may happen on the boundary. Between the damage part (e.g., voids) in the lining and the lining surface, the waves could be multiply reflected thus changing the vibrations on the lining surface. Due to the existence of the void-induced discontinuities, the spreading of stress wave energy is interfered, entrapping the energy within the concrete lining. Therefore, analyzing the vibration intensity can help detect the defects existing inside of the lining concrete.

The mean values of PSD in the low-frequency range 0-100 Hz, *P*, for the three spans

were calculated respectively to analyze their different characteristics of wave amplitudes by

$$P^{D} = E\left(\sum_{f=i}^{j} P(f)\right) \tag{7.1}$$

where *E()* indicates the mean value of a set of data, *P* are the power spectra density and the superscript *D* denotes the direction of the tunnel (*D=R* denotes the radial direction, *D=C* denotes the circumferential direction and *D=A* denotes the axial direction, as shown in Fig. 7.1).

Since the amplitudes of measured microtremors are very small, they can be easily affected by other unexpected vibration sources (e.g., nearby traffic loads). Therefore, it is worthless to directly compare the P^D values among the three spans. Meanwhile, the voids existing in tunnel lining have different spatial distributions, which can induce different vibration intensities in different directions. At here, the PSD ratio (RPSD) between different orientations as follows was proposed to diminish the influences of vibration sources.

$$RPSD^{Di/Dj} = P^{Di} / P^{Dj} \tag{7.2}$$

where *(i, j)* is the combination of the radial (*R*), circumferential *(C)* and axial *(A)* directions (see Fig. 7.1). For example, (*i = A, j = R*) denotes the ratio of P^A to P^R. Since PSD represents the vibration intensity, $RPSD^{Di/Dj}$ denotes the comparative vibration intensities between different orientations. The voids existing in tunnel lining have different spatial distributions, which can induce different vibration intensities in different orientations. Therefore, $RPSD^{Di/Dj}$ can be used as an indicator of the damage status (i.e. damage pattern, damage degree) of the lining.

For the convinience of analysis, $RPSD^{Di/Dj}$ was normalized by the following equation for the three spans.

$$RPSD^{Di/Dj} = \ln\left(\left(RPSD^{Di/Dj}\right)_d / \left(RPSD^{Di/Dj}\right)_u\right) \tag{7.3}$$

where the subscript d means the damaged span (S1 and S2), u means the undamaged span. The normalized $RPSD^{Di/Dj}$ of the undamaged span S3 in different directions

therefore become 0. A $RPSD^{Di/Dj}$ with positive value means that a relatively larger vibration intensity of damaged span is induced in the i direction, compared with the undamaged span. On the contrary, a $RPSD^{Di/Dj}$ with negative value means that a larger vibration intensity is induced in the *j* direction.

The RPSD values of the in-situ microtremor measurements are plotted in Fig. 7.2. In the damaged span S1 (Fig. 5.3 (a)), the RPSD values of C1, in which voids and cracks exist, are obviously smaller than 0 especially for $RPSD^{C/R}$ (smaller than -2.0). The RPSD values of C2 in both S1 and S2 (Fig. 5.3 (b)), where only surface cracks exist, are larger or smaller than 0 in varying degrees. The RPSD values of C1 in S2, where no cracks or voids exist, are almost equal to 0.

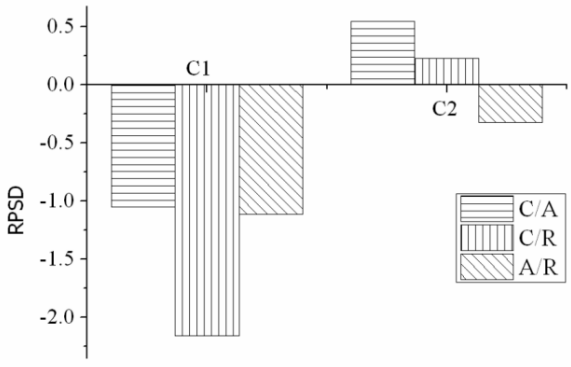

(a)

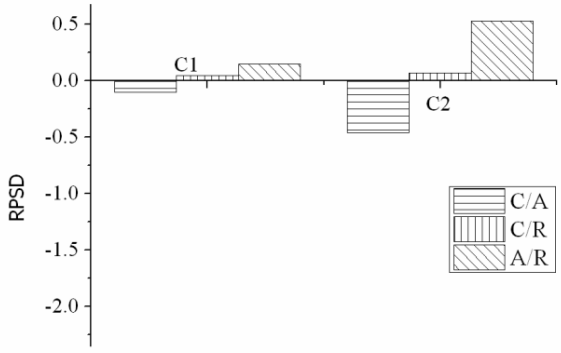

(b)

Fig. 7.2 RPSD values of the in-situ microtremor measurements. (a) S1 span. (b) S2 span

The cracks may open and close depending on the loading conditions and vibration amplitude, and affect the vibration characters of tunnel lining (Chondros, 2001). The surface cracks induce a moderate variation of RPSD in different orientations and the variation shows different characteristics with that induced by voids, by comparing Fig. 5.3(a) with Fig. 5.3 (b). The absolute values of changes induced by the cracks are no more than 0.5 (C2 in S1 and S2) and are not as obvious as that induced by the voids (the absolute values of RPSD of C1 in S1 are larger than 1). These results indicate that the voids change the PSD features greatly and can be effectively detected by the proposed indicator, regardless of the existence of cracks.

7.3 Vibration intensity of Numerical simulations

7.3.1 Numerical model for simulations

The actual interaction between the concrete and the surrounding rock mass of a tunnel is difficult to be accurately represented by a numerical model due to the heterogeneity and anisotropy of the rock mass and the existence of incomplete contacts (Holmgren, 1979; Stille, 1992; Malmgren, 2001; Stacey, 2002). In the numerical simulations, it was simplified to weak concrete-rock interfaces with small values of normal and shear stiffness. The Mohr-Coulomb model and the Coulomb slip model were adopted to represent the mechanical behavior of rock mass and concrete lining, and rock-concrete interface, respectively. Their physico-mechanical properties are tabulated in Table 6.1 in Chapter 6. The size of the numerical model is in accordance with the tested tunnel, as shown in Fig. 7.3. Since this is a two-dimensional model, only the vibration histories in vertical and horizontal directions were recorded. Stress equivalent to an overburden of 35 m was applied on the upper boundary of the model. In order to investigate the influences of voids on the microtremor behavior, a series of models with/without simplified elliptic voids located at the arch and crown of tunnel lining were established and simulated, as shown in Fig 6.5 in Chapter 6, and the void parameters adopted in different cases are tabulated in Table 6.3.

A static equilibrium was achieved before the start of dynamic simulation. The seismic wave sources were assumed to be far-field that could be input into the model on the

boundaries as simplified plane waves. However, in in-situ measurements, it is difficult to record the real vibration histories at the locations corresponding to the boundaries of the numerical models. As an alternative, the microtremors measured at the point C1 of S3 span were chosen as vibration sources and were input on the bottom boundary of the model. It was assumed that the microtremors at different locations in the lining of a tunnel are induced by the waves with similar propagation direction. The Rayleigh damping with a ratio of 1% was utilized during dynamic calculations to represent the attenuation of materials. The boundaries of model were set as viscous boundaries to absorb the propagating stress waves passing by and to minimize wave reflections at boundaries. 32768 discrete time signals at each monitoring point were recorded during numerical simulations with a sampling interval of 0.001 s. An element size of 0.2 m was adopted in the numerical models.

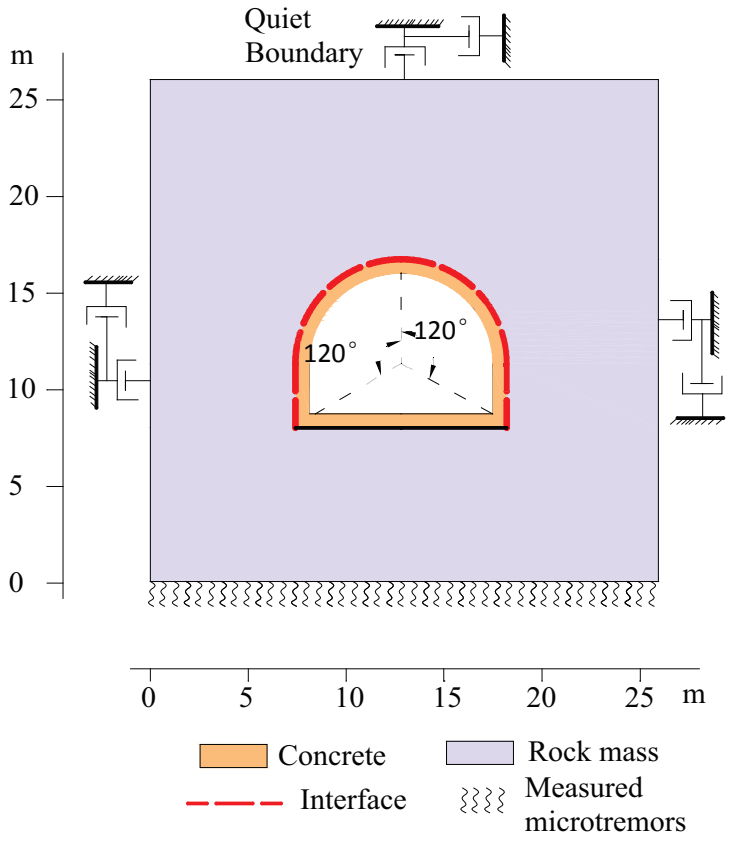

Fig. 7.3 Model of numerical simulation.

7.3.2 Influence of the concrete-rock interface

The concrete-rock interface has a great influence on the vibration characters of a structure. Especially for the tunnels built by the conventional methods without using shotcrete, incomplete contacts usually exist between rock mass and concrete, resulting in the remarkable decrease of concrete-rock interface stiffness.

A group of rock-concrete interfaces with different stiffness based on case VL-1 were simulated and their mechanical properties are tabulated in Table 7.1, including different combinations of the values of normal and/or shear stiffness. The calculated $RPSD^{C/R}$ is shown in Fig. 7.4. When the normal stiffness is relatively high (cases J-3-10, J-4-10 and J-4-100), the $RPSD^{C/R}$ at the locations where the void exists have negative values with the minimum on the center of the void. The minimum moves to the both sides of the void in the cases with low normal stiffness (cases J-1-10 and J-2-10). Especially for the case J-1-10 of which the normal stiffness is 0.1 GPa/m, the minimum occurs at the locations with arc angle of about 30° away from the void, undermining the clear detection of the void location based on the $RPSD^{C/R}$. As the shear stiffness decreases (cases J-4-10 and J-4-100), the minimum also decreases even though the variation is not as obvious as that in normal stiffness.

In these cases, large intensity radial vibration on the top of the void is evoked ($RPSD^{C/R} < 0$), which allowed the void delineation based on the minimum $RPSD^{C/R}$ in the condition of large normal stiffness. Laboratory testing results on shotcrete-rock joints conducted by Saiang (2005) showed that the mechanical properties of interface have similar values with those of the case J-4-100, which were therefore adopted in the following simulations.

Table 7.1. Material properties of rock-concrete interface used in the numerical simulations.

Cases	Normal stiffness (GPa/m)	Shear stiffness (MPa/m)
J-1-10	0.1	0.01
J-2-10	1	0.1
J-3-10	10	1
J-4-10	100	10
J-4-100	100	1

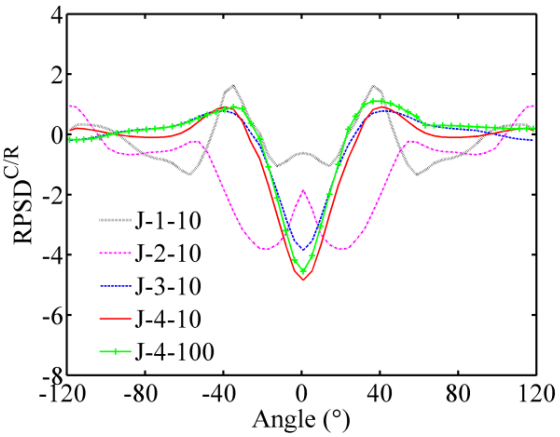

Fig. 7.4 Influence of the stiffness of the concrete-rock interface on $RPSD^{C/R}$.

7.3.3 Influence of void location (angle θ)

The influence of void location defined by angle θ was analyzed by using the cases VL-1, VL-2 and VL-3 with a void depth of 0.6 m and a sector angle of 60° (listed in Table 7.3). The calculated $RPSD^{C/R}$ of tunnel lining is shown in Fig. 7.5.

In these cases, the $RPSD^{C/R}$ at the void location has negative values. This indicates that the existence of the void leads to the increase of the vibration intensity in the radial direction, caused by the repeated multiple wave reflections between the tunnel wall and the void surface. The minimum values (-4.84 in case VL-1, -6.174 in case VL-2 and -5.45 in case VL-3) occur on the center of the void and vary in a small range with the change of the void location. It reveals that the minimum of $RPSD^{C/R}$ always exists on the center of the void and its position shifts along with the void location.

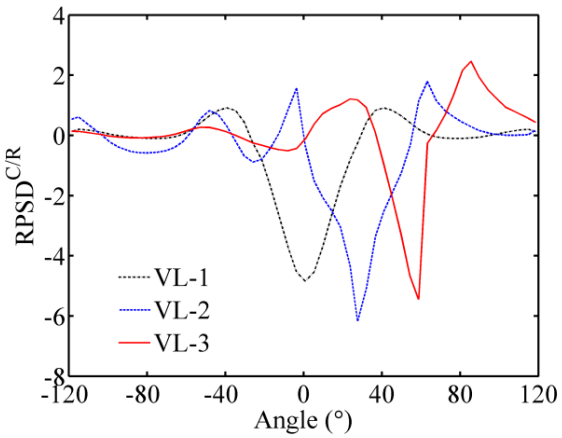

Fig. 7.5 Influence of the void location on $RPSD^{C/R}$.

7.3.4 Influence of the void arc length (sector angle γ)

The influence of void arc length defined by sector angle γ was analyzed using the cases with different void arc lengths but equivalent void depth of 0.6 m and void location of 0° (cases VS-L0-1 ~ VS-L0-6). The calculated $RPSD^{C/R}$ is shown in Fig. 7.6.

As the sector angle increases, the value of $RPSD^{C/R}$ at the void location decreases. When the sector angle γ = 10° (cases VS-L0-1) the $RPSD^{C/R}$ of the whole tunnel lining approaches zero, revealing that void with such size could hardly be identified. The values of $RPSD^{C/R}$ at the void location are obvious less than zero in the cases VS-L0-3 ~ 6 and the void could be delineated based on the negative $RPSD^{C/R}$ values.

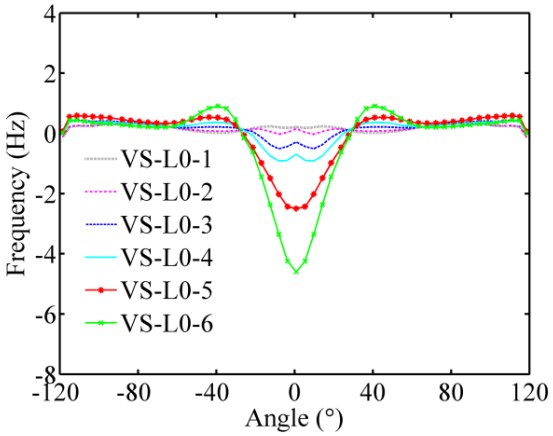

Fig. 7.6 Influence of the void arc length on $RPSD^{C/R}$.

7.3.5 Influence of void depth *h*

The influence of void depth was analyzed by using the cases with different void depths (cases VD-L0-1, VD-L0-2, VD-L0-3 and VD-L0-4). The calculated $RPSD^{C/R}$ is shown in Fig. 7.7.

The existence of the void usually reduces the thickness of the lining, rendering a considerable reduction in the lining resistance and a larger radial vibration. As shown in Fig. 7.7, the value of $RPSD^{C/R}$ at the void location increases gradually with the decrease of the void depth *h*. Especially in the case VD-L0-1 with the lining thickness of 20 cm, the thin lining shell results in a significant reduction in the minimum value of $RPSD^{C/R}$.

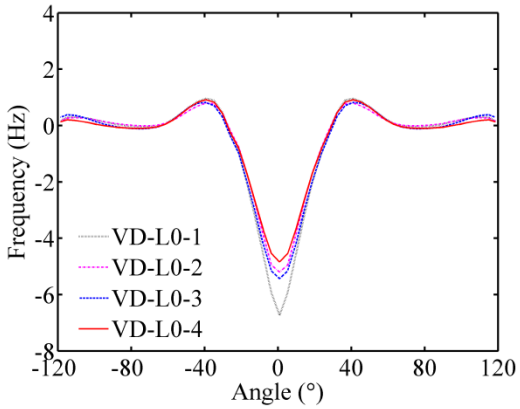

Fig. 7.7 Influence of the void depth on $RPSD^{C/R}$.

7.3.6 Influence of lining concrete type

The properties of three typical types of concrete that are commonly used in tunnel lining constructions with different mechanical properties are tabulated in Table 6.4. The variation of elastic modulus also causes changes in the $RPSD^{C/R}$ of tunnel lining, as demonstrated in Fig. 7.8. As the elastic modulus decreases (i.e. from C50 to C20), the value of $RPSD^{C/R}$ at the void location decreases gradually, revealing that larger vibrations are much easier to be excited in the concrete with lower stiffness.

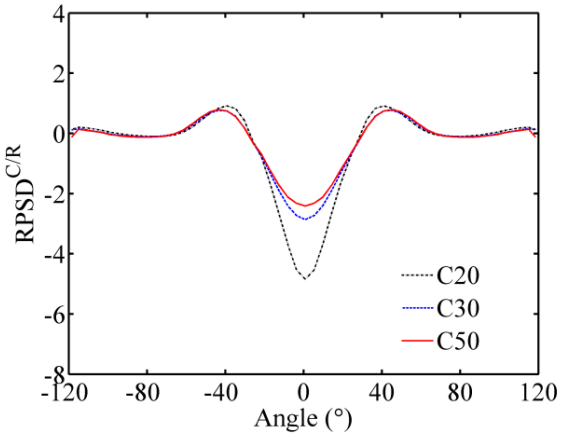

Fig. 7.8 Influence of the concrete type on $RPSD^{C/R}$.

7.3.7 Influence of rock type

Besides the rock-concrete interface and concrete lining, the surrounding rock mass remains as another key factor affecting the dynamic properties of the tunnel system. The properties of typical types of rocks are tabulated in Table 6.5 and the valued of $RPSD^{C/R}$ of tunnel lining supporting different rock types are shown in Fig. 7.9.

In four cases, similar negative peak values of $RPSD^{C/R}$ exist at the center of the void. In the case of weathered rock, the value of $RPSD^{C/R}$ fluctuates around 0. Except the case of the weathered rock, the $RPSD^{C/R}$ of tunnel lining have similar variation around the void, especially in the medium and the hard rock that have the larger elastic modulus. The soft rock, of which the acoustic impedance is the closest to that of the lining concrete, has the minimum negative peak value of $RPSD^{C/R}$. These results indicate the $RPSD^{C/R}$ is an effective indicator for the void delineation regardless of the rock type and has the potential to be widely used in various geological conditions.

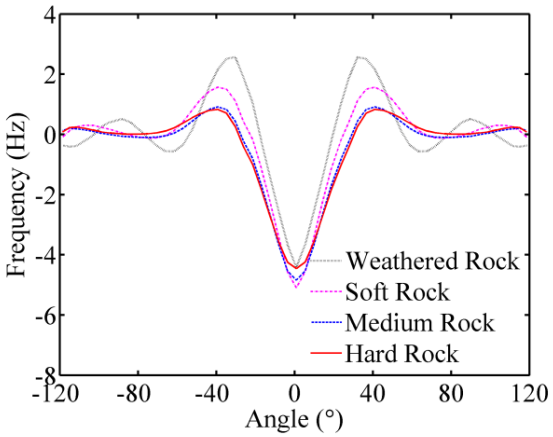

Fig. 7.9 Influence of the rock type on $RPSD^{C/R}$.

7.4 Influence of axial cracks

The influences of axial cracks defined by location angle θ and by stiffness were analyzed by using the cases listed in Table 6.6 and the calculated $RPSD^{C/R}$ on the surface of tunnel lining is shown in Figs. 7.10ab.

In these cases, all the $RPSD^{C/R}$ values are around 0. As the location angle changes, few variations are invoked (the maximum of variations < 0.2). The normal and shear stiffness of axial cracks invoke almost no variations of $RPSD^{C/R}$, as shown in Fig. 7.9b. Compared with the voids, the axial cracks have the much fewer influences on the vibration intensity, which agrees with the in-situ measurements although their absolute values are not equal. It indicates that axial cracks could hardly be identified. A detailed study about the crack propagation in tunnel lining should be carried out.

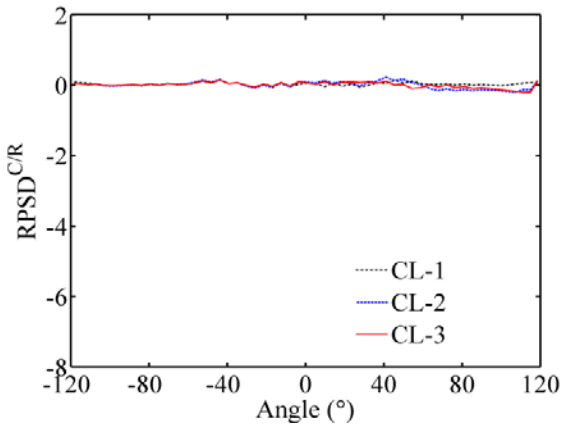

(a)

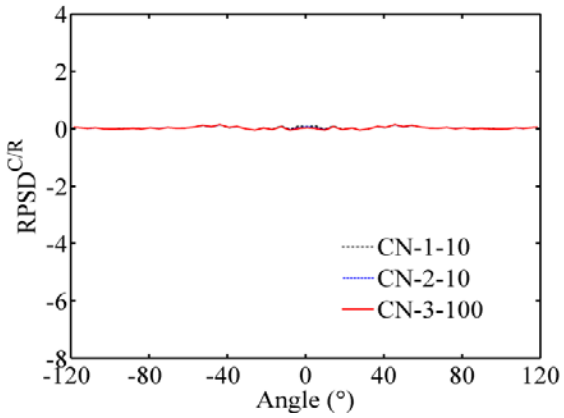

(b)

Fig. 7.10 Influence of of axial crack on $RPSD^{C/R}$. (a) The location angle θ. (b) The normal and shear stiffness.

7.5 Summary

This chapter presented a simple technique for the void delineation of tunnel lining, through both in-situ measurements and numerical simulations of the microtremor characteristics of an aged tunnel. By using the ratio of vibration intensity of microtremors in different directions, the void behind the tunnel lining can be delineated. The influences of the rock-concrete interface, the void and its parameters (location, size and depth), rock type and concrete type on the RPSD were also numerically investigated and were compared with in-situ measurements. The following conclusions are drawn from this study.

(1) In both field measurements and numerical simulations, the indicator RPSD, which is the normalized ratio of the ratio of PSD at different direction (i.e. C/R) of undamaged span to damaged span, has shown good performance in detecting the void. For the region where the void exists, the RPSD values are smaller than 0 and the negative peak (the minimum) occurs on the center of the void. The $RPSD^{C/R}$ of the region where the void is located decreases gradually with the decrement of the void depth and the increment of the void arc length. The void could hardly be identified when the sector angle $\gamma < 20°$.

(2) The interaction between rock mass and lining concrete is simplified as interfaces with normal and shear stiffness, which can be considered as an elastic supporting system during the dynamic calculation. Compared to the shear stiffness, the normal stiffness causes much larger changes on the RPSD values.

(3) As the concrete stiffness decreases, $RPSD^{C/R}$ of the region where the void is located also decrease gradually. The $RPSD^{C/R}$ affected by the void is more sensitive to in the lining with low stiffness.

(4) The rock with the similar acoustic impedance of the lining concrete has the minimum R$PSD^{C/R}$ negative peak and the $RPSD^{C/R}$ is an effective indicator for the void regardless of the rock type.

CHAPTER 8

Conclusions and discussions

8.1 Conslusions

Notwithstanding how well a tunnel is constructed, it still require the health assessment ot determine the condition of the lining after a long time service. So far, many health assessment techniques have been proposed to identify defects in the aged tunnel lining. However, these techniques usually depend on the experiences of the operator for data interpretation and cannot be continued with the decrease of labor force and the increase of engineering quantities. This thesis presented a simple technique for the health assessment of tunnel lining, through theoretical analysis, in-situ measurements and numerical simulations of the vibration characteristics of an aged mountain tunnel. Based on the microtremor measurement of tunnel lining, the void, which usually induces serious damages on tunnel linings, can be identified based on its frequency response and the vibration intensity. The stress state of tunnel lining around the void can also be estimated based on the first natural frequency. Hence, the healthy state of tunnel lining can be evaluated. The main conclusions about this study are summarized in this chapter.

In Chapter 2, three types of widely used non-destructive health assessment techniques (Optical technique, electromagnetic technique and mechanical oscillation technique) were introduced firstly. Visual inspection and infrared thermography techniques have low cost and easy operations, while it has the limitation of penetration depth and is influenced by the coating or installation on the surface of tunnel lining. Impact-echo technique is effective for detecting defect interface in the lining concrete, while additional calibration is necessary and interpretation of data is very slow. The Ground Penetrate Radar (GPR) has a wide range of application, while it is limited by the conductive environment (such as steel reinforcement, water). Meanwhile, these techniques all depend on the experiences of the operator for data interpretation and cannot be continued with the decrease of labor force and the increase of engineering quantities.

In Chapter 3, the EDEM based on the DEM code of UDEC is further developed and is applied to investigate the natural frequency of reinforcement concrete beam under loading. The tensile-shear failure criterion adopted by Jiang et al. (2009) has been

implanted into the framework of EDEM to determine the initiation and propagation of 2-D cracks and to analyze the failure patterns of RC beam. The displacement-loading curve and the failure status of the EDEM simulations agree well with the experimental tests. In both EDEM simulations and the experiments, similar variation of natural frequency can also be concluded that: the cracking process in the RC beam, that decreases its rigidity, can be identified based on the continuously descending of the natural frequency.

In Chapter 4, the natural frequencies of tunnel lining shell with the supporting of elastic rock-concrete interfaces were analyzed based on the Love-Timoshenko shell theory and Donnell-Mushtari shell theory. When $n \geq 1$, the nature frequency estimated by Love theory is slight smaller than that of Donnell theory due to the neglecting of the tangential displacements and their derivatives. The relative error among the methods used in this paper is small in low frequency modes and increases with the increment of h/R. The natural frequencies decrease with the increment of the void size and the significant influence of the void size exists in the first order frequency. The first order natural frequency can be estimated accurately. The elastic rock-concrete interface has a great influence on natural frequencies of the tunnel lining. For $n \geq 1$, the nature frequencies are mainly affected by the normal stiffness. The interface stiffness has the largest influence on low nature frequencies in vibration modes of $n = 1, 2, 3$.

In Chapter 5 and 6, the microtremor characteristics were analyzed by both the in-situ experiments and the numerical simulations. Firstly, the microtremors were measured on three spans of a road tunnel with varying damage degrees. The modal parameters including natural frequencies and damping ratio were extracted with the peak picking methods. In the healthy span S3 and moderate damaged span S2 (one axial crack) the identified peak frequencies are similar, while in seriously damaged span S1 (voids and cracks) multiple frequency peaks with the lowest peak frequency 32.2 Hz occur. As the span healthy worsens, the damping ratio increases. However, damping ratios couldn't be indentified in some cases because of heavily damped and the closely spaced modes. And then, numerical simulations were carried out based on the physico-mechanical properties of the surrounding rock mass and lining concrete in accordance with the tested tunnel.

The influences of voids on natural frequency that voids induced the decrease of the first peak frequency and the additional frequency peaks were verified. The decrease of the first peak frequency was found to be dependent mainly on the void size and location, and the larger the void size and location angle, the larger the decrease of the first peak frequency. As the concrete stiffness decreases, the peak frequencies also decrease gradually and the peak frequencies in higher mode are more sensitive to the changes of lining stiffness. In the case of unweathered rock, the elastic modulus of rock has no obvious influence on the peak frequencies, while in the case of weathered rock, the peak frequency decreases slightly with the decrease of elastic modulus, and the identification of the peak frequencies become difficult due to the appearance of several small frequency peaks. The first peak frequency variation can be considered to be intimately linked with the stress state. Except for the cases with extremely small void depth, the void location and size are key parameters changing the stress state of the tunnel lining.

In Chapter 7, the void behind the tunnel lining was delineated by using the ratio of vibration intensity of microtremos in different directions. In both field measurements and numerical simulations, the RPSD values are smaller than 0 on the region where the void exists and the negative peak (the minimum) occurs on the center of the void. The $RPSD^{C/R}$ of the region where the void is located decreases gradually with the decrement of the void depth and the increment of the void arc length. The void could hardly be identified when the sector angle $\gamma < 20°$. Compared to the shear stiffness, the normal stiffness causes much larger changes on the RPSD values. Except for the cases with low normal stiffness (no larger than 1 GMp/m), the void can be identified based on the RPSD. As the concrete stiffness decreases, $RPSD^{C/R}$ of the region where the void is located also decrease gradually. The $RPSD^{C/R}$ affected by the void is more sensitive to in the lining with low stiffness. The rock with the similar acoustic impedance of the lining concrete has the minimum $RPSD^{C/R}$ negative peak and the $RPSD^{C/R}$ is an effective indicator for the void regardless of the rock type.

8.2 Future study

The microtremor analysis method presented in this study only needs to measure the acceleration waves on the surface of tunnel lining, which is convenient for application, low in cost, and bringing negligible damage to the lining concrete. During the in-situ microtremor measurements, three points (one on crown, and other two on the arch of each side) are recommended in order to obtain the frequency information of the whole span. The peak frequency can be identified easily from the measured microtremors.

Voids, usually existing between concrete linings and rock masses, change the lining stress state that the lining undergoes inner compression on the surface and tension on the outer surface and invoke lining structure cracking which could involve the serious risks for the tunnel safety. A further study concerning the influence of crack initiation and propagation induced by voids on frequency response is very necessary.

More in-situ measurements are also needed to extend this method for future engineering practices and to give more comprehensive assessment of the microtremor dynamic properties of tunnel linings.

REFERENCE

Abraham O, Dérobert X. Non-destructive testing of fired tunnel walls: the Mont-Blanc Tunnel case study[J]. NDT & E International, 2003, 36(6): 411-418.

Adams A K, Gill A S, Ek J R, et al. Contribution of conduction to total infant energy expenditure[J]. Journal of thermal biology, 1998, 23(5): 267-273.

Aktan A E, Catbas F N, Grimmelsman K A, et al. Issues in infrastructure health monitoring for management[J]. Journal of Engineering Mechanics, 2000, 126(7): 711-724.

Annan A P, Cosway S W, DeSouza T. Application of GPR to map concrete to delineate embedded structural elements and defects[C]//Proceedings Of Ninth International Conference on Ground Penetrating Radar (GPR2002). International Society for Optics and Photonics, 2002: 359-364.

Armenàkas A E, Gazis D C, Herrmann G. Free vibrations of circular cylindrical shells[R]. Northwestern Univ Evanston Il Dept of Civil Engineering, 1969.

Asakura T, Kojima Y. Tunnel maintenance in Japan[J]. Tunnelling and Underground Space Technology, 2003, 18(2): 161-169.

Mrad R B, Fassois S D, Levitt J A. A polynomial-algebraic method for non-stationary TARMA signal analysis-Part I: The method[J]. Signal Processing, 1998, 65(1): 1-19.

Balendra T, Thambiratnam D P, Koh C G, et al. Dynamic response of twin circular tunnels due to incident SH‐waves[J]. Earthquake engineering & structural dynamics, 1984, 12(2): 181-201.

Beskou N D, Theodorakopoulos D D. Dynamic effects of moving loads on road pavements: a review[J]. Soil Dynamics and Earthquake Engineering, 2011, 31(4): 547-567.

Bendat J S, Piersol A G. Random data: analysis and measurement procedures[M]. John Wiley & Sons, 2011.

Bendat J S, Piersol A G. Engineering applications of correlation and spectral analysis[J]. New York, Wiley-Interscience, 1980, 315 p.

Bouchard P O, Bay F, Chastel Y, et al. Crack propagation modelling using an advanced remeshing technique[J]. Computer methods in applied mechanics and engineering, 2000, 189(3): 723-742.

Brincker R, Zhang L, Andersen P. Modal identification of output-only systems using frequency domain decomposition[J]. Smart materials and structures, 2001, 10(3): 441.

Bhalla S, Yang Y W, Zhao J, et al. Structural health monitoring of underground facilities–technological issues and challenges[J]. Tunnelling and Underground Space Technology, 2005, 20(5): 487-500.

Bishop R E D and Johnson D C. Vibration analysis table[M], Cambridge University Press, 1956.

Bracewell R N. Fourier transform and its applications[M]. McGraw-Hill, New York, 1980.

Brownjohn J M W. Ambient vibration studies for system identification of tall buildings[J]. Earthquake engineering & structural dynamics, 2003, 32(1): 71-95.

Bungey J H. Sub-surface radar testing of concrete: a review[J]. Construction and Building materials, 2004, 18(1): 1-8.

Burnay S G, Williams T L. Applications of thermal imaging[M]. Taylor & Francis Group, 1988.

Can M. Simultaneous convective heat and mass transfer in impingement ink drying[J]. International communications in heat and mass transfer, 1998, 25(6): 863-874.

Carino N J, Sansalone M. Pulse-echo method for flaw detection in concrete[J]. Final Report National Bureau of Standards, Washington, DC. Center for Building Technology., 1984, 1.

Celebi M, Liu H P. Before and after retrofit–response of a building during ambient and strong motions[J]. Journal of Wind Engineering and Industrial Aerodynamics, 1998, 77: 259-268.

Chatelain J L, Gueguen P, Guillier B, et al. CityShark: A user-friendly instrument dedicated to ambient noise (microtremor) recording for site and building response studies[J]. Seismological Research Letters, 2000, 71(6): 698-703.

Cheng C C, Sansalone M. Effects on impact-echo signals caused by steel reinforcing bars and voids around bars[J]. ACI Materials Journal, 1993, 90(5).

Clinton J F. Modern digital seismology-instrumentation, and small amplitude studues in the engineering world[D]. California Institute of Technology, 2004.

Chowdhury M R. Experimental modal testing and analysis of continuously supported structures[C]. Proceedings of 8th Int'l Mod. Anal. Conf., Florida, 1990: 109-114.

Chondros T G, Dimarogonas A D, Yao J. A continuous cracked beam vibration theory[J]. Journal of Sound and Vibration, 1998, 215(1): 17-34.

Chondros T G, Dimarogonas A D, Yao J. Vibration of a beam with a breathing crack[J]. Journal of Sound and vibration, 2001, 239(1): 57-67.

Conforto S, D'alessio T. Spectral analysis for non-stationary signals from mechanical measurements: a parametric approach[J]. Mechanical Systems and Signal Processing, 1999, 13(3): 395-411.

Cooper J E, Worden K. On-line physical parameter estimation with adaptive forgetting factors[J]. Mechanical Systems and Signal Processing, 2000, 14(5): 705-730.

Cremer L, Heckl M, Petersson B A T. Structure-borne sound[J]. Physics Today, 1975, 28: 81.

Cubed A. General State of the Art Review of Ground Probing Radar[M].A-CUBED, Mississauga, Ontario, 1983.

Daniels D J. Ground Penetrating Radar. 2nd ed. IEE Radar, Sonar, Navigation and Avionics Series[M]. Institute of Electrical Engineers, London, 2004.

Davis A G. The non-destructive impulse response test in North America: 1985–2001[J]. NDT&E International (Elsevier Science), 2003. 36: 185–93.

Davis A G, Lim M K, Petersen C G. Rapid and economical evaluation of concrete tunnel linings with impulse response and impulse radar non-destructive methods[J]. NDT & E International, 2005, 38(3): 181-186.

Davis A G. The nondestructive impulse response test in North America: 1985–2001[J]. NDT & E International, 2003, 36(4): 185-193.

Davis A G, Lim M K, Petersen C G. Rapid and economical evaluation of concrete tunnel linings with impulse response and impulse radar non-destructive methods[J]. NDT & E International, 2005, 38(3): 181-186.

Davis C A, Lee V W, Bardet J P. Transverse response of underground cavities and pipes to incident SV waves[J]. Earthquake engineering & structural dynamics, 2001, 30(3): 383-410.

Diamanti N, Giannopoulos A, Forde M C. Numerical modelling and experimental verification of GPR to investigate ring separation in brick masonry arch bridges[J]. NDT & E International, 2008, 41(5): 354-363.

Doebling S W, Farrar C R, Prime M B, et al. Damage identification and health monitoring of structural and mechanical systems from changes in their vibration characteristics: a literature review[R]. Los Alamos National Lab., NM (United States), 1996.

Doebling S W, Farrar C R, Goodman R S. Effects of measurement statistics on the detection of damage in the Alamosa Canyon Bridge[C].Proceedings-spie The International Society For Optical Engineering. Spie International Society for Optical, 1997: 919-929.

Dondi G. Three-dimensional finite element analysis of a reinforced paved road[C].Proceedings of the fifth international conference on geotextiles, geomembranes and related products. 1994, 1: 95-100.

Donnelly L J, McCann D M. The location of abandoned mine workings using thermal techniques[J]. Engineering geology, 2000, 57(1): 39-52.

Donovan K, Pariseau W G, Cepak M. 1984, Finite element approach to cable bolting in steeply dipping VCR stopes[M]. In Geomechanics Application in Underground Hardrock Mining. Society of Mining Engineers, New York.

Drysdale D. An introduction to fire dynamics[M]. John Wiley & Sons, 2011.

Dunand F, Guéguen P , Bard P Y, Rodgers J, Celebi M. Comparaison of the dynamic behaviour extracted from weak, moderate and strong motion recorded in buildings[C]. In: Proceedings First European Conf. on Earthquake Engineering and Seismology, 3-8 September 2006, Geneva, Switzerland, paper#1021.

Eisenberger M, Efraim E. In‐plane vibrations of shear deformable curved beams[J]. International Journal for Numerical Methods in Engineering, 2001, 52(11): 1221-1234.

Engelbert P J, Hotchkiss R H, Kelly W E. Integrated remote sensing and geophysical techniques for locating canal seepage in Nebraska[J]. Journal of applied geophysics, 1997, 38(2): 143-154.

Farrar C R, Doebling S W, Cornwell P J, et al. Variability of modal parameters measured on the Alamosa Canyon Bridge[C]. Proceedings-spie The International Society For Optical Engineering. Spie International Society for Optical, 1997: 257-263.

Fuller C R. The effects of wall discontinuities on the propagation of flexural waves in cylindrical shells[J]. Journal of Sound and Vibration, 1981, 75(2): 207-228.

Braun S. Encyclopedia of vibration: FP[M]. Academic Press, 2002.

Forsberg K. Influence of boundary conditions on the modal characteristics of thin cylindrical shells[J]. AIAA journal, 1964, 2(12): 2150-2157.

Fotieva N N. Determination of the minimum seismically safe distance between two parallel tunnels[J]. Soil Mechanics and Foundation Engineering, 1980, 17(3): 111-116.

Fouskitakis G N, Fassois S D. On the estimation of nonstationary functional series TARMA models: An isomorphic matrix algebra based method[J]. Journal of dynamic systems, measurement, and control, 2001, 123(4): 601-610.

François S, Pyl L, Masoumi H R, et al. The influence of dynamic soil–structure interaction on traffic induced vibrations in buildings[J]. Soil Dynamics and Earthquake Engineering, 2007, 27(7): 655-674.

Gao Y, Jiang Y, Li B, et al. Study on microtremor spectrum properties of tunnel lining[C].. Renewable Energy Research and Applications (ICRERA), 2012 International Conference on. IEEE, 2012: 1-6.

Gao Y, Jiang Y, Li B. Estimation of effect of voids on frequency response of mountain tunnel lining based on microtremor method[J]. Tunnelling and Underground Space Technology, 2014, 42: 184-194.

Gersch W, Kitagawa G. A time varying AR coefficient model for modelling and simulating earthquake ground motion[J]. Earthquake engineering & structural dynamics, 1985, 13(2): 243-254.

Glazanov V E, Shenderov E L. Plane wave scattering by cylindrical cavity in isotropic elastic medium[J]. Soviet Physics Acoustics 17(1971):41–43.

Grundmann H. Dynamic interaction of structures with the subsoil[J]. Balkema Publishers, Structural Dynamics: EURODYN'99, 1999, 1: 31-41.

Haack A, Schreyer J, Jackel G. State-of-the-art of Non-destructive Testing Methods for Determining the State of a Tunnel Lining[J]. Tunnelling and Underground Space Technology incorporating Trenchless Technology Research, 1995, 10(4): 413-431.

Harari, A. Wave propagation in a cylindrical shell with joint discontinuity[J]. Shock and vibration Bulletin. 1978, 48, 53-61.

Hatanaka et al.,. Reinforced concrete structure design: Third Edition and theory [M], Tokyo, Morikita Publishing Co., 2010.

Hirose S. Boundary element modelling and analysis of moving loads in time and frequency domains[J]. Wave 2000/Wave Propagation, Moving Loads and Vibration Reduction, Balkema, 2000: 71-82.

Holmgren J. Punch-loaded shotcrete linings on hard rock–PhD Dissertation[J]. Royal Institute of Technology, Stockholm, Sweden, Swedish Rock Engineering Research Foundation–BeFo report, 1979 (7): 2.

Li B, Jiang Y, Tanabashi Y, et al. Behavior of large scale underground cavern located in jointed rock masses evaluated by using Distinct Element Method[J]. Soils and Foundations, 2010, 50(5): 609-621.

Ikeda Y, Suzuki Y, Suzuki Y, et al. Damage detection of actual building structures through singular value decomposition of power spectral density matrices of microtremor responses[J]. AIJ Journal of Technology and Design, 2010, 16(32): 69-74.

Itasca, UDEC - user's manual[M]. Minneapolis, MN: Itasca Consulting Group Inc. 2000.

JDP NEWS. Police begin office raids of collapsed Japanese tunnel operator [online]. Last accessed Dec 04, 2012 at: http://japandailypress.com/police-begin -office-raids- of-collapsed-japanese-tunnel-operator-0419253/.

Jaeger J C, Cook N G W, Zimmerman R. Fundamentals of rock mechanics[M]. John Wiley & Sons, 2009.

Jiang Y, Tanabashi Y, Nakagawa M. Modelling Of Rock Joints And Application To Underground Openings In Discontinuous Rock Masses[C]. ISRM International Symposium. International Society for Rock Mechanics, 2000.

Jiang Y, Xiao J, Yamaguchi K, et al. Mechanical Behaviour and Support Design of Large Underground Opening in Discontinuous Rock Masses[J]. Journal Mining and Materials Processing Institute of Japan, 2001, 117(8): 639-644.

Jiang Y, Xiao J, Tanabashi Y, et al. Development of an automated servo-controlled direct shear apparatus applying a constant normal stiffness condition[J]. International Journal of Rock Mechanics and Mining Sciences, 2004, 41(2): 275-286.

Jiang Y, Tanabashi Y, Li B, et al. Influence of geometrical distribution of rock joints on deformational behavior of underground opening[J]. Tunnelling and underground space technology, 2006, 21(5): 485-491.

Jiang Y, Li B, Yamashita Y. Simulation of cracking near a large underground cavern in a discontinuous rock mass using the expanded distinct element method[J]. International Journal of Rock Mechanics and Mining Sciences, 2009, 46(1): 97-106.

Jiang Y, Gao Y, Li B, Ogawa Y, Yang L. Research on health assessment technique of tunnel lining based on power spectrum density characteristics of microtremors[J]. Journal of Japan Society of Civil Engineers, 2012, 68(3): I_111-118.

Jiles D C. Review of magnetic methods for nondestructive evaluation[J]. NDT international, 1988, 21(5): 311-319.

Jones B, Carnevale M, Hager J. Comparison of high-resolution 3D imaging radar survey with material testing data in an overall structural integrity assessment of a concrete ringwall[C]. Proceedings of 11th international conference on ground penetrating radar, Columbus, Ohio. 2006.

Júlio E N B S, da Silva Rebelo C A, Dias-da-Costa D A S G. Structural assessment of the tower of the University of Coimbra by modal identification[J]. Engineering Structures, 2008, 30(12): 3468-3477.

Kim J T, Ryu Y S, Cho H M, et al. Damage identification in beam-type structures: frequency-based method vs mode-shape-based method[J]. Engineering structures, 2003, 25(1): 57-67.

Kirchhoff G. Über das Gleichgewicht und die Bewegung einer elastischen Scheibe[J]. Journal für die reine und angewandte Mathematik, 1850, 40: 51-88.

Kulatilake P, Ucpirti H, Wang S, et al. Use of the distinct element method to perform stress analysis in rock with non-persistent joints and to study the effect of joint geometry parameters on the strength and deformability of rock masses[J]. Rock mechanics and rock engineering, 1992, 25(4): 253-274.

Kundu T, Boström A. Elastic wave scattering by a circular crack in a transversely isotropic solid[J]. Wave Motion, 1992, 15(3): 285-300.

Kuo C M, Hall K T, Darter M I. Three-dimensional finite element model for analysis of concrete pavement support[J]. Transportation Research Record, 1995 (1505): 119-127.

Konno K, Ohmachi T. Ground-motion characteristics estimated from spectral ratio between horizontal and vertical components of microtremor[J]. Bulletin of the Seismological Society of America, 1998, 88(1): 228-241.

Kitagawa G. Changing spectrum estimation[J]. Journal of Sound and Vibration, 1983, 89(3): 433-445.

Kuhlemeyer R L, Lysmer J. Finite element method accuracy for wave propagation problems[J]. Journal of Soil Mechanics & Foundations Div, 1973, 99(Tech Rpt).

Lam H F, Lee Y Y, Sun H Y, et al. Application of the spatial wavelet transform and Bayesian approach to the crack detection of a partially obstructed beam[J]. Thin-walled structures, 2005, 43(1): 1-21.

Lam H F, Lee Y Y, Sun H Y, et al. Application of the spatial wavelet transform and Bayesian approach to the crack detection of a partially obstructed beam[J]. Thin-walled structures, 2005, 43(1): 1-21.

Lam H F, Ng C T. The selection of pattern features for structural damage detection using an extended Bayesian ANN algorithm[J]. Engineering Structures, 2008, 30(10): 2762-2770.

Lauterbach B, Gross D. Crack growth in brittle solids under compression[J]. Mechanics of Materials, 1998, 29(2): 81-92.

Lee, J.S.. Installation of real-time monitoring system for high-speed railroad tunnel[J]. Korean Tunnel Association , 2001,3: 63-67.

Lee V W, Trifunac M D. Response of tunnels to incident SH-waves[J]. Journal of the Engineering Mechanics Division, 1979, 105(4): 643-659.

Leissa A W. Vibration of shells[M]. Washington, DC, USA: Scientific and Technical Information Office, National Aeronautics and Space Administration, 1973.

Lermo J, Chávez-García F J. Are microtremors useful in site response evaluation?[J]. Bulletin of the Seismological Society of America, 1994, 84(5): 1350-1364.

Li X. Study on free vibration analysis of circular cylindrical shells using wave propagation[J]. Journal of sound and vibration, 2008, 311(3): 667-682.

Li B, Jiang Y, Tanabashi Y, et al. Behavior of large scale underground cavern located in jointed rock masses evaluated by using Distinct Element Method[J]. Soils and Foundations, 2010, 50(5): 609-621.

Lombaert G, Degrande G, Clouteau D. Numerical modelling of free field traffic-induced vibrations[J]. Soil Dynamics and Earthquake Engineering, 2000, 19(7): 473-488.

Loutridis S, Douka E, Hadjileontiadis L J, et al. A two-dimensional wavelet transform for detection of cracks in plates[J]. Engineering structures, 2005, 27(9): 1327-1338.

Love A E H. The small free vibrations and deformation of a thin elastic shell[J]. Philosophical Transactions of the Royal Society of London. A, 1888: 491-546.

Magalhaes F, Cunha A, Caetano E. Online automatic identification of the modal parameters of a long span arch bridge[J]. Mechanical Systems and Signal Processing, 2009, 23(2): 316-329.

Makino K, Study on Identification Method of Structural Vibration Characteristics of Existing Bridges by Vibration Measurement using Laser Doppler Velocimeter. Doctoral thesis, Nagasaki University, Fukuoka, Japan, 2013.

Mal A K, Bar-Cohen Y, Yin C C. Analysis of acoustic pulses reflected from fiber-reinforced composite laminates[J]. Journal of applied mechanics, 1992, 59(2S): S136-S144.

Malmgren L, Nordlund E, Rolund S. Adhesion strength and shrinkage of shotcrete[J]. Tunnelling and underground space technology, 2005, 20(1): 33-48.

Malmgren L, Nordlund E. Behaviour of shotcrete supported rock wedges subjected to blast-induced vibrations[J]. International Journal of Rock Mechanics and Mining Sciences, 2006, 43(4): 593-615.

Massenzio M, Jacquelin E, Ovigne P A. Natural frequency evaluation of a cracked RC beam with or without composite strengthening for a damage assessment[J]. Materials and structures, 2005, 38(10): 865-873.

MATLAB Reference Guide, The Math Works, Inc., Natic, MA 2003.

McCandless S. An algorithm for automatic formant extraction using linear prediction spectra[J]. Acoustics, Speech and Signal Processing, IEEE Transactions on, 1974, 22(2): 135-141.

Meguid M A, Dang H K. The effect of erosion voids on existing tunnel linings[J]. Tunnelling and Underground Space Technology, 2009, 24(3): 278-286.

Metrikine A V, Vrouwenvelder A. Surface ground vibration due to a moving train in a tunnel: two-dimensional model[J]. Journal of Sound and vibration, 2000, 234(1): 43-66.

Michel C, Guéguen P, Bard P Y. Dynamic parameters of structures extracted from ambient vibration measurements: An aid for the seismic vulnerability assessment of existing buildings in moderate seismic hazard regions[J]. Soil Dynamics and Earthquake Engineering, 2008, 28(8): 593-604.

Migliori, A., Bell, T. M., Dixon, R. D., and Strong, R. Resonant Ultrasound Non-Destructive Inspection[R]. Los Alamos National Laboratory report LA-UR-93-225,1993.

Ministry of Land, Infrastructure, Transport and Tourism: White Paper of Land, Infrastructure, Transport and Tourism [R]. Tokyo: National Printing Bureau, 2005.

Modena C, Sonda D, Zonta D. Damage localization in reinforced concrete structures by using damping measurements[J]. Key engineering materials, 1999, 167: 132-141.

Nakagawa K. Numerical approaches of rock mass behaviors considering crack generation and large deformation. Doctoral thesis, Kyushu University, Fukuoka, Japan, 1999.

Nakamura Y. A method for dynamic characteristics estimation of subsurface using microtremor on the ground surface[J]. Railway Technical Research Institute, Quarterly Reports, 1989, 30(1).

Niedzwiecki M. Identification of time-varying processes[M]. New York: Wiley, 2000.

Okada H. The microtremor survey method[M]. Society of Exploration Geophysicists with the cooperation of Society of Exploration Geophysicists of Japan [and] Australian Society of Exploration Geophysicists, 2003.

Pan G, Okada H, Atluri S N. Nonlinear transient dynamic analysis of soil-pavement interaction under moving load: a coupled BEM-FEM approach[J]. Engineering analysis with boundary elements, 1994, 14(1): 99-112.

Pan G, Atluri S N. Dynamic response of finite sized elastic runways subjected to moving loads: a coupled BEM/FEM approach[J]. International journal for numerical methods in engineering, 1995, 38(18): 3143-3166.

Park S, Choi S. Development of methodology for estimating the effective properties of containment buildings[R]. Korea Institute of Nuclear Safety, KINS/HR-836, 2008.

Peeters B. System Identification and Damage Detection in Civil Engineering. PhD thesis, Katholieke Universiteit Leuven, 2000.

Peeters B, Maeck J, De Roeck G. Vibration-based damage detection in civil engineering: excitation sources and temperature effects[J]. Smart materials and Structures, 2001, 10(3): 518.

Peeters B, Van der Auweraer H. POLYMAX: a revolution in operational modal analysis[C]. Proceedings of the 1st International Operational Modal Analysis Conference, Copenhagen, Denmark. 2005.

Pessiki S P, Carino N J. Setting time and strength of concrete using the impact-echo method[J]. NDT and E International, 1997, 30(4): 264-265.

Pierro E, Mucchi E, Soria L, et al. On the vibro-acoustical operational modal analysis of a helicopter cabin[J]. Mechanical Systems and Signal Processing, 2009, 23(4): 1205-1217.

Poranski C F, Greenawald E C, Ham Y S. X-ray backscatter tomography: NDT potential and limitations[C]. Materials Science Forum. 1996, 210: 211-218.

Pratt D, Sansalone M. Impact-echo signal interpretation using artificial intelligence[J]. ACI Materials Journal, 1992, 89(2).

Providakis C P, Sotiropoulos D A, Beskos D E. BEM analysis of reduced dynamic stress concentration by multiple holes[J]. Communications in numerical methods in engineering, 1993, 9(11): 917-924.

Rasmussen K M, Nielsen S R K, Kirkegaard P H. Boundary element method solution in the time domain for a moving time-dependent force[J]. Computers & Structures, 2001, 79(7): 691-701.

Richards J A. Inspection, maintenance and repair of tunnels: international lessons and practice[J]. Tunnelling and Underground Space Technology, 1998, 13(4): 369-375.

Roytman, A B, Titova, O A. Simulation of cylinder shell oscillations with axial crack[C]. Proceeding of the Internal Conference “Mechanika-2001”, 2001, 178-183.

Saenger E H, Gold N, Shapiro S A. Modeling the propagation of elastic waves using a modified finite-difference grid[J]. Wave motion, 2000, 31(1): 77-92.

Saiang D, Malmgren L, Nordlund E. Laboratory tests on shotcrete-rock joints in direct shear, tension and compression[J]. Rock mechanics and rock engineering, 2005, 38(4): 275-297.

Sancar S, Pao Y H. Spectral analysis of elastic pulses backscattered from two cylindrical cavities in a solid. Part I[J]. The Journal of the Acoustical Society of America, 1981, 69(6): 1591-1596.

Salawu O S. Detection of structural damage through changes in frequency: a review[J]. Engineering structures, 1997, 19(9): 718-723.

Sandrone F, Labiouse V. Identification and analysis of Swiss National Road tunnels pathologies[J]. Tunnelling and Underground Space Technology, 2011, 26(2): 374-390.

Sansalone M, Carino N J. Impact-Echo: A method for flaw detection in concrete using transient stress wave[J]. 1986.

Sansalone M, Carino N J. mpact-Echo Method: Detecting Honeycombing, the Depth of Surface-Opening Cracks, and Ungrouted Ducts[J]. Concrete International , 1988a, 10(4): 38-46.

Sansalone M, Carino N J. Laboratory and Field Study of the Impact-Echo Method for Flaw Detection in Concrete[J]. Nondestructive Testing of Concrete, Ed. H.S. Lew, ACI SP-112, American Concrete Institute, 1988b:1-20.

Sasama H, Ukai M, Ohta M, et al. Inspection system for railway facilities using a continuously scanned image[J]. Electrical Engineering in Japan, 1998, 125(2): 52-64.

Shen B, Barton N. The disturbed zone around tunnels in jointed rock masses[J]. International Journal of Rock Mechanics and Mining Sciences, 1997, 34(1): 117-125.

Shi S, Feng H, Zhenqing W, et al. The interaction of plane SH-waves and non-circular cavity surfaced with lining in anisotropic media[J]. Applied Mathematics and Mechanics, 1996, 17(9): 855-867.

SHRP2. Data Presentation[Online]. Available: http://www.ndtoolbox.org/content/tunnel/irt-data-presentation, 2000.

Singh R, Carter B J, Wawrzynek P A, et al. Universal crack closure integral for SIF estimation[J]. Engineering Fracture Mechanics, 1998, 60(2): 133-146.

Sinha S K, Fieguth P W. Automated detection of cracks in buried concrete pipe images[J]. Automation in Construction, 2006, 15(1): 58-72.

Smith B L, Vronay D F. Free vibration of circular cylindrical shells of finite length[J]. AIAA Journal, 1970, 8(3): 601-603.

Snell R C, Milinazzo F. Formant location from LPC analysis data[J]. IEEE Transactions on Speech and Audio Processing, 1993, 1(2): 129-134.

Soedel W. Vibrations of shells and plates[M]. CRC Press, 1981.

Song K I, Cho G C. Numerical study on the evaluation of tunnel shotcrete using the impact-echo method coupled with Fourier transform and short-time Fourier transform[J]. International Journal of Rock Mechanics and Mining Sciences, 2010, 47(8): 1274-1288.

Souley M, Homand F. Stability of jointed rock masses evaluated by UDEC with an extended Saeb-Amadei constitutive law[C]. International journal of rock mechanics and mining sciences & geomechanics abstracts. Pergamon, 1996, 33(3): 233-244.

Stacey T R. Shotcrete in mines–state-of-the-art in South Africa[C]. Proceeding of the Internal Seminar and Field Trials on Mine Surface Support Liners, Section. 2001, 6: 22-24.

Stamos A A, Theodorakopoulos D D, Beskos D E. Harmonic wave response of tunnels in poroelastic saturated soil[J]. Publication of: Computational Mechanics Publications, 1997.

Stent S, Gherardi R, Stenger B, Soga K, Cipolla R. An Image-Based System for Change Detection on Tunnel Linings. 13th IAPR International Conference on Machine Vision Applications, Kyoto, Japan, May 20-23, 2013

Stille H. Rock support in theory and practice[J]. Underground Mining Methods: Engineering Fundamentals and International Case Studies, 2001: 535-546.

Suorineni F T, Tannant D D, Kaiser P K. Determination of fault-related sloughage in open stopes[J]. International Journal of Rock Mechanics and Mining Sciences, 1999, 36(7): 891-906.

Sylvette B C, Cécile C, Pierre-Yves B, et al. H/V ratio: a tool for site effects evaluation. Results from 1-D noise simulations[J]. Geophysical Journal International, 2006, 167(2): 827-837.

Todorovska M, Trifunac M D, Hao T Y. Variations of apparent building frequencies-lessons from full-scale earthquake observations[C]. Proceedings First European Conf. on Earthquake Engineering and Seismology. 2006: 3-8..

Tokimatsu, K. Geotechnical site characterization using surface wave. Proceeding of the 1st Internal Conference on Earthquake Geotechnique Engineering, 1995: 1333-1367.

Tung P C, Hwang Y R, Wu M C. The development of a mobile manipulator imaging system for bridge crack inspection[J]. Automation in construction, 2002, 11(6): 717-729.

Tunnel Operations, Maintenance, Inspection and Evaluation (TOMIE) Manual [M]. DTFH61-07-D-00004 – TASK ORDER 006 / TECHNICAL DIRECTIVE 003, 2013.

Uddin W, Ricalde L. Nonlinear material modeling and dynamic finite element simulation of asphalt pavement[C]. Proceedings Fourteenth Engineering Mechanics Conference, ASCE, Austin, Tex, 2000.

Ulriksen C P F. Application of Impulse Radar to Civil Engineering: Doctoral Thesis[M]. University of Technology, Department of Engineering Geology, 1982.

Ukai M. Advanced Inspection System of Tunnel Wall Deformation using Image Processing[J]. Railway Technical Research Institute, Quarterly Reports, 2007, 48(2).

U.S. Department of Transportation. Detecting Underground Storage Tanks [Online]. Available: http://www.cflhd.gov/resources/agm/engApplications/SubsurfaceChart --acter/632DetectingUnderground StorageTanks .cfm, 2014.

Varadan V V. Scattering matrix for elastic waves. II. Application to elliptic cylinders[J]. The Journal of the Acoustical Society of America, 1978, 63(4): 1014-1024.

Ventura C E, Liam Finn W D, Lord J F, et al. Dynamic characteristics of a base isolated building from ambient vibration measurements and low level earthquake shaking[J]. Soil Dynamics and Earthquake Engineering, 2003, 23(4): 313-322.

Vestroni F, Capecchi D. Damage detection in beam structures based on frequency measurements[J]. Journal of Engineering Mechanics, 2000, 126(7): 761-768.

Wang C, Lai J C S. Prediction of natural frequencies of finite length circular cylindrical shells[J]. Applied acoustics, 2000, 59(4): 385-400.

Warburton G B, Higgs J. Natural frequencies of thin cantilever cylindrical shells[J]. Journal of Sound and Vibration, 1970, 11(3): 335-338.

Welch P D. The use of fast Fourier transform for the estimation of power spectra: a method based on time averaging over short, modified periodograms[J]. IEEE Transactions on audio and electroacoustics, 1967, 15(2): 70-73.

Wiehle C.K. Review of Soil-Structure Interaction. Proceedings of the Symposium on Soil-Structure Interaction. Tucson Ariz. University of Arizona, 239-245, 1964.

Williams C, Salawu O S. Damping as a damage indication parameter[C]. Proceedings-spie the international society for optical engineering. Spie international society for optical, 1997: 1531-1536.

Wills, R. H. A digital phase coded ground probing radar: Ground penetrating radar, in J. Pilon, ed., Geological Survey of Canada, 231–235, 1992.

Wong R H C, Tang C A, Chau K T, et al. Splitting failure in brittle rocks containing pre-existing flaws under uniaxial compression[J]. Engineering Fracture Mechanics, 2002, 69(17): 1853-1871.

Xu M B, Zhang X M. Vibration power flow in a fluid-filled cylindrical shell[J]. Journal of sound and vibration, 1998, 218(4): 587-598.

Xu M B, Zhang X M, Zhang W H. Space-harmonic analysis of input power flow in a periodically stiffened shell filled with fluid[J]. Journal of Sound and Vibration, 1999, 222(4): 531-546.

Xu M B, Zhang X M, Zhang W H. The effect of wall joint on the vibrational power flow propagation in a fluid-filled shell[J]. Journal of sound and vibration, 1999, 224(3): 395-410.

Xu M B, Zhang W H. Vibrational power flow input and transmission in a circular cylindrical shell filled with fluid[J]. Journal of Sound and Vibration, 2000, 234(3): 387-403.

Yam L H, Li Y Y, Wong W O. Sensitivity studies of parameters for damage detection of plate-like structures using static and dynamic approaches[J]. Engineering structures, 2002, 24(11): 1465-1475.

Yoon J S, Sagong M, Lee J S, et al. Feature extraction of a concrete tunnel liner from 3D laser scanning data[J]. NDT & E International, 2009, 42(2): 97-105.

Yu C P, Cheng C C, Lai J. Application of closed-form solution for normal surface displacements on impacted half space: quantification of impact-echo signals[J]. 2006;4(2):127–50.

Yu S N, Jang J H, Han C S. Auto inspection system using a mobile robot for detecting concrete cracks in a tunnel[J]. Automation in Construction, 2007, 16(3): 255-261.

Yuen K V, Lam H F. On the complexity of artificial neural networks for smart structures monitoring[J]. Engineering Structures, 2006, 28(7): 977-984.

Zaghloul S M, White T. Use of a three-dimensional, dynamic finite element program for analysis of flexible pavement. Transportation Research Record. 1388, TRB, National Research Council, Washington, D.C., 60–69, 1993.

Zerwer A, Cascante G, Hutchinson J. Parameter estimation in finite element simulations of Rayleigh waves[J]. Journal of geotechnical and geoenvironmental engineering, 2002, 128(3): 250-261.

Chuhan Z, Pekau O A, Feng J, et al. Application of distinct element method in dynamic analysis of high rock slopes and blocky structures[J]. Soil Dynamics and Earthquake Engineering, 1997, 16(6): 385-394.

Zhang X M, Liu G R, Lam K Y. Vibration analysis of thin cylindrical shells using wave propagation approach[J]. Journal of Sound and Vibration, 2001, 239(3): 397-403.

Zhang X M, Liu G R, Lam K Y. Coupled vibration analysis of fluid-filled cylindrical shells using the wave propagation approach[J]. Applied Acoustics, 2001, 62(3): 229-243.

Zhang X M. Frequency analysis of submerged cylindrical shells with the wave propagation approach[J]. International Journal of Mechanical Sciences, 2002, 44(7): 1259-1273.

Zhang X M. Vibration analysis of cross-ply laminated composite cylindrical shells using the wave propagation approach[J]. Applied Acoustics, 2001, 62(11): 1221-1228.

Zhan Y M, Jardine A K S. Adaptive autoregressive modeling of non-stationary vibration signals under distinct gear states. Part 1: modeling[J]. Journal of Sound and Vibration, 2005, 286(3): 429-450.

Zhao X B, Zhao J, Hefny A M, et al. Normal transmission of S-wave across parallel fractures with Coulomb slip behavior[J]. Journal of engineering mechanics, 2006, 132(6): 641-650.

Zhao X B, Zhao J, Cai J G, et al. UDEC modelling on wave propagation across fractured rock masses[J]. Computers and Geotechnics, 2008, 35(1): 97-104.